

UNCLASSIFIED

AD 407 169

DEFENSE DOCUMENTATION CENTER

FOR

SCIENTIFIC AND TECHNICAL INFORMATION

CAMERON STATION, ALEXANDRIA, VIRGINIA



UNCLASSIFIED

NOTICE: When government or other drawings, specifications or other data are used for any purpose other than in connection with a definitely related government procurement operation, the U. S. Government thereby incurs no responsibility, nor any obligation whatsoever; and the fact that the Government may have formulated, furnished, or in any way supplied the said drawings, specifications, or other data is not to be regarded by implication or otherwise as in any manner licensing the holder or any other person or corporation, or conveying any rights or permission to manufacture, use or sell any patented invention that may in any way be related thereto.

407 169

CURTISS



WRIGHT

CURTISS-WRIGHT CORPORATION
RESEARCH DIVISION
QUEHANNA, PA. U.S.A.

PAGES _____
ARE
MISSING
IN
ORIGINAL
DOCUMENT

14 March 1960

Director
Advanced Research Projects Agency
The Pentagon
Washington 25, D.C.

SUBJECT: Status Report dated 1 March 1960 on "Compact Charge Exchange"
Contract NOar 2886(00), Task Number 094-347.

REFERENCE: Department of the Navy Letter ONR: 429: WLM: 111, NR 094-347
of February 23, 1960.

Dear Sir:

In accordance with reference letter, subject report is attached in quadruplicate. Inasmuch as the reporting instructions have been somewhat modified, subject report has been prepared to as an up-to-date technical status report. All prior reports were in letter form. The next report will be the Final Report, and will be submitted not later than 30 days following 1 May 1960 which is the contract termination date.

E. M. Petrick
Project Director

EMP/amr

ENC: Report CWR 300-116 (4)

Distribution:

Chief of Naval Research (Code 429) (2 copies)
Department of the Navy
Washington 25, D.C.

Chief, Bureau of Naval Weapons (Code RAFF-3) (2 copies)
Department of the Navy
Washington 25, D.C.

Commanding Officer (1 copy)
Office of Naval Research Branch Office
346 Broadway
New York 13, N. Y.

ARPA Cont. No. 159

④ NA

⑤ 236 500

⑦

⑨ Quarterly Status Report

⑭ CWR 300-116

⑥ EXPERIMENTAL INVESTIGATION
of
COMPACT CHARGE IONIZATION

⑪ March 1, 1960

⑫ ARPA Order Number 5158-694-349
⑬ Contract Number NOnr 2886(00)

② NA

③ NA

④ 1584

⑤ NA

⑥ NA

⑦ NA

⑧ NA

⑨ NA

⑩ NA

J.C.

Published March 21, 1960

CURTISS



WRIGHT

JUN 21 1960

RECEIVED
TISIA A

CURTISS-WRIGHT CORPORATION

RESEARCH DIVISION

QUEHANNA, PENNSYLVANIA

ARPA CONF. NO. 1599

Copy 7

QUARTERLY STATUS REPORT

ARPA Order Number 5-58
Project Code Number Unassigned
Contract Number NOnr 2886(00)
Contract Period 1 May 1959 to 30 April 1960
Project Director Dr. E. N. Petrick, Phone
Frenchville AMherst 3-4711

Prepared by

E. N. Petrick, O. K. Husmann, and
H. W. Szymanowski,

The authors are indebted to Dr. C. Burnett, Pennsylvania State University,
and to Messrs. R. Hughes and W. Aker of the Curtiss-Wright Research Division
for their assistance in the preparation of this report.

Approved for release by

J. E. Sanders
J. E. Sanders, Chief, Powerplant Sciences and Engineering

CURTISS-WRIGHT CORPORATION • RESEARCH DIVISION



Contents

1	I. INTRODUCTION
3	II. THEORETICAL CONSIDERATIONS
3	A. The Charge Exchange Method
30	B. The RF Ion Source
32	C. The Plasma Arc Source
39	III. TYPES OF CONTACT EMITTERS
39	A. Porous Sintered Tungsten
39	B. Mechanically Perforated Platinum Screen
42	C. Electro-Formed Molybdenum Screen
45	IV. DIFFUSION EXPERIMENTS
77	V. EXPERIMENTAL EVALUATION OF VARIOUS CONTACT EMITTERS
77	A. Ion Gun
90	B. Mass Spectrometer
101	VI. EMITTER HEATING TECHNIQUES
101	A. Resistance Heating
104	B. Radiation Heating
104	C. RF Heating
104	D. Arc Heating
109	VII. BONDING THE EMITTER
109	A. Mechanical Joints
112	B. Brazing
118	C. Welding
121	D. Sintering in Place
123	VIII. CORROSION OF MATERIALS BY CESIUM
123	A. Introduction
123	B. Materials
124	C. Test Procedure
128	D. Results
138	E. Next Test Phase
139	IX. CESIUM GENERATION IN SITU



Contents

143	X. THE RF ION SOURCE APPARATUS
147	XI. THE PLASMA ARC SOURCE, PROPOSED EXPERIMENTS
147	A. Diagnostics
150	B. Ion Extraction
155	XII. CONCLUSION AND RECOMMENDATIONS
157	REFERENCES



Tables

3	II-A	IONIZATION POTENTIAL OF ALKALI METALS
4	II-B	WORK FUNCTION AND MELTING POINT OF EMITTER MATERIALS
49	IV-A	PORE SIZE COUNT
50	IV-B	MEAN PORE DIAMETER
59	IV-C	SOME GAS PROPERTIES
59	IV-D	PLATINUM SCREEN DIFFUSION RESULTS
62	IV-E	CLAUSING FACTOR
62	IV-F	MOLYBDENUM SCREEN FLOW TESTS
65	IV-G	FLOW TEST OF P-2 TUNGSTEN PLATE
70	IV-H	FLOW DATA FOR F-1 POROUS PLATE
71	IV-I	FLOW DATA FOR C-1 POROUS TUNGSTEN PLATE
129	VIII-A	EFFECT OF A CESIUM ATMOSPHERE ON VARIOUS METALS
130	VIII-B	EFFECT OF CESIUM ATMOSPHERE ON VARIOUS NON-METALLIC MATERIALS
131	VIII-C	SECOND CESIUM CORROSION TEST WITH METALS



Figures

- | | |
|----|--|
| 5 | II-1. Efficiency Versus Temperature for Various Ion Propulsion Fuels |
| 6 | II-2. Ionization Efficiency of Cesium |
| 7 | II-3. Ionization Efficiency of Rubidium |
| 8 | II-4. Ionization Efficiency of Potassium |
| 9 | II-5. Ionization Efficiency of Sodium |
| 10 | II-6. Ionization Efficiency of Lithium |
| 13 | II-7. Lifetime on Heated Tungsten Surface |
| 14 | II-8. Lifetime of Rb Atom on Tungsten for Various Degrees of Contamination |
| 16 | II-9. Saturation Vapor Pressure of Alkali Metals |
| 18 | II-10. Mean Free Path |
| 20 | II-11. Flow Rate as a Function of Pore Size and Emitter Temperature |
| 21 | II-12. Heat Loss by Radiation to Space as a Function of Emitter Temperature and Emissivity, Neglecting Solar Radiation |
| 23 | II-13. Effect of Electrode Spacing for Plane Electrodes |
| 24 | II-14. Effect of Fuel Mass on Current Density |
| 25 | II-15. Current-Field Characteristics for Tungsten Covered with K and Cs |
| 28 | II-16. Radial Potential Drop in a Cesium Ion Beam |
| 29 | II-17. Longitudinal Potential Drop in a Cesium Ion Beam |
| 31 | II-18. Breakdown in RF Field with Electrodes Oxidized |
| 33 | II-19. Ion Condenser System |
| 34 | II-20. Effect of Ion Condenser |
| 35 | II-21. Effect of Magnetic Field (Transversal) |
| 40 | III-1. Platinum Emitter (Drawing) |
| 41 | III-2. Platinum Emitter (Photograph) |
| 43 | III-3. Photograph of Molybdenum Screen |
| 46 | IV-1. Diffusion Flow Rate Measuring Apparatus |
| 47 | IV-2. Diffusion Flow Measuring Apparatus |
| 51 | IV-3. Cross-Section of F-2 Porous Plate - Surface of Plate at Top (1000X) |
| 52 | IV-4. Cross-Section of F-2 Porous Plate - Parallel to Plate Surface (1000X) |
| 53 | IV-5. Cross-Section of P-1 Porous Plate (1000X) |
| 54 | IV-6. Proportional Frequency of Void Lengths |
| 55 | IV-7. Theoretical Porous Plate Model with Uniform Spherical Grains |
| 56 | IV-8. Mean Pore Radius Versus Grain Diameter for Theoretical Model with Uniform Spherical Grain |
| 57 | IV-9. Theoretical Flow in Amps per cm^2 in Model Plate as a Function of Pore Radius |
| 58 | IV-10. Theoretical Flow in Amps per cm^2 in Model Plate as a Function of Porous Volume |
| 60 | IV-11. Molecular Flow Rate through a Bundle of Capillaries as a Function of Molecular Weight |
| 61 | IV-12. Molecular Flow Rate through a Bundle of Capillaries as a Function of Pore Radius |



Figures

63	IV-13. Experimental and Theoretical Diffusion Flow for Platinum Screen
64	IV-14. Platinum Screen Diffusion Flow as a Function of Screen Temperature
66	IV-15. Flow Rate for Molybdenum Screen
67	IV-16. Experimental and Theoretical Flow Data for P-2 Tungsten Plate
68	IV-17. Flow Data for F-1 Porous Tungsten Plate Showing Aging Effect
69	IV-18. Experimental and Theoretical Flow Data for F-1 Porous Plate
72	IV-19. Helium Flow Rate through Porous Tungsten as a Function of Plate Temperature (Molecular Flow)
73	IV-20. Experimental and Theoretical Flow Data for C-1 Porous Plate
74	IV-21. Transmission Coefficient Versus Porous Volume for Barium through Porous Plate
79	V-1. Ion Gun
81	V-2. Ion Gun Assembly - Photograph
82	V-3. RF Heating of the P-1 Porous Tungsten Emitter
83	V-4. Wiring Diagram for Ion Gun
85	V-5. Pressure Increase in the Ion Gun as a Function of the Accelerating Potential
86	V-6. Experimental Results with P-1 Emitter in First Test
87	V-7. Dependence of Ion Current on Fuel Vapor Pressure (Temperature)
88	V-8. Theoretical Dependence of Ion Current on Plate Temperature
89	V-9. Ion Gun Current with Residual Gases
91	V-10. Potential Distribution Proposed Ion Gun
92	V-11. Construction of Ion Beam Trajectory
93	V-12. Experimental Ion Current with P-1 Emitter Using Focusing Electrode
94	V-13. Experimental Ion Current with P-1 Emitter, After Fire Hours Operation
96	V-14. Sketch of Mass Spectrometer
97	V-15. Mass Spectrometer During Assembly
99	V-16. Field Strength in Mass Spectrometer
102	VI-1. Direct Resistance Heated Ion Source - Assembly
103	VI-2. Direct Resistance Heated Ion Source - Components
105	VI-3. Radiation Heating
106	VI-4. Arc Heating
110	VII-1. "L" Cathode
111	VII-2. Powder Seal
113	VII-3. Nickel Brazed Porous Tungsten Plate
115	VII-4. Typical Brazing Set-Up
116	VII-5. First Platinum Braze Configuration
117	VII-6. Cross-Section of Brazed Assembly
119	VII-7. RF Heating Assembly for Joining Ceramic Tube to Porous Tungsten Plate
120	VII-8. Vacuum Arc Weld Apparatus
122	VII-9. Porous Tungsten Plate Sintered Directly into Tungsten Tube



Figures

- | | | |
|------|---------|--|
| 126 | VIII-1. | Metallic Samples in Glass Vacuum Container |
| 127 | VIII-2. | Test Set-Up for Loading Cesium into Corrosion Containers |
| 132 | VIII-3. | Photomicrograph of Aluminum Sample Exposed to Cesium Vapor at 550°F for 100 hours (500X) |
| 133 | VIII-4. | Molybdenum Before and After Cesium Corrosion Test |
| 134 | VIII-5. | Niobium Before and After Cesium Corrosion Test |
| 135 | VIII-6. | Inconel X Before and After Cesium Corrosion Test |
| 136 | VIII-7. | Stainless Steel 308 Before and After Cesium Corrosion Test |
| 137 | VIII-8. | Iridium Before and After Cesium Corrosion Test |
|
 | | |
| 141 | IX-1. | Vacuum System for Cesium Generator Experiments |
|
 | | |
| 144 | X-1. | RF Hydrogen Ion Source in the Manner of Moak, et al. |
| 145 | X-2. | RF Ion Source |
|
 | | |
| 151 | XI-1. | Magnetically Constricted Plasma-Arc |



I. INTRODUCTION

The objective of the ~~contract~~ work described ~~herein~~ is to experimentally investigate and optimize a compact ion emitter in order to provide maximum beam current per unit area. The principal investigation involves the use of cesium ionized by the charge exchange (contact) method, with additional limited studies (for comparison purposes) of the RF and plasma-arc methods.

During the course of the experimental work, there have been some changes in emphasis as compared to the statement of work presented in the original proposal of Ref. 1. The changes have been necessary in order to solve some additional problems to satisfy the contract objective. These problems include, for example, cesium corrosion studies, bonding techniques, and cesium handling techniques, none of which were originally proposed. It should be noted that the ion emitter must provide (a) an acceptable efficiency and (b) reliability ~~and long life. Based on these requirements, the program has en-~~compassed the following analytical and experimental studies:

~~(a) For Maximum Efficiency:~~

- (1) Analytical studies of fuel flow rates, migration velocity, neutral lifetime, and ionization efficiency;
- (2) Diffusion experiments to establish the flow regime through the emitter;
- (3) Development of a bonding technique (emitter attachment to vapor source) to eliminate by-pass flow, i.e., fuel leakage; ~~Techniques include powder seal, metallized ceramic joint, arc weld, braze, and sintering in place.~~
- (4) Tests of various emitters for ionization efficiency, including sintered tungsten plates (40% to 80% density), molybdenum screen (0.003 in. holes), and platinum screen (0.0005 in. holes). ~~Preliminary ionization tests are conducted with an ion gun; precise tests with a mass spectrometer.~~
- (5) Comparison with other ionization techniques, including studies of a plasma-seeding method, and of an RF method;

~~(b) For Reliability and Long Life:~~

- (6) ~~Corrosion tests to establish the materials least subject to attack by cesium, including emitter materials (tungsten, molybdenum, platinum), structural materials (nickel, stainless steel), electrical conductors (copper), and electrical insulators (aluminum oxide);~~
- (7) ~~Investigation of emitter heating techniques, with tests of an inductive technique (no internal connections) and of a direct heating technique; and~~



- (3) ~~4~~ Elimination of fuel handling problems. Test of cesium generation in situ by reduction of a storable cesium salt, thereby eliminating liquid cesium storage in sealed vacuum ampules.

The status of each of the above phases of the investigation is contained in the present report. The data are not yet complete and should be considered as preliminary. Final data, conclusions, and recommendations will be included in the final report at the completion of the present contract period.



CURTISS-WRIGHT CORPORATION • RESEARCH DIVISION

II. THEORETICAL CONSIDERATIONS

The principal emphasis in this investigation is on the charge exchange (contact) method of producing ions, by passing an alkali metal vapor through a porous or screen emitter. Other techniques considered include the RF source and the plasma arc source. Each of the methods is described in more detail below.

A. The Charge Exchange Method

In this technique an emitter material with high work function ϕ removes an electron from the alkali atom, which has an ionization potential lower than ϕ . The charge exchange method, under certain conditions which will be discussed later, offers the advantage of a high ionization efficiency when compared with other ionizing methods.

Ionization efficiency has been discussed recently by Eucken (Ref. 2), Zemel (Ref. 3), and Datz and Taylor (Ref. 4). Previous papers include those of Killian (Ref. 5), Taylor and Langmuir (Ref. 6), Copley and Phipps (Ref. 7), Keuk and Loeb (Ref. 8), and Taylor and Langmuir (Ref. 9). Development of the alkali-ion source from the Kunsman type to the porous plate has been reported by Nordmeyer (Ref. 10) and, in particular, by Koch (Ref. 11). A high ionization efficiency as a principal criterion for ion sources in space travel is discussed by Stuhlinger (Ref. 12), Willinsky and Orr (Ref. 13), Langmuir (Ref. 14), Boden (Ref. 15), and Forrester and Speiser (Ref. 16).

The charge exchange method of ionization is efficient with alkali metals because of their low ionization potentials, as given in TABLE II-A.

TABLE II-A. IONIZATION POTENTIAL OF ALKALI METALS

Li	5.390 volts
Na	5.138
K	4.339
Rb	4.176
Cs	3.893

The ionization efficiency is given by the Saha equation:

$$n_i / (n_i + n_a) = \left\{ 1 + 2 \exp \left[-(\phi - I) e / kT \right] \right\}^{-1} \quad (\text{Eq. II-1})$$



where

n_i = number of ions
 n_a = number of neutrals
 e = $(1.602) \cdot 10^{-19}$ coul
 ϕ = work function, volts
 I = ionization potential, volts
 k = $(1.38) \cdot 10^{-16}$ erg/grad
 T = deg. Kelvin

Figure II-1 presents the ionization efficiency for all the alkali metals as a function of temperature, with work function as the parameter. The curves indicate that the ionization efficiency depends both on the work function and on the ionization potential, and increases as the difference between the two values increases. A work function improvement of 0.1 volt increases the ionization efficiency considerably, as can be noted. Increasing the temperature reduces the ionization efficiency, and the efficiency remains between 99% and 100% efficiency over a wide temperature range only when the difference between work function and the ionization potential is large. Ionization starts at approximately 1200°K, when the exchange surface starts to clean up by evaporation of contaminating materials on the emitter surface. Even potassium exhibits high ionization efficiency at reasonable work functions at a temperature of 2000°K. The higher ionization efficiencies at high temperatures for sodium and lithium can be maintained only with high work function materials. Figures II-2 through II-6 illustrate that the work function must be high to maintain a given ionization efficiency as the temperature is raised.

The charge-exchange material is evaluated on the basis of two factors: work function and melting point. Materials which suit this requirement for alkali metal ionization are tungsten, molybdenum, tantalum, niobium, rhenium, and platinum, as illustrated in TABLE II-B.

TABLE II-B. WORK FUNCTION AND MELTING POINT OF EMITTER MATERIALS

<u>Material</u>	<u>Electron Work Function</u>	<u>Melting Point</u>
W	4.54 volt	3380° C
Mo	4.24	2622
Ta	4.13	2996
Nb	3.99	2410
Pt	5.36 and 6.37	1773.5
Re	4.97	3172
W Oxide	6.24	3380
Pt Oxide	6.55	1773.5



CURTISS-WRIGHT CORPORATION, RESEARCH DIVISION

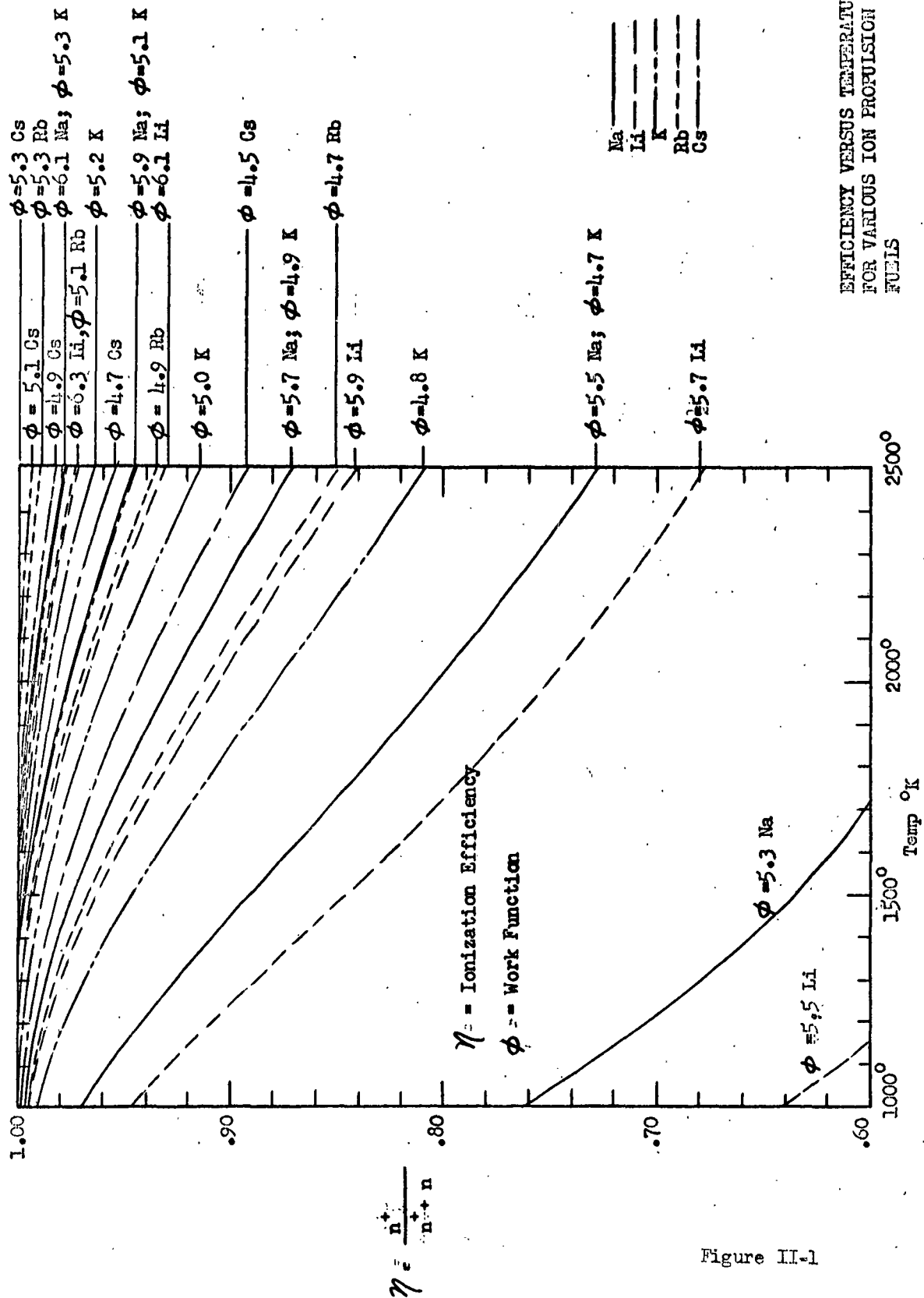
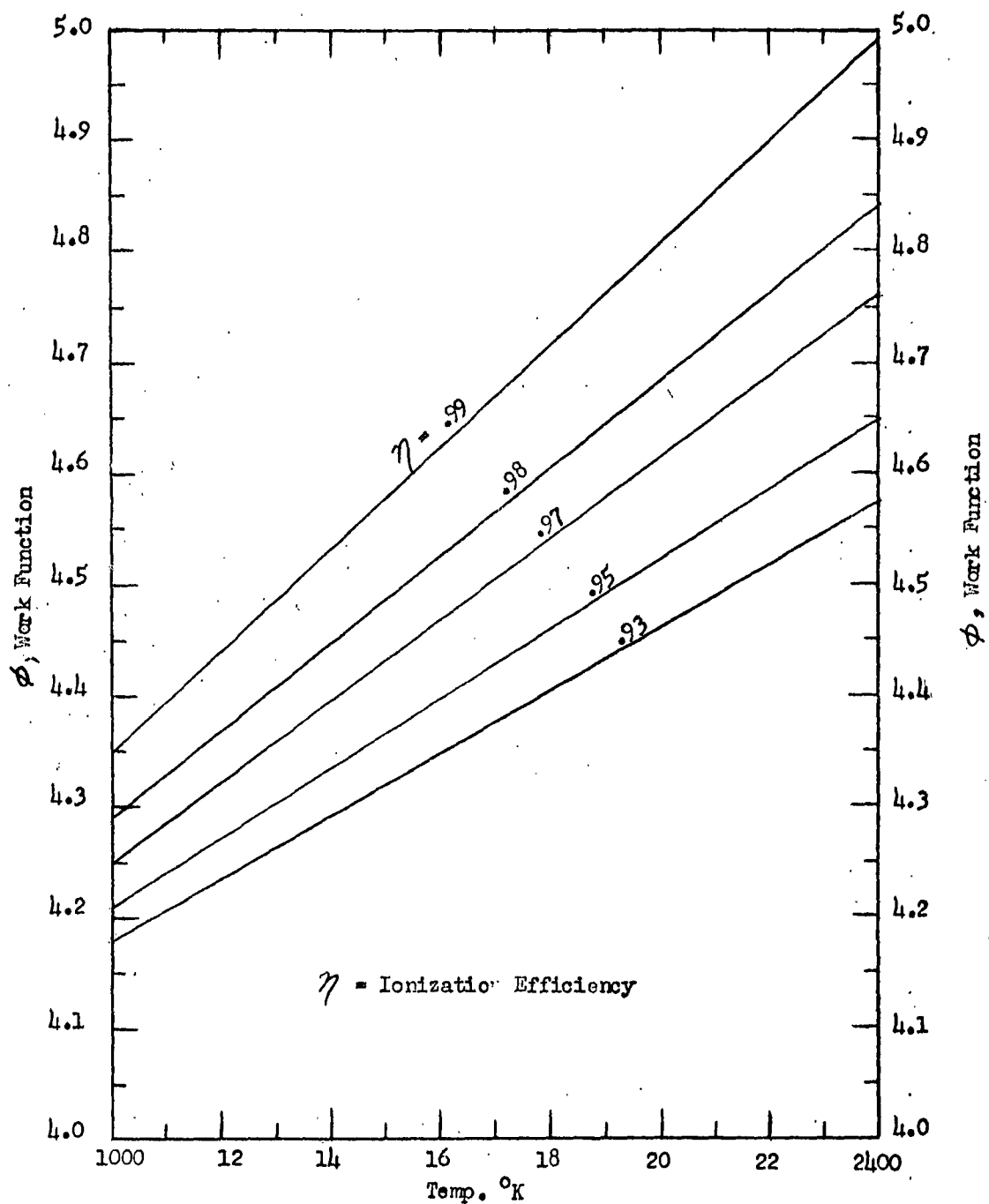
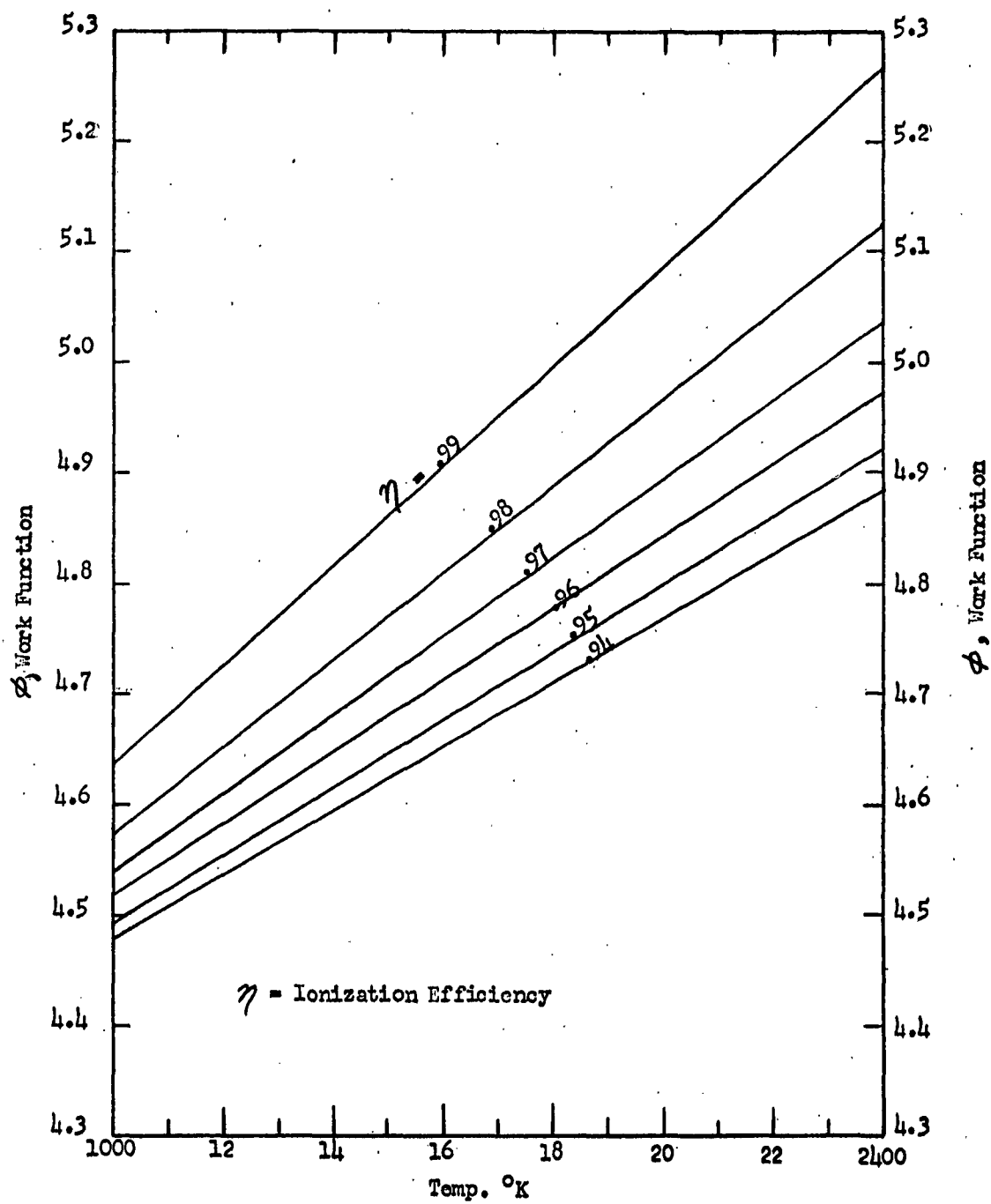


Figure II-1



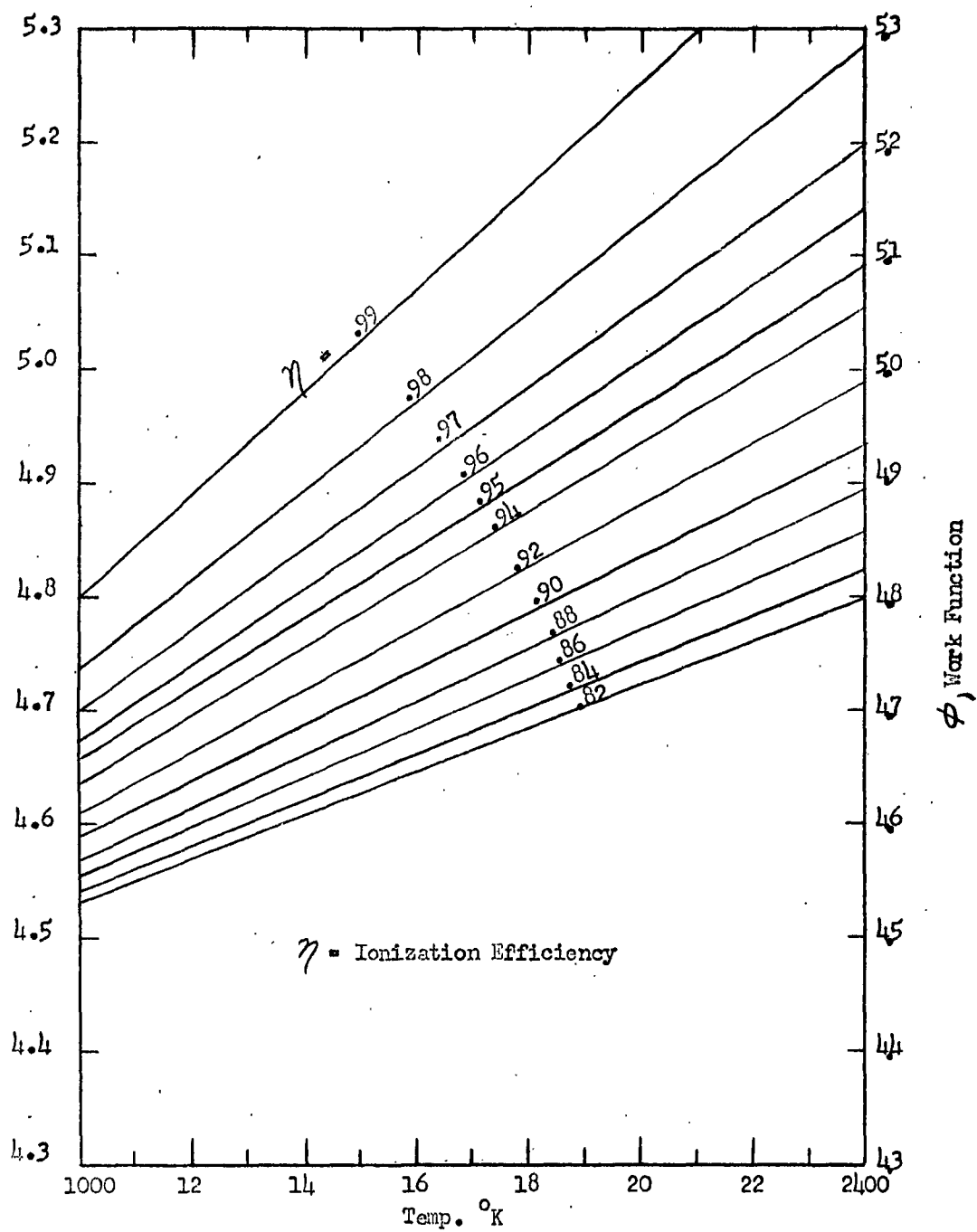
IONIZATION EFFICIENCY OF CESIUM

Figure II-2



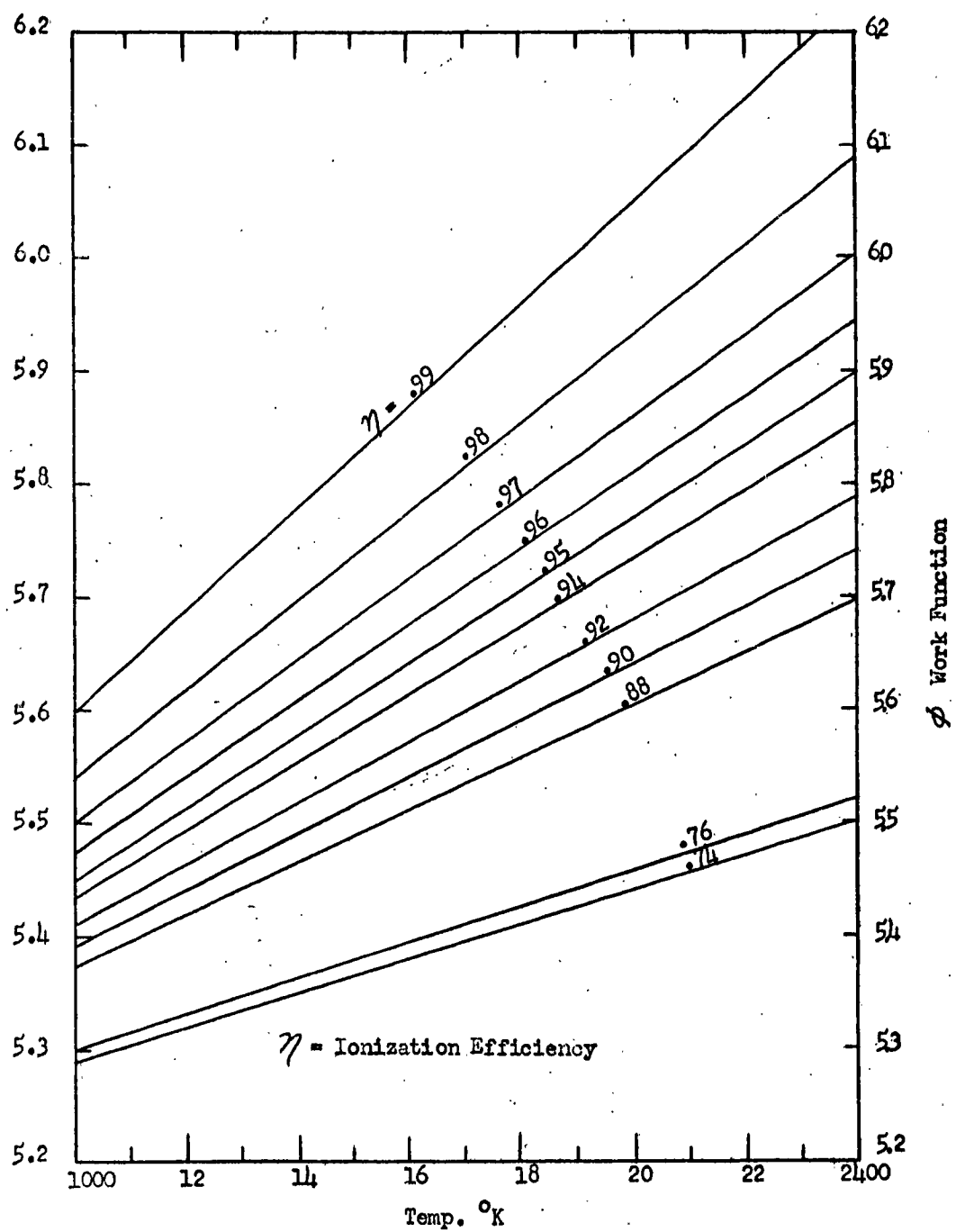
IONIZATION EFFICIENCY OF RUBIDIUM

Figure II-3



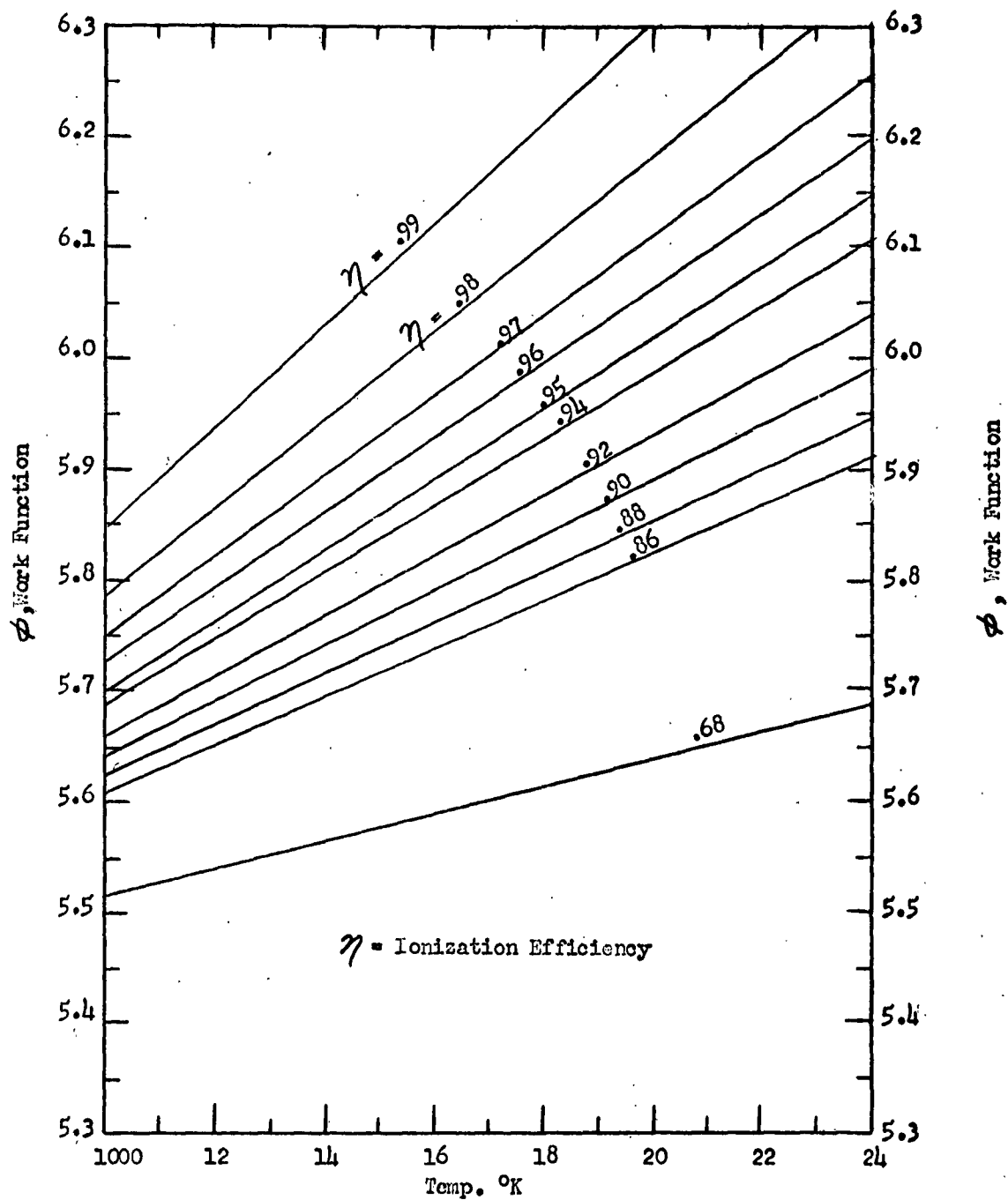
IONIZATION EFFICIENCY OF POTASSIUM

Figure II-4



IONIZATION EFFICIENCY OF SODIUM

Figure II-5



IONIZATION EFFICIENCY OF LITHIUM

Figure II-6

The work functions in TABLE II-B are the electron work functions and do not necessarily dominate in the charge exchange process. For example, two different work functions are reported for platinum. As recent investigations show, the work function is very dependent on the crystallographic index of the emitting surface (Ref. 17). Dependence of the work function on the temperature, as assumed in earlier investigations, may be explained on the basis of this index (Ref. 3). Two commonly used independent methods of measuring the work function are the Richardson equation, predominantly, and also the photo-effect. If there are patches of lower work function on the surface, these will strongly influence the electron emission. Thus, the work function given in TABLE II-B may be considered as a lower limit (Ref. 17). In the case of an oxide layer, the work function is increased considerably, as has been measured for W-oxide and Pt-oxide. Unfortunately, the oxide layers have a short lifetime at elevated temperatures; therefore, they are not of interest unless a sufficient amount of oxide can be supplied continuously (Ref. 18). Desorption of oxygen from tungsten takes place in three stages. Bursts of gas are desorbed at about 500°K, 1150°K, and 1750°K. The work function is of the order of 6 volts or more until the second desorption stage is completed, at which time the work function drops to approximately 5.5 volts. A similar desorption occurs for a Pt-oxide layer.

In regard to the crystallographic index, Hughes, et al., investigated W single crystals (Ref. 17). Their results are in good agreement with the data discovered earlier by E. Mueller (Ref. 18). The lowest work function is exhibited by the W-116 plane; for the 011 plane Mueller found values of 5.70 to 5.99 volts. The Hughes group concluded that the thermionic emission is identical for the three crystallographic directions 112, 112, and 110 with a work function of 5.25 ± 0.05 volt. By etching methods they achieved the surfaces on a single crystal wire. If the emitter is not a single crystal, it is impossible to get the same crystallographic plane over the total surface. Because the ionization efficiency on such higher work function patches is considerably higher than on the other areas, they contribute more to the ionization and, therefore, the overall work function must be weighed. The present experimental investigation is limited to tungsten, molybdenum, and platinum, but in the next phase of the investigation porous Re-plates, sintered or welded in Re-tubes, should be tried. The work function and melting point of rhenium are promising and this material seems to be more workable than tungsten or molybdenum. To obtain an ion source as compact as possible, it is necessary to achieve high current densities. Under optimal conditions, which are described later, the total amount of fuel (alkali metal) evaporated per unit time is dependent on the emitter surface temperature and follows an exponential law.

$$1/t = (\text{const}) \exp (-\phi/kT)$$

(Eq. II-2)



where

ϕ = work function
 $k = (1.38) 10^{-16}$ erg deg $^{-1}$
 T = deg. Kelvin
 t = time

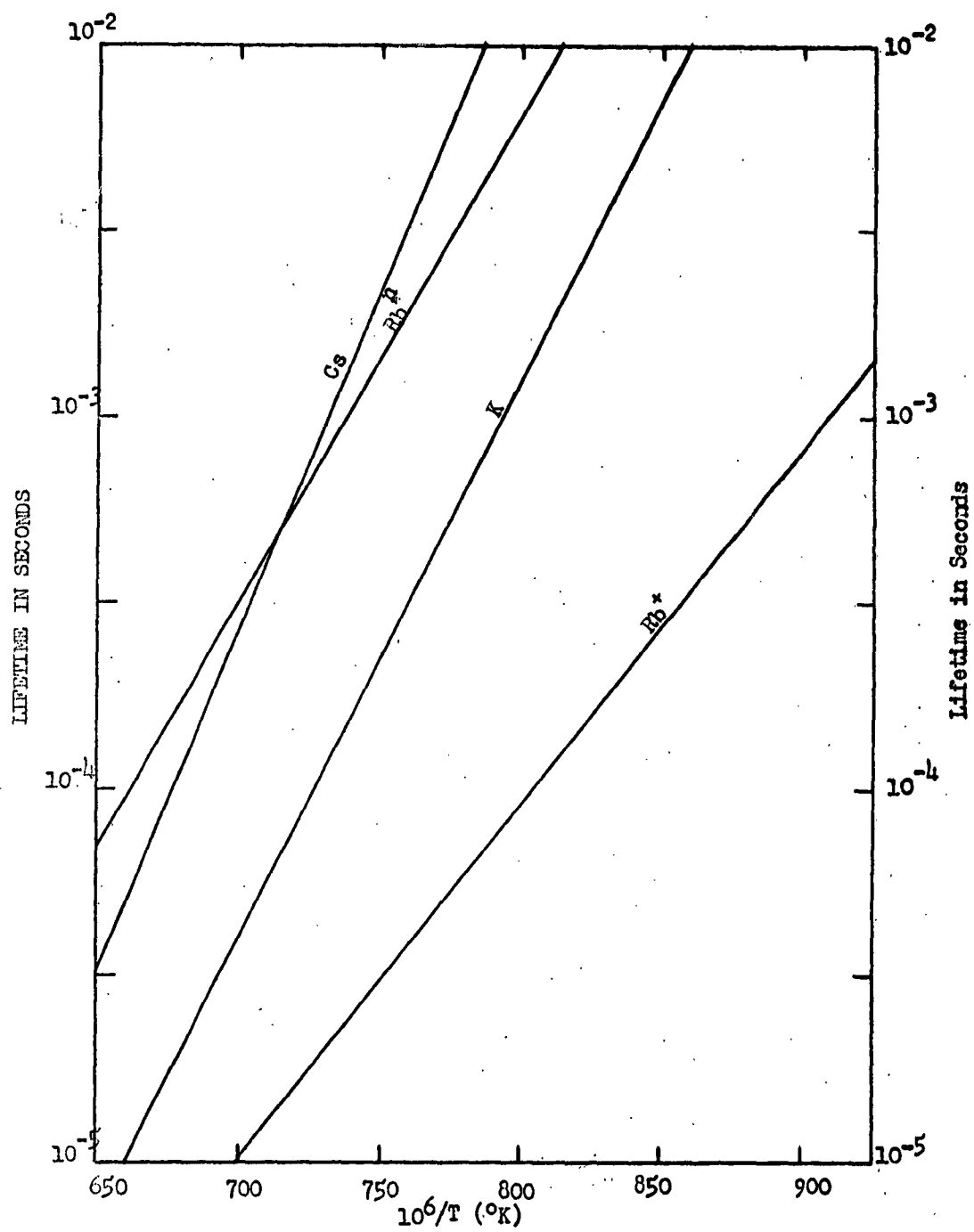
The lifetime (t) on a clean heated tungsten surface, therefore, decreases exponentially with increasing temperature. As Equation II-2 shows, it increases with the work function, so that higher work function materials need higher temperatures for equal lifetime. This is the reason platinum is less desirable than tungsten and molybdenum; the melting point limits the operating temperature.

The lifetimes for ions are shorter than for the atoms of the same substance. Hughes, et al., report values of both lifetimes for rubidium (Ref. 17). In earlier reports, Knauer (Ref. 19), Bull and Marshall (Ref. 20), and Evans (Ref. 21) reported one lifetime for both. At temperatures of 2000°K the lifetimes are estimated to be between 10^{-5} and 10^{-7} seconds for alkali metals on tungsten. The lifetime is of interest because the emitter saturation current density is inversely proportional to lifetime. Lifetimes for cesium, rubidium, and potassium are shown in Figure II-7 using available data. The effect of surface contamination is illustrated in Figure II-8.

To prevent the work function changing from that of the emitter material to that of the fuel, the surface coverage with fuel should be less than 1% of a monatomic layer of the fuel (Ref. 19). The migration time of the fuel on the emitter surface, therefore, must be short enough to prevent the build-up of a monatomic layer in excess of 1%. In considering a porous emitter, the plate can be thought of as a parallel layer of many fine capillary tubes. If the surface migration time of the fuel on the emitter surface is not high enough, the fuel concentration will exceed 1% around the ends of the capillaries and, in consequence, the work function will be reduced from that of the plate material to that of the fuel. Migration of the fuel on the emitter surface depends on the surface temperature, increasing exponentially with the temperature. Recent data on the migration time of alkali on tungsten surface are not available, although some information has been published by Becker (Ref. 22), Benjamin and Jenkins (Ref. 23), and Frank (Ref. 24). It appears that the earlier investigations were made with insufficiently clean surfaces; therefore, the measured values may not be applicable. Further experimental investigations in this field appear to be highly warranted.

The question of migration time appears to be negligible if a solid emitter surface is used and the fuel is equally distributed over the exchange plate by means of an atomic beam. To achieve this





LIFETIME ON HEATED TUNGSTEN SURFACE

Figure II-7

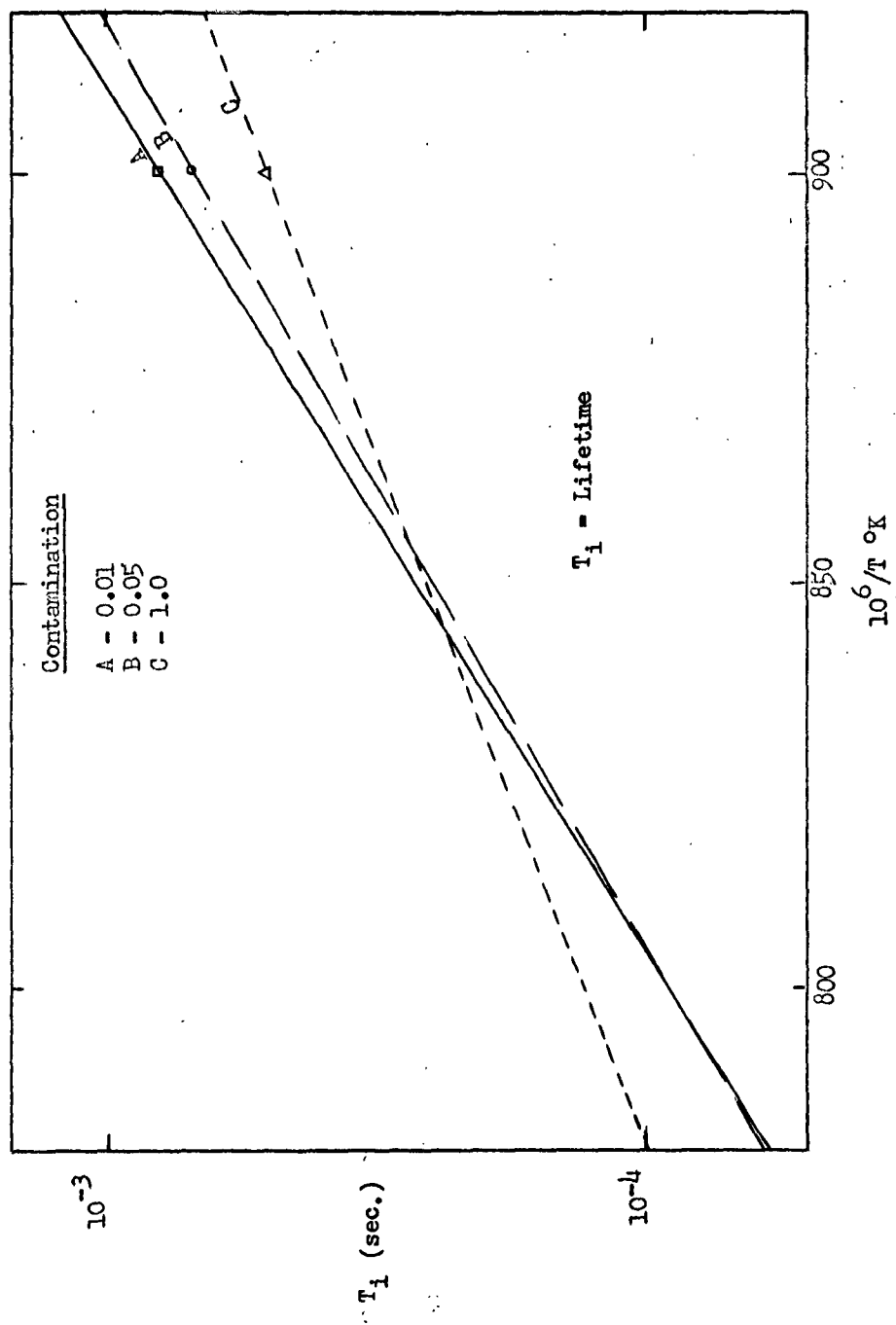


Figure II-8

LIFETIME OF Rb ATOM ON TUNGSTEN FOR VARIOUS DEGREES OF CONTAMINATION

a small angle between incident atom-beam and the plate is useful. The fuel beam gun can be built into the focusing electrode (which is at the same potential as the ion emitter) of a Pierce type accelerator. However, evaporation of the fuel from the accelerating electrode has disadvantages because of the low breakdown voltage in the alkali-vapor.

In addition to the factors of ionization efficiency, fuel lifetime on the surface, and migration velocity, the ion beam current density is also governed by the fuel flow rate through the emitter material ("through" because this experimental investigation is confined to porous plates and fine screens).

Depending on the fuel vapor pressure and on the design (and the operating conditions) of the porous plate, a certain amount of the fuel will penetrate the porous plate and be evaporated from the surface. The vapor pressures of the alkali fuels are relatively well-known, and are given as a function of temperature in Figure II-9. The pertinent equations are:

$$\text{Li} : \log p = 8.00 - 8143/T$$

$$\text{Na} : \log p = 9.235 - 0.5 T - 5567/T$$

$$\text{K} : \log p = 8.793 - 0.5 \log T - 4552/T$$

$$\text{Rb} : \log p = 10.55 - 4132/T$$

$$\text{Cs} : \log p = 11.176 - 1.4 \log T - 4042/T$$

where p is mm Hg and T is degrees Kelvin.

The above equations are taken from Ditchburn and Gilmour (Ref. 25). Earlier references include those of Eucken (Ref. 26), and Taylor and Langmuir (Ref. 9).

The flow rate through the emitter is a function of the inlet fuel vapor pressure (P_1), the mean pore diameter, and the exit pressure (P_2). At higher fuel pressures, the flow rate follows the equation for viscous flow:

$$F_v = (1.33 \pi r^4 / 8 \eta L) \left(\frac{1}{2} \right) (P_1 + P_2) \quad (\text{Eq. II-3})$$

where

$$F_v = \text{viscous flow rate, cm}^3 \text{ sec}^{-1}$$

$$\eta = \text{viscosity coefficient}$$

$$r = \text{mean pore diameter, cm}$$

$$L = \text{effective pore length, cm}$$

$$p = \text{pressure, microns}$$



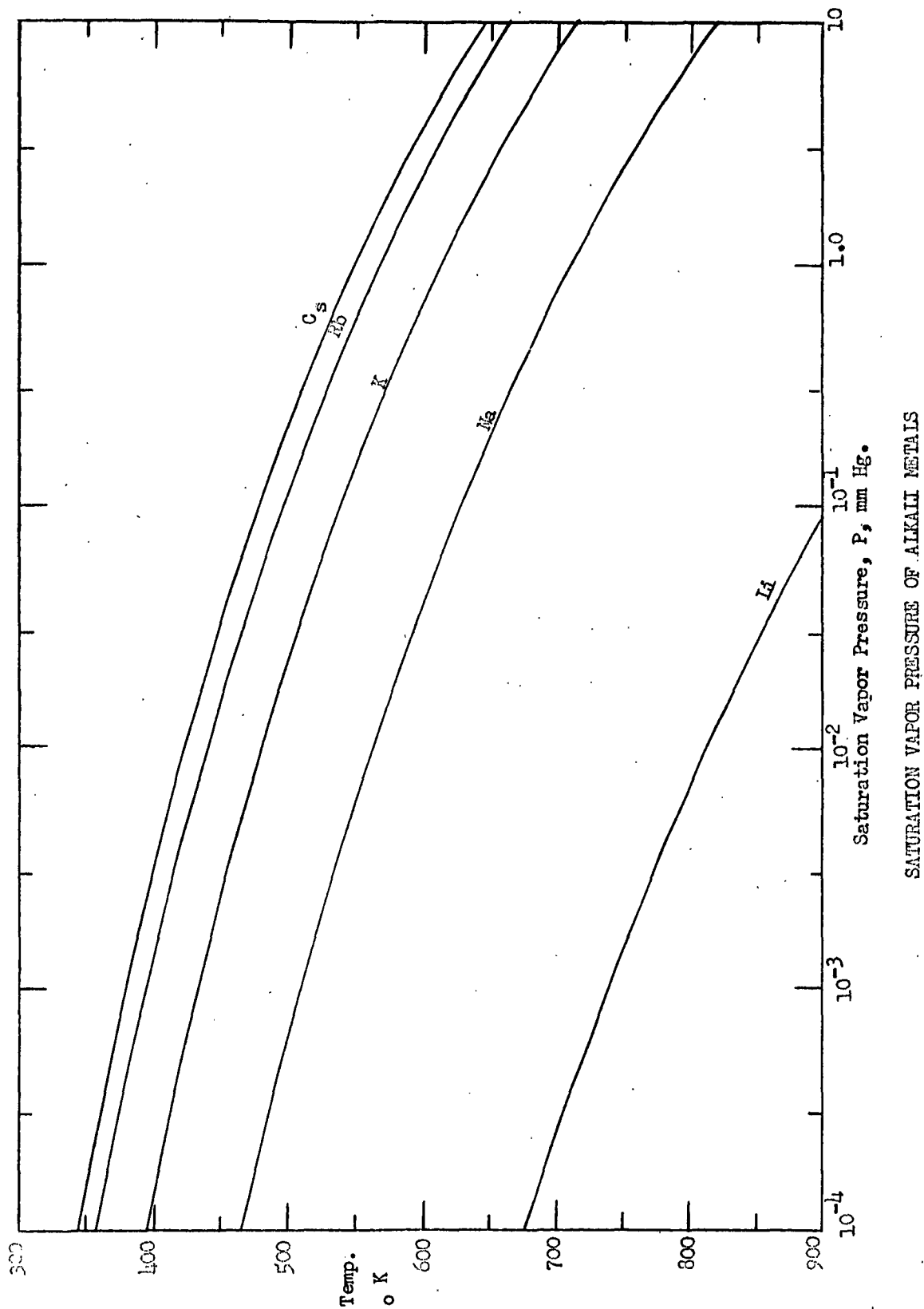


Figure II-9

With smaller pore sizes and lower vapor pressures, the flow changes from viscous flow to slip flow and subsequently to molecular flow. Molecular flow denotes the condition wherein the mean free path is equal to or greater than the mean pore diameter. The mean free path for the alkali metals as function of pressure is given in Figure II-10 for temperatures of 1200°K and 2000°K. For comparative purposes, the mean free path of helium, argon, and xenon is shown, computed using the following equation:

$$\lambda = (7.6) 10^{-17} / \pi \sqrt{L_2} (2.68) d^2 (p) \quad (\text{Eq. II-4})$$

where λ is the mean free path in cm, and

$$d = \text{atomic diameter, cm, where } d^2 = d_0^2 (1 - C/T) (1 + C/273)$$

$$d_0 = \text{atomic diameter at zero deg. C}$$

$$C = \text{Sutherland constant}$$

$$p = \text{pressure, mm Hg}$$

The equations for slip flow and molecular flow, respectively, are given below.

$$F_{sp} = \left[(1.33 \pi r^4) \left(\frac{1}{2} \right) (p_1 + p_2) / 8 \eta L \right] + \left[8 \pi r^3 v_a / 12 L \right] \quad (\text{Eq. II-5})$$

$$F_m = (8 \pi r^3 v_z / 12 L) \quad (\text{Eq. II-6})$$

When the mean free path of an atom adsorbed on the capillary surface is equal to or greater than the mean pore diameter, then surface flow also contributes to the total flow-rate, as given in Eq. II-7 for constant plate temperature.

$$F_s = F_m (1 + a) \quad (\text{Eq. II-7})$$

where

$$F_{sp} = \text{slip flow rate, cm}^3 \text{ sec}^{-1}$$

$$F_m = \text{molecular flow rate, cm}^3 \text{ sec}^{-1}$$

$$F_s = \text{surface flow rate, cm}^3 \text{ sec}^{-1}$$

$$a = (3/4) (D_s) (TS_0) / (r^2) (v_a)$$

$$v_a = \text{mean velocity, } (1.455) (10^4) (T/M)^{1/2}, \text{ cm sec}^{-1}$$

$$D_s = \text{surface diffusion coefficient}$$

$$S = \text{surface concentration of adsorbed atoms}$$



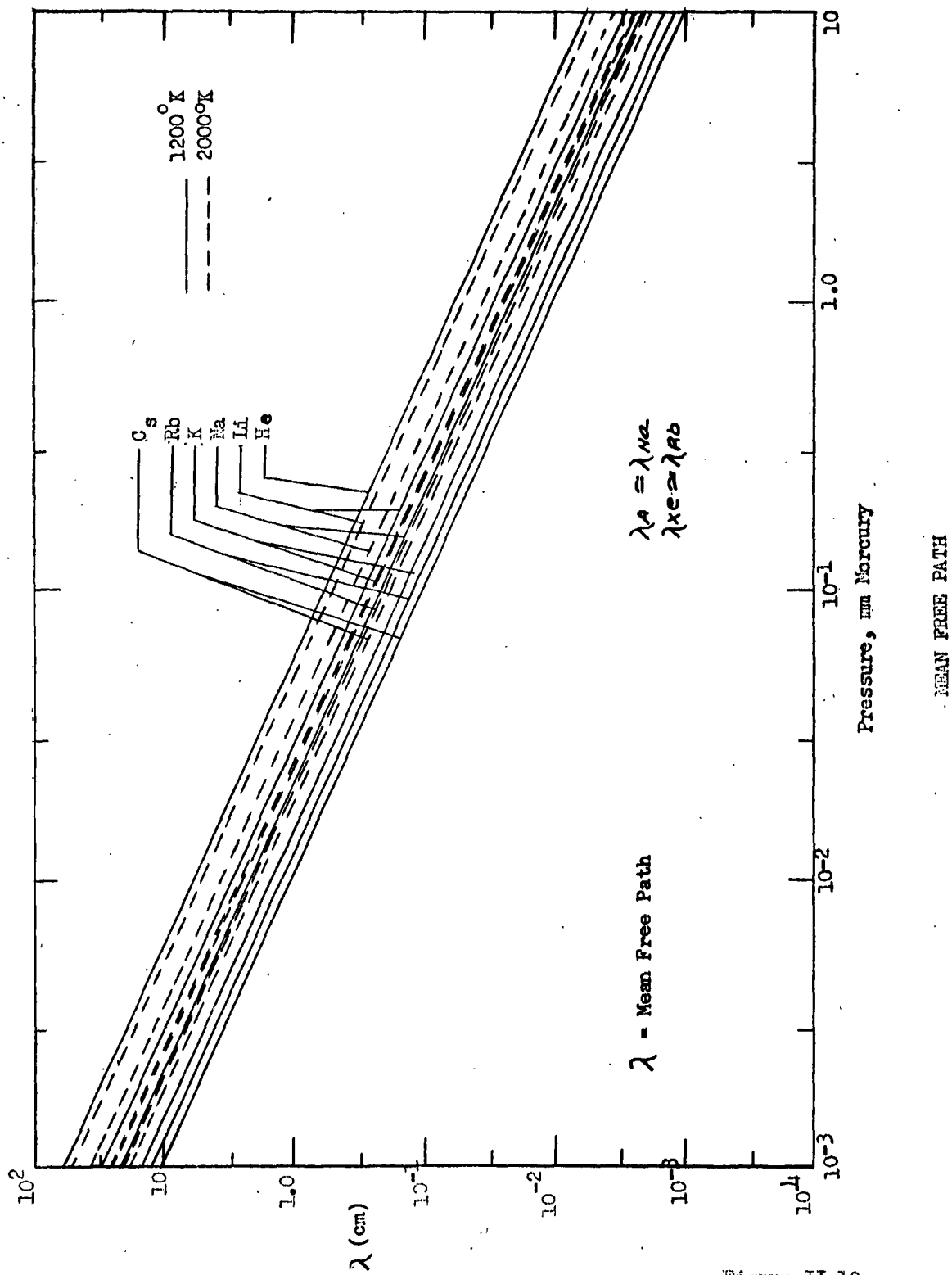


Figure II-10

θ = local surface coverage

T = temperature, deg. Kelvin

In the case of a porous emitter, the ratio of capillary length to diameter is greater than 100, so there are no corrections for short capillaries. The ratio of viscous flow to molecular flow gives the effective pore radius and, with the equation for the molecular flow, gives also the effective pore length, assuming that the capillaries are circular and that the total flow rate is not affected by surface flow. Tortuosity of the capillary and deviation from a circular shape reduce the flow rate through the capillary. It is not possible in the case of a porous emitter to distinguish between the length and the shape of the capillary.

As will be discussed later in the section on "Diffusion Experiments," the emitter (porous or screen) can be calibrated for flow at various differential pressure conditions. Briefly, the emitter is connected on the inlet side to a container of constant volume filled with an inert gas (such as helium); the exit side is evacuated. Using a flow measuring apparatus, the dependence of flow rate on plate temperature, pressure differential, and fuel atomic weight can be determined and utilized in the design of the ion source.

As shown in Figure II-11, the total flow rate per unit (F_m) is proportional to $1/T^2$ and to r ; whereas the surface flow rate is proportional to $1/r$.

Another factor which mitigates in favor of a high beam current density is the smaller emitter area which results, and the reduced power loss due to spatial heat radiation. It has already been shown that high emitter temperatures are required for efficient ionization, between 1100°K and 2000°K. The heat loss by radiation increases rapidly with temperature. For example, Figure II-12 shows power loss as a function of emissivity and temperature. Values of total emissivity between 0.12 and 0.20 are reported for tungsten in the temperature range of 1100°K to 1500°K (Ref. 27).

It is also advantageous to limit the radiating area to the emitter surface itself; i.e., with a minimum "seeing" angle. Sideways emission can be reduced in part by radiation shielding. For example, if there are n thin metal shields of the same emissivity between parallel walls, then the energy loss reduces to:

$$E = \sigma (F) (\epsilon) (T_1^4 - T_2^4) / (1 + n) \quad (\text{Eq. II-8})$$

where

E = watts per sq cm

$\sigma = 5.67 (10^{-12})$



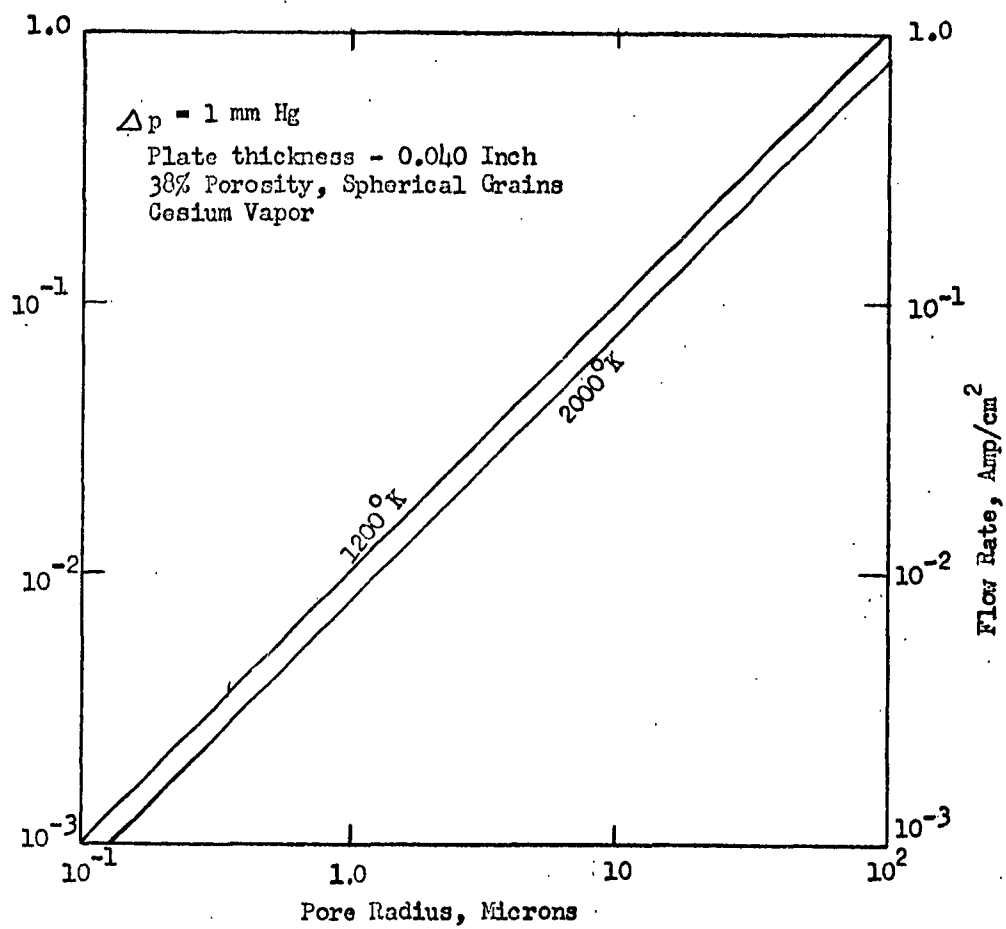


Figure II-11

FLOW RATE AS A FUNCTION OF PORE SIZE AND EMITTER TEMPERATURE

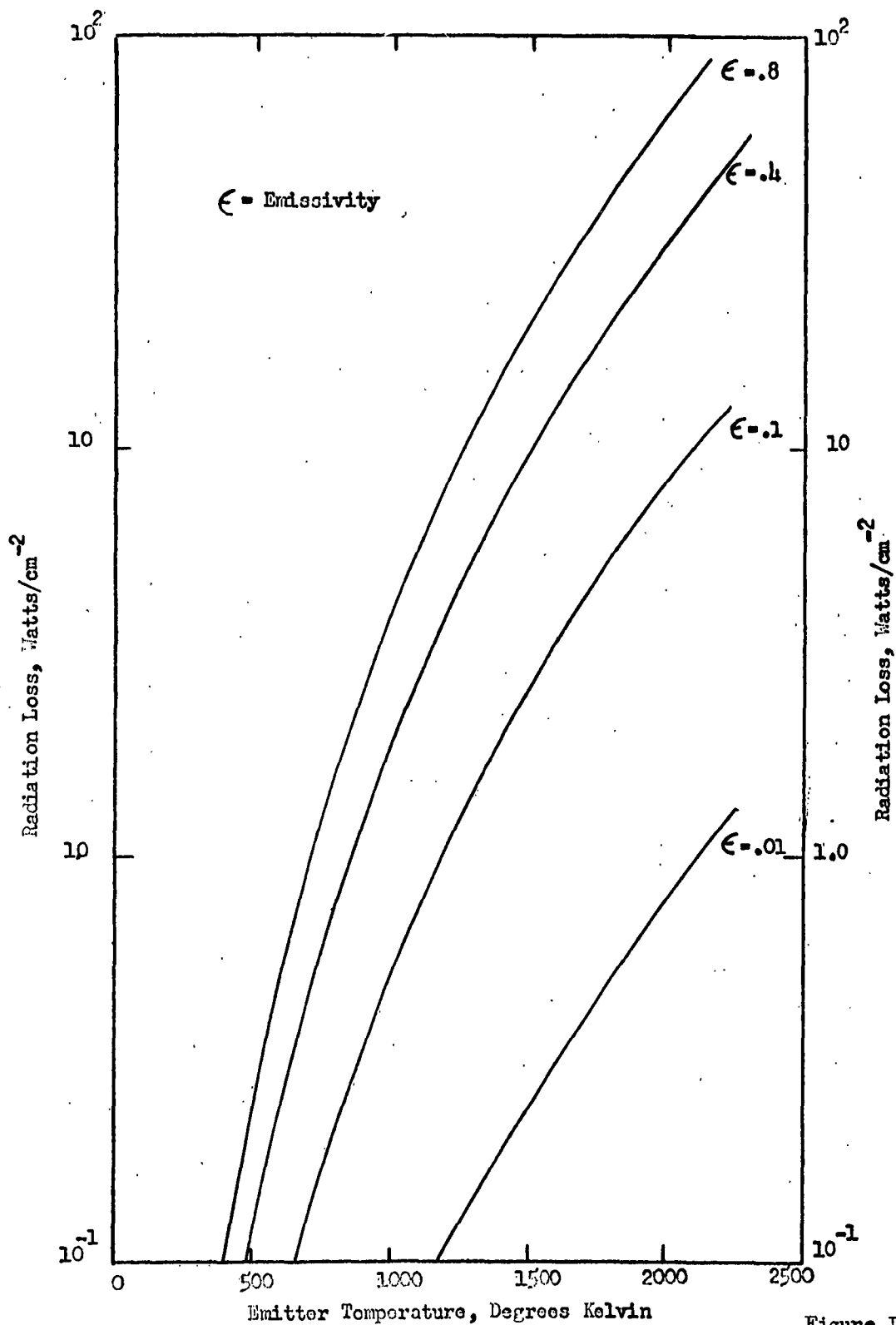


Figure II-12
HEAT LOSS BY RADIATION TO SPACE AS A
FUNCTION OF EMITTER TEMPERATURE AND EMISSIVITY, NEGLECTING SOLAR RADIATION

F = surface area, cm^2

By proper shielding, the thermal radiation loss from the emitter can therefore be reduced. The overall loss, as indicated previously, can be further reduced by utilizing a minimum emitter surface, or correspondingly a high current density.

The production of an ion beam is governed not only by the fuel flow rate through the emitter and the emitter temperature, but also by the capacity of the ion extraction and acceleration systems. The ion current is space-charge-limited in accordance with the Child-Langmuir law:

$$j = (5.45) (10^{-8}) U^{3/2} / (d^2) (m_1^{1/2}) \quad (\text{Eq. II-9})$$

where

j = ion current density, amps cm^{-2}

U = accelerating potential, volts

d = spacing between emitter and accelerating electrode, cm

m_1 = atomic weight

Figure II-13 illustrates for cesium the dependence of the current density on the electrode spacing at various accelerating voltages. The space-charge-limited current density attainable for various fuels and accelerating voltages is given in Figure II-14, assuming an electrode spacing of 10mm. A reduction in the spacing between the emitter and the accelerator electrode sharply reduces the required voltage, but, on the other hand, a lower limit exists for this spacing. The limit is governed by field emission of electrons from the accelerating electrode. Field emission can be reduced by increasing the electrode work function. An approximation for the minimum electrode distance in centimeters is given by the equation:

$$d_{\min} = U / (10^5) (a) \quad (\text{Eq. II-10})$$

where 'a' is 1.70 for rounded polished nickel electrodes, U is expressed in volts, and equation II-10 pertains to pressure levels less than 10^{-4} mm Hg. The minimum radius for edges on the electrodes in areas of high field gradients is as follows:

$$r_{\min} = U_{kv} / 20 \quad (\text{Eq. II-11})$$

where r_m is the radius in mm and U_{kv} is the accelerating potential in kilovolts. The use of values of r_m less than 0.2 is not recommended.

Cesium deposition on the acceleration electrode (by neutrals or ions) reduces the electrode work function and increases the possibility of electron field emission, as indicated in Figure II-15. Voltage break-

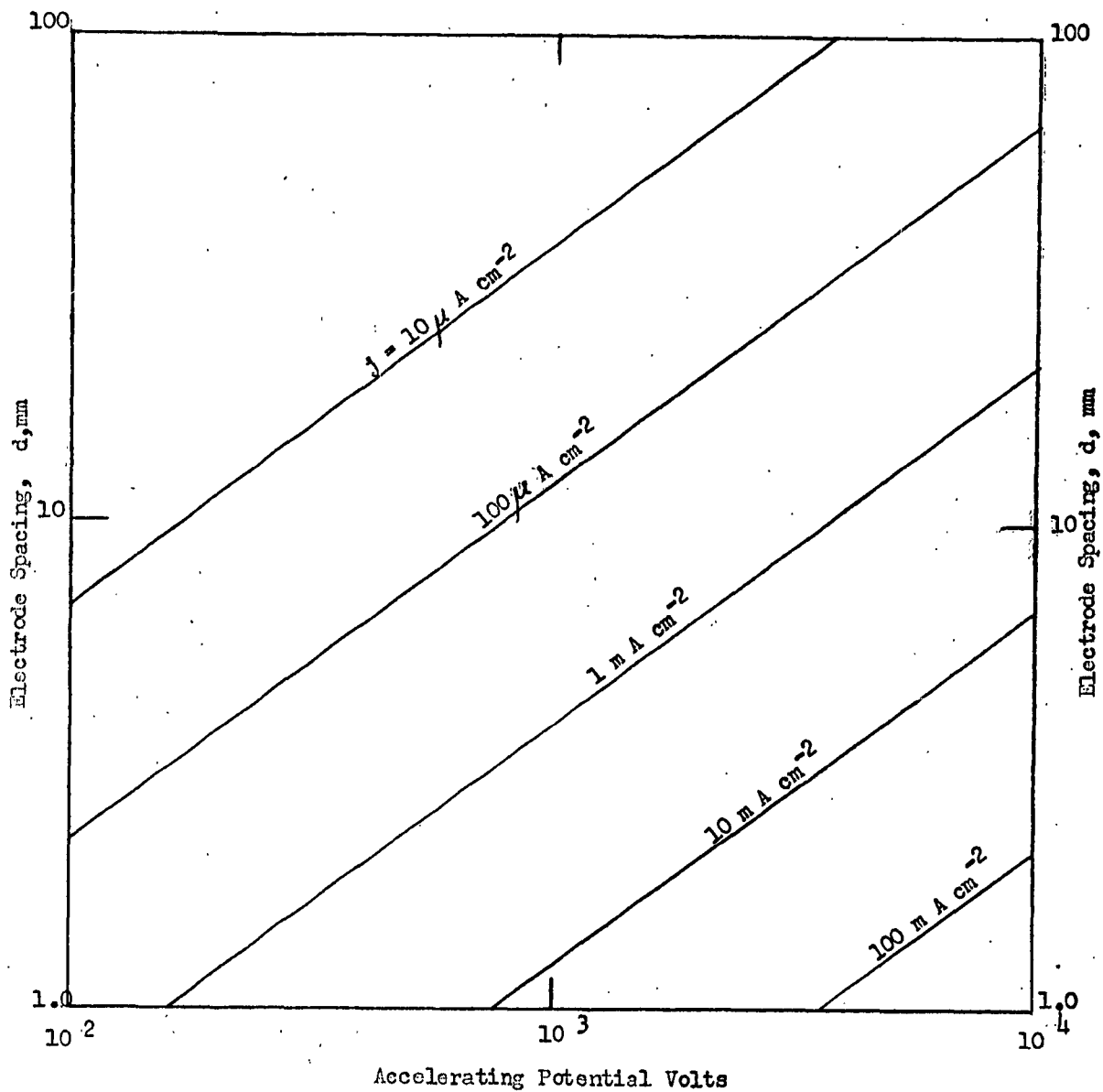


Figure II-13

EFFECT OF ELECTRODE SPACING FOR PLANE ELECTRODES

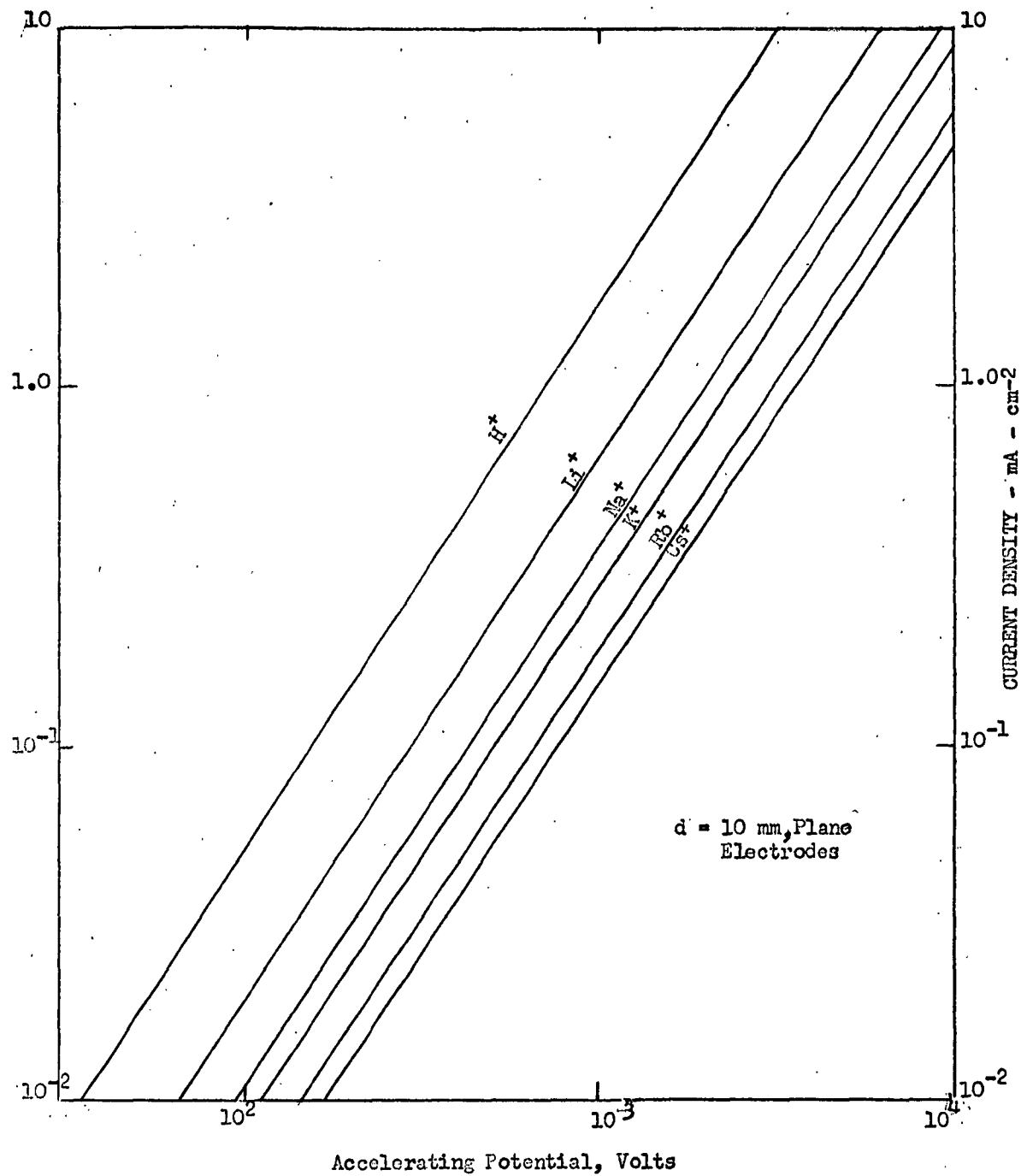


Figure II-14

EFFECT OF FUEL MASS ON CURRENT DENSITY

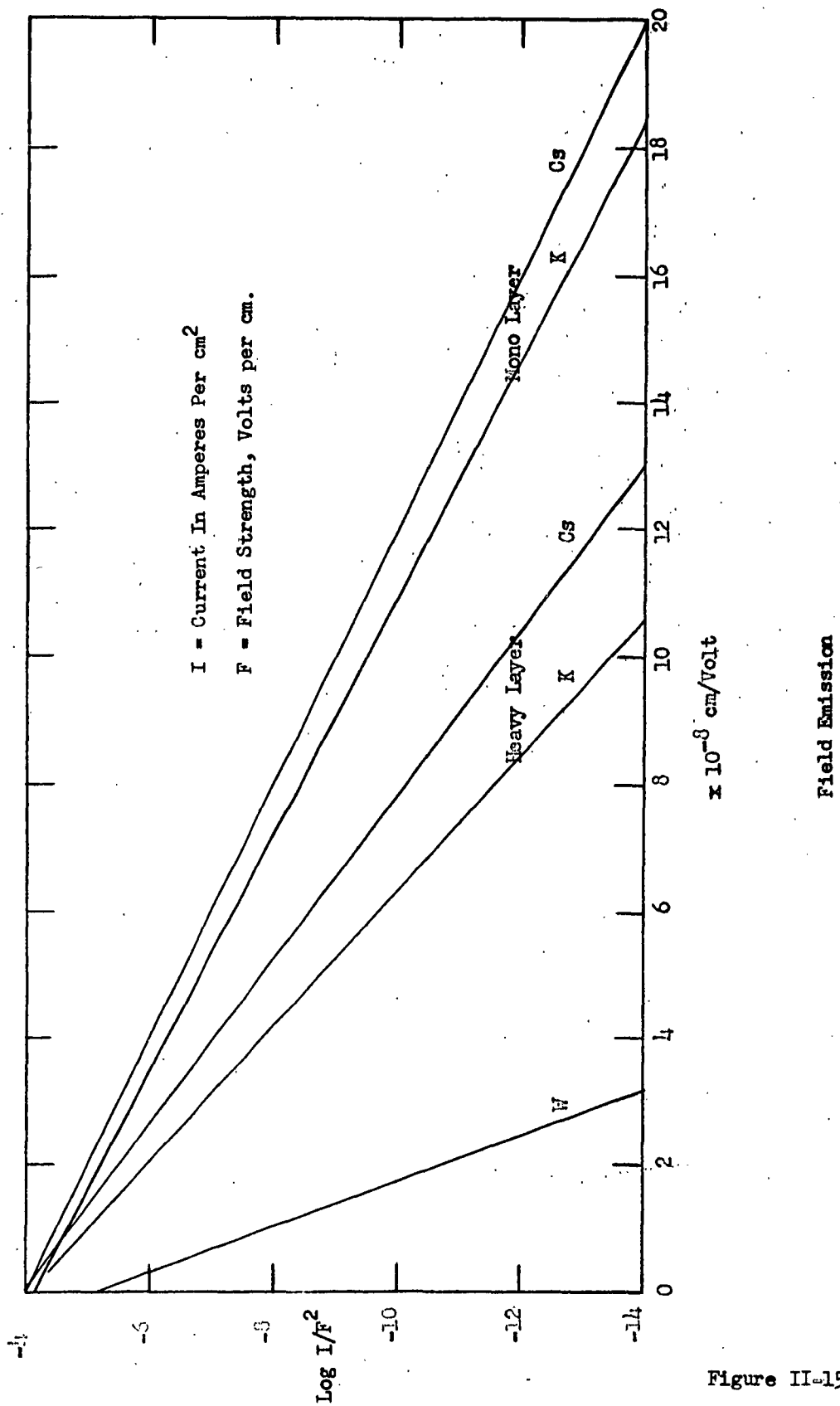


Figure II-15

down in cesium vapor appears not to be a problem if a sufficiently high vacuum (low pressure) is available.

At higher current densities, the beam tends to spread due to the beam space-charge effect. If (or when) the ions impinge on the electrode, material is sputtered with a loss both in fuel and in electrode material. Sputtering has been discussed by Wehner (Ref. 28), Goldman, et al., (Ref. 29), Bruenne (Ref. 30), and Waters (Ref. 31), among others. Following Wehner, the sputtering rate of molybdenum appears to be relatively low. Furthermore, molybdenum has a high melting point and appears to be a good choice for electrode material. Extrapolation of the sputtering ratios for mercury given by Wehner indicate that the sputtering effect must be minimized in order to provide long life for the extraction-acceleration system.

A "conventional" method of focusing and accelerating the ion beam is the Pierce method (Ref. 32). Such a system is limited to a perveance of approximately 10^{-7} , where the perveance is given by the equation:

$$P = (m_i/m_e)^{1/2} (I)/U^{3/2} \quad (\text{Eq. II-12})$$

where

P = perveance

m_i = ion mass

m_e = electron mass

I = beam current, amps

U = accelerating potential, volts

Perveances greater than 10^{-7} can be obtained by using a combined electrostatic and magnetic field, in accordance with Hines (Ref. 33), Von Duzer and Brewer (Ref. 34), and Fox (Ref. 35). These types of acceleration systems are being further analyzed.

The preceding discussion on sputtering and beam focusing-acceleration is pertinent to the ion source investigation because the various sources can be evaluated and compared only if the beam is collected and measured. An acceleration system is also required, of course, in a complete propulsion system. A consideration less germane to the source itself but unquestionably pertinent to the ultimate application is the problem of beam neutralization. The term "problem" is apropos, a considerable effort on beam neutralization has been and is being expended by various agencies (Ref. 36). Briefly, if a continuous stream of positive ions is being ejected, the same amount of the negative charge will remain in the system. Coulomb forces are built up and eventually will compensate the acceleration force. Therefore, it is necessary to eject the same number of negative charges with the positive ions. The

question is how and where the ejection should occur, depending in some measure on the beam diameter and acceleration gap. It would appear that electron injection directly into the beam is to be preferred, but the mechanism of mixing high-mass low-velocity ions with low-mass electrons has yet to be fully developed. This problem is also under consideration, although not as an integral part of the present program on ion sources. Figures II-16 and II-17 illustrate the potential drop in the radial and longitudinal direction of an unneutralized beam. The potential drop indicates that injected electrons will be accelerated toward the center of the beam and toward the emitter plate.

It has been shown in the preceding discussion on the charge exchange method of ionization, that alkali metal fuels in contact with high temperature metals such as tungsten, molybdenum, rhenium, and platinum can provide a high ionization efficiency. The discussion also has included detailed consideration of such factors as diffusion flow through the emitter, migration velocity, atom and ion lifetimes, and emitter temperature effects. From the application viewpoint, brief mention has been made of sputtering, acceleration, thermal radiation losses, and beam neutralization, which are not principal areas of investigation in the present program. Other ion sources, principally the RF and plasma arc methods, are described in the following sections.



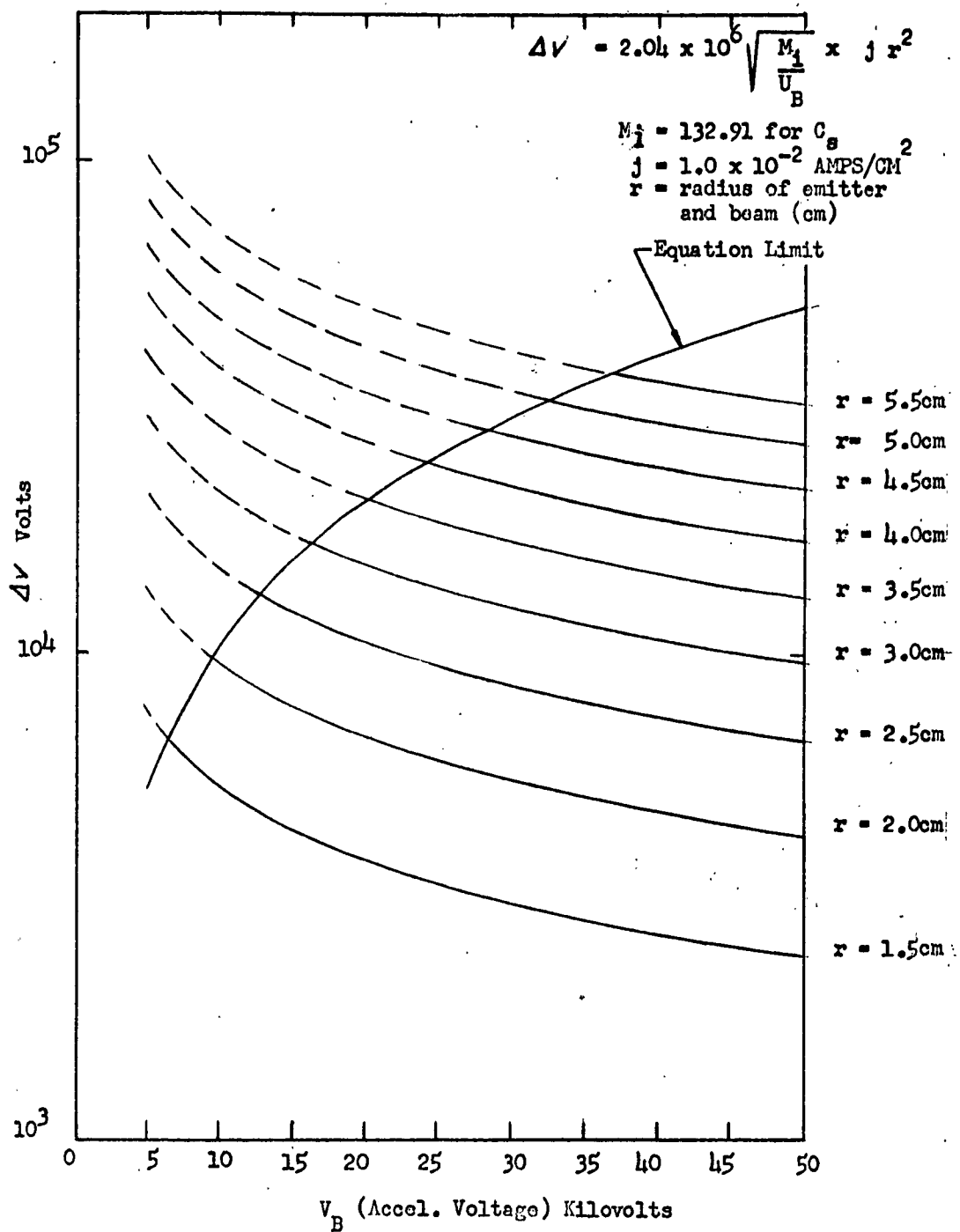
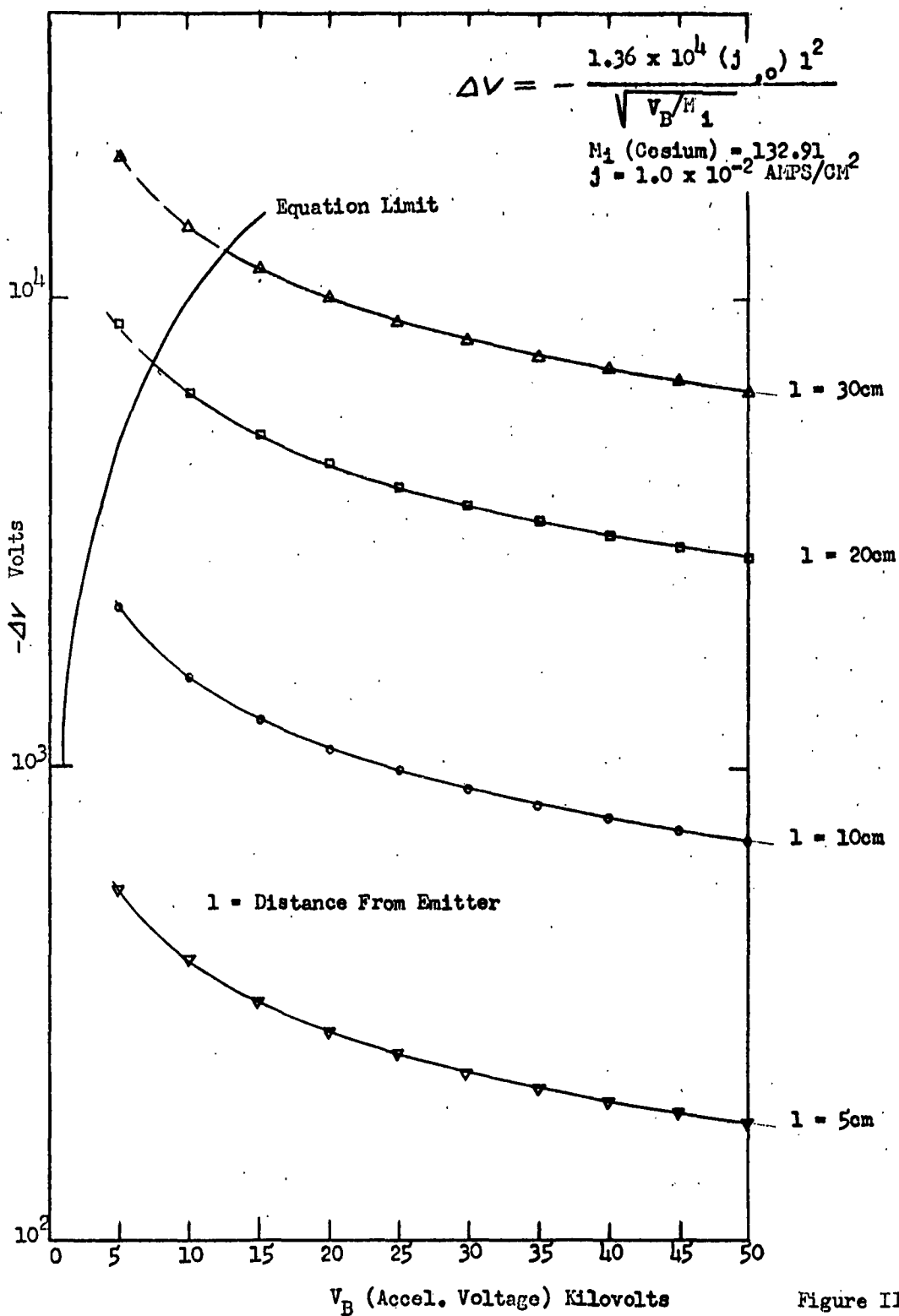


Figure II-16

RADIAL POTENTIAL DROP IN A CESIUM ION BEAM



V_B (Accel. Voltage) Kilovolts
 LONGITUDINAL POTENTIAL DROP IN A CESIUM ION BEAM

Figure II-17

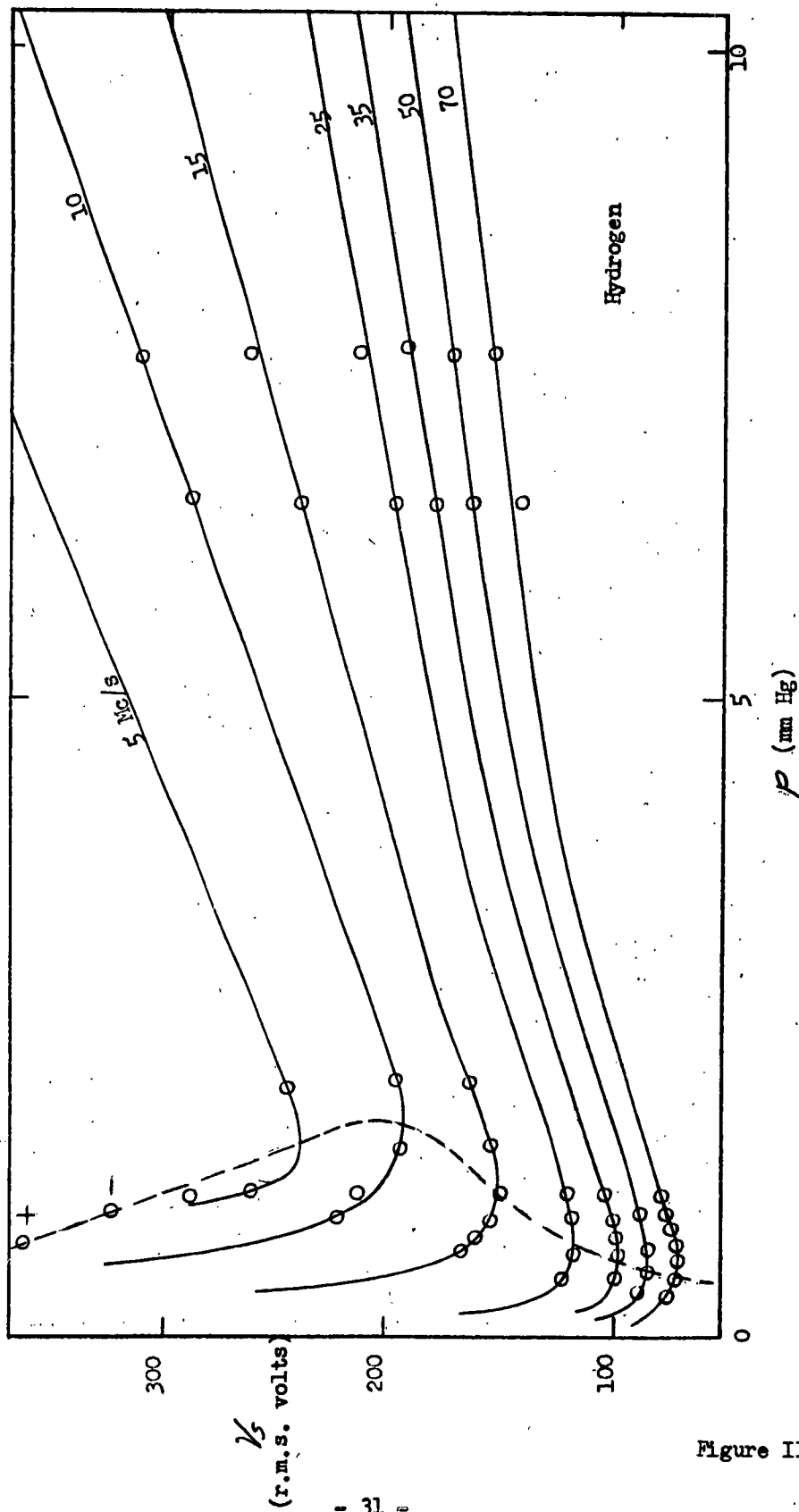
B. The RF Ion Source

Briefly stated, ionization can be obtained by subjecting the fuel vapor (e.g. cesium vapor) to a radio-frequency field. For a typical installation as discussed later in Section X of this report, the vapor is enclosed within a glass container which is surrounded by external RF coils. The ions are extracted from the plasma boundary in the end of the container.

The mechanism of the RF ionization can be described briefly as follows. For ignition a certain amount of rest-ionization (as given in part by environmental cosmic radiation) is essential. The RF field (primarily the magnetic field component to prevent dielectric losses in the walls of the container) causes the electrons to be accelerated and to ionize the low density gas or vapor. Before the ions reach the wall of the container, both the field direction and also the electron direction change. The breakdown potential follows the Paschen law (shown in Figure II-18) and decreases with increasing frequency. The operating frequency is in the range of 1.0 to 100 Mcps as shown in Figure II-18.

In the discharge area a luminous plasma is formed and serves as the source of ions. To extract the ions an electrostatic field is superimposed over the discharge area. In front of the negative extraction electrode a dark area is formed with a depth depending upon the applied potential and the plasma density. Inside the plasma tube, at some distance from the extraction electrode, the extraction field is screened by the positive space charge. The luminous plasma boundary is thus the ion-emitting surface. The dark area before the extraction channel is free of electrons and, therefore, also free of recombinations.

Inasmuch as the vapor pressure in the plasma is less than that used in other types of discharges, the extraction channel (aperture) can be larger, resulting in higher current densities. Typical pressures in the RF discharge are in the range of 0.1 to 5.0 microns. Application of a longitudinal or transverse magnetic field to the RF discharge increases the plasma density, permitting lower gas or vapor pressures. Neuert, et al., investigated the effect of a magnetic field on the discharge (Ref. 37). Fundamental studies on the RF ion source were performed by Thoneman (Ref. 38), Hall (Ref. 39), Neuert (Ref. 40), Chenot (Ref. 41), and Swann and Swingle (Ref. 42). Improvement over the first extraction systems was accomplished by Moak, et al., (Ref. 43) and in particular by Reifenschweider (Ref. 44) and Sommeria (Ref. 45 and 46). Reifenschweider investigated the extraction channel with the result that the channel diameter can be increased and the channel length decreased due to the beam crossover in the channel. At the crossover point only a small aperture is necessary. Sommeria investigated the plasma-channel extraction conditions and showed good results by the arrangement of an electrostatic



BREAKDOWN IN R F FIELD WITH ELECTRODES OXIDIZED

Figure II-18

lens with its focal point in the aperture. Other investigators including Moak used a magnetic field for confinement of the ions coming from the plasma boundary, thereby increasing the ion current and focusing it in the channel. Beam spreading behind the extraction channel is prevented by use of an ion condenser (Figure II-19), with the effect shown in Figure II-20. The increase of ion current by use of a transverse magnetic field is shown in Figure II-21.

The experimental technique used in the present program is described further in Section X of this report.

C. The Plasma Arc Source

The problem as previously cited is the ultimate production of a copious supply of heavy ions amenable to electrostatic acceleration.

The development of such an ion source and the evaluation of its performance requires that a number of basic problems in plasma physics be considered. The ionization, diffusion, and recombination processes in a plasma must be studied to obtain a suitable ion source. Additional problems involving plasma sheaths and ion optics are inherent in methods to extract ions from the source and to accelerate them. Fortunately considerable literature exists on ion source development for high energy accelerators, mass spectrographs, and, recently, the magnetic mirror fusion devices. It is readily apparent from this literature that the detailed processes in electric discharges are not completely understood. However, many useful experimental techniques have evolved and several types of ion sources have been produced which have been successful for their purpose.

The ion source should be designed for the utmost in efficiency and dependability. An obvious parameter to be considered in determining the ion source efficiency is the ion current/source weight ratio. The total weight relating to source operation, however, is a complex consideration depending as it does on the power supply as well as source design. For the present, the emphasis will be placed on developing a larger ion current. It appears that the problem of power efficiency rests primarily with the prime power supply for the acceleration mechanism and for the overall device. The power used for ionization is negligible, even if the process is inefficient. Existing sources have a power efficiency on the order of 1%. Cesium ions requiring 3.87 ev for ionization and subsequently accelerated to at least 10 kev energy could thus be used at about 96% efficiency (for the overall system) if no other losses were encountered.

Likewise the fuel waste involved in neutral atom loss must be analyzed in terms of the overall device weight. For each ampere of ion current about 1 milligram/second of cesium would be ionized and ejected. Carrying a comparable amount of fuel to be wasted would probably not

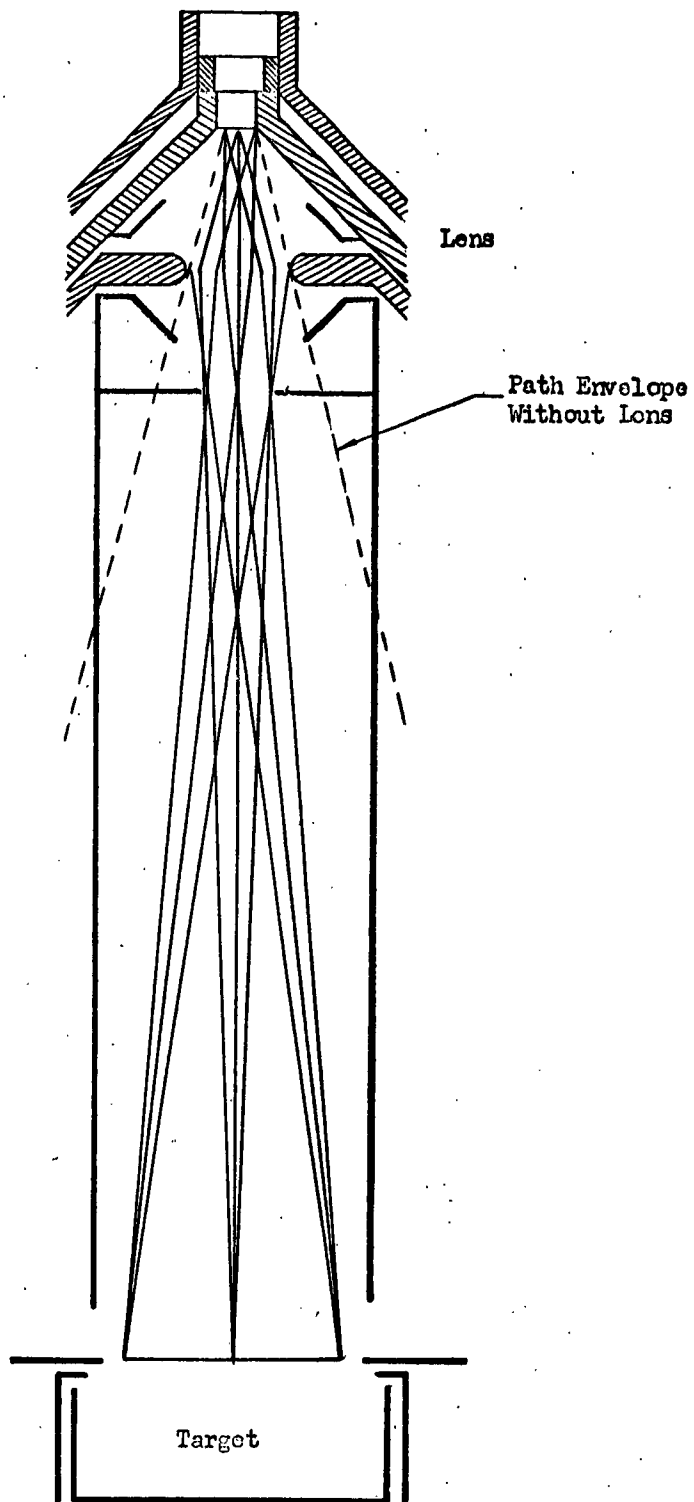
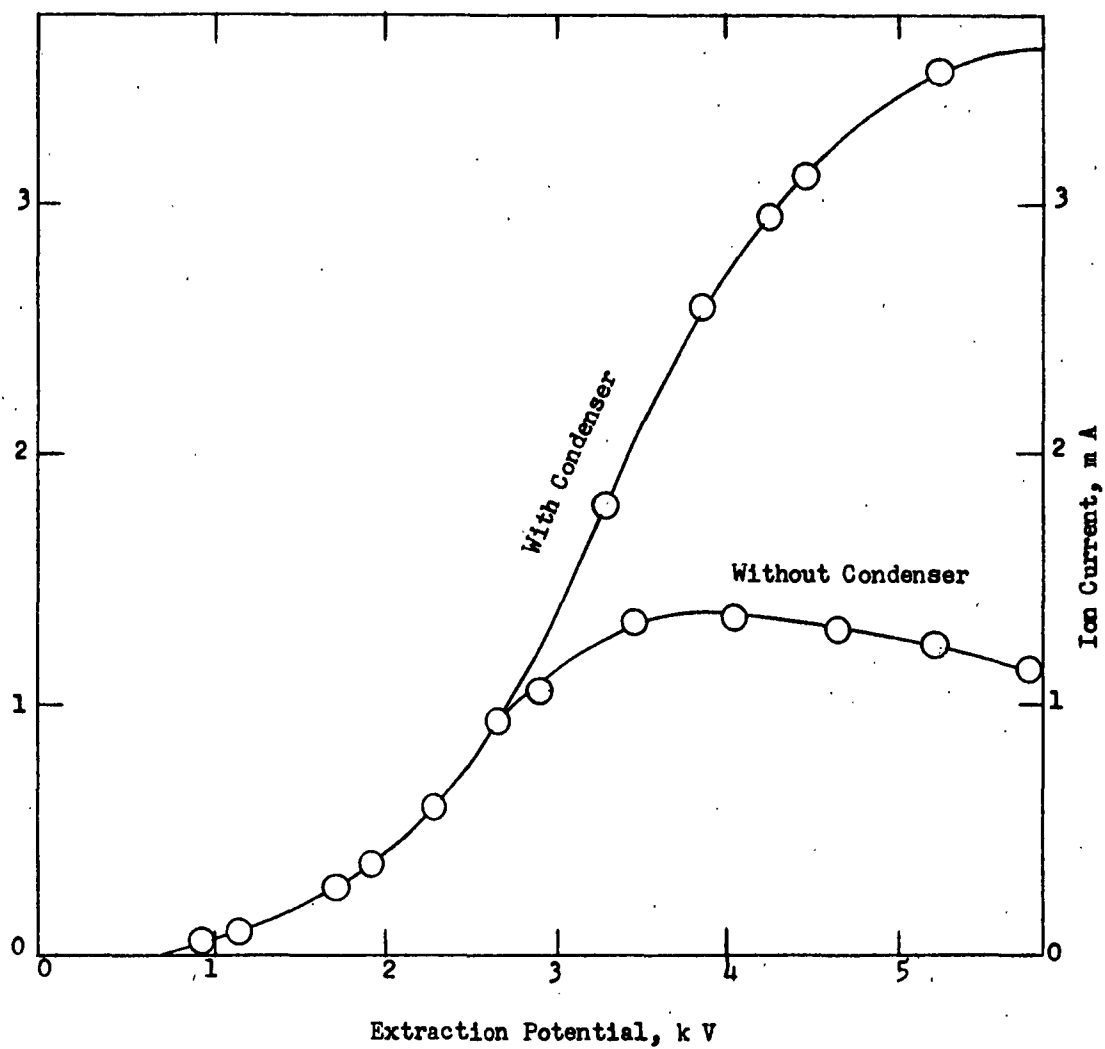


Figure II-19

ION CONDENSER SYSTEM



EFFECT OF ION CONDENSER

Figure II-20

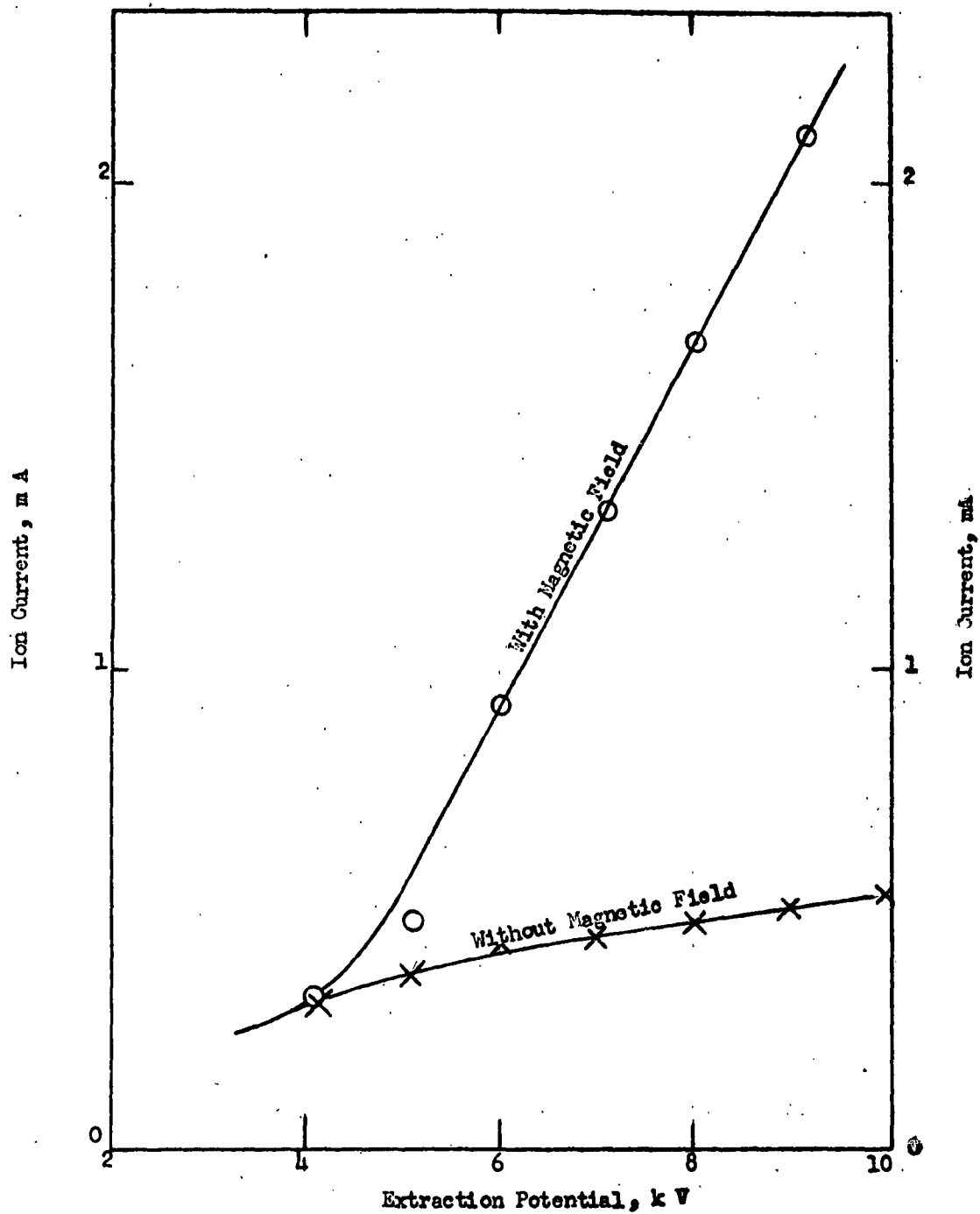


Figure II-21
EFFECT OF MAGNETIC FIELD
(TRANSVERSAL)

be a burden except for long-period operation. However, if these neutrals became ionized in the accelerating system, they would constitute a source of electrons which would parasitically load the power supply. A plasma sheath might also be established which would shield the ions from the accelerating field.

It appears that reliability should become a prime consideration in the ion source. Ease in starting the ion source, stability, and structural durability will be of crucial importance. In particular, those sources utilizing components subject to sputtering are not desirable. The choice of fuel should also be considered in this connection. The advantage of a low ionization potential for an element in a high temperature ion source may be overshadowed by the high chemical activity and the vapor condensation problems with an alkali metal. Experiments on the ionization of cesium will in any case be of interest.

A large number of ion sources in existence have been described recently by Von Ardenne (Ref. 47). The Duoplasmatron developed by Von Ardenne has excited considerable interest and this type of source is being tested at Oak Ridge National Laboratory and at Livermore for use in Project Sherwood fusion devices (Ref. 48 and 49). Von Ardenne's data for this source are as follows: maximum ion current, one ampere of protons with 7 ampere arc current at 120 volts and extraction aperture of 1 mm diameter. The power efficiency in the ionization process was thus about 1.5%. Investigators in this country have experienced difficulty in improving on the results. Filament life continues to be a problem and backstreaming electrons and negative ions in the extractor region require special care if power loss and sputtering problems are to be avoided. An important feature of this arc is the magnetic and electrostatic compression which makes the ionization process especially efficient near the extractor.

The Oak Ridge and Livermore laboratories are working also on a hot cathode arc which is somewhat similar to the Duoplasmatron but requires several hundred amperes arc current. This source is also operated in a magnetic field, but does not utilize the compression features of the Duoplasmatron. Operation is on a pulsed basis with several amps beam current extracted at the anode for use with the magnetic mirror fusion device (Ref. 50).

A similar grid ion source has been developed at Oak Ridge for continuous operation.

A DCX type arc developed at Oak Ridge has been suggested as a powerful ion source (Ref. 51). Observation of 20 amperes of backstreaming ions which strike the cathode has been interpreted to mean that electric fields exist within the arc and accelerate the ions to the cathode sheath. This observation is in agreement with the theory of positive ion collection by probes which shows that the

ions should arrive at the probe sheath with an energy of about $1/2 kT_e$ (Ref. 52). The ion temperature of the arc measures from 10 ev to 50 ev and the drift energy of the ions toward the cathode is about 2 ev (Ref. 53). The arc current was 300 amperes.

It had originally been proposed in the present program to conduct experiments on the plasma arc seeded with cesium to ascertain its capabilities as an ion source. The preceding discussion has indicated the considerable effort currently being expended by the AEC on arc devices at the high ion current densities which can be obtained. In Section XI of the present report several proposed experimental arc devices are described. In addition, the methods of ion extraction and diagnostics are discussed.



III. TYPES OF CONTACT EMITTERS

Three types of contact emitters are being evaluated. In each case, the cesium vapor is passed through the emitter. In order to provide maximum ionization efficiency, the use of (relatively) large mesh screens and grids has been ruled out, by the same reasoning as applied to the effort in this program in eliminating by-pass flow around the edges of the emitter.

Emitters with the smallest possible flow passages were obtained, including porous tungsten plates, platinum screens, and molybdenum screens. The specifications are given below.

A. Porous Sintered Tungsten

Items	Plate Thickness (in.)	Powder Size (Microns)	Apparent Density(%)	Porous Volume(%)	Sintering Temp.(°K)
F-1	.050	4.0-5.0	58	42	1700
F-2	.030	4.0-5.0	58	42	1700
C-1	.104	6.0-7.0	52	48	1725
P-1	.060	0.5-10.0	83	17	2675
P-2	.040	0.5-10.0	83	17	2675
P-3	.020	0.5-10.0	83	17	2675

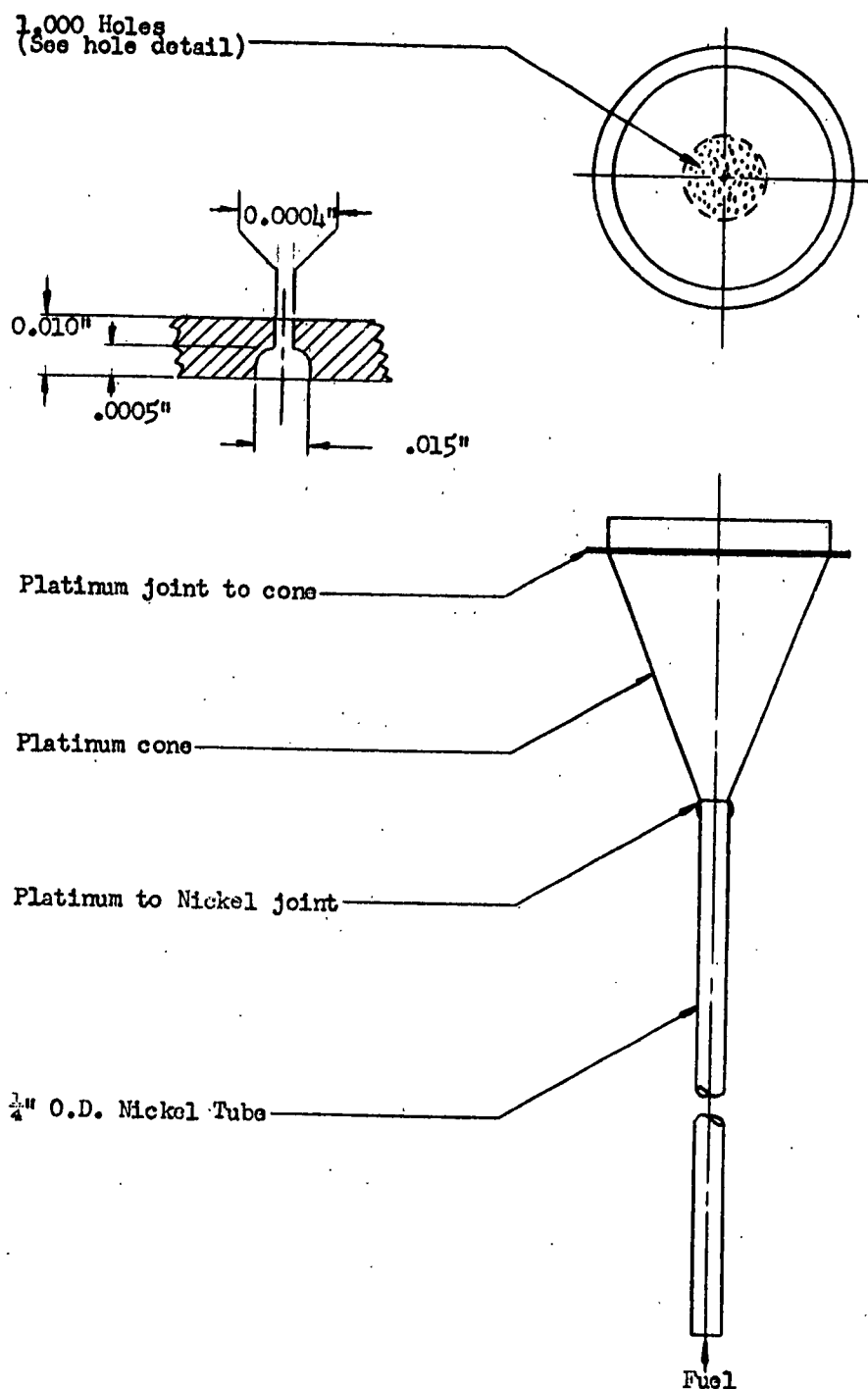
In the first series of tests, the evaluation includes Items F-1, C-1, and P-1. These are sufficient to provide an initial cross-section of plate types and the effect on performance.

Further confirming data with the remaining tungsten plates will be obtained later.

B. Mechanically Perforated Platinum Screen

The platinum screen was obtained in the form of a complete "spinerette," the general shape and form being almost identical to that used as a commercial spinerette for forming viscous rayon and artificial fibers. A sketch of the configuration is shown in Figure III-1. As can be seen from this sketch, 1000 holes are punched into the center of the emitter plate. The photograph in Figure III-2 is a front view of the emitter showing the circular location of the holes. In order to keep the diameter of each hole as small as possible it was decided not to polish the outer surface of the emitter, thus leaving a rough ring around each of the punched holes and reducing the apparent diameter





PLATINUM EMITTER

Figure III-1



Figure III-2. Platinum Emitter

of the holes from a nominal 0.001 in. to approximately 0.0004 in. As may be seen on the inset in Figure III-1, the actual holes through the platinum are not direct but rather bell-shaped, with the small punched hole leading from the apex of the bell to the emitter surface. The prime advantage of this fabrication is that the complete assembly is made from platinum with platinum-fused joints. Leakage is not a problem.

C. Electro-Formed Molybdenum Screen

Several types of screens were considered for application to the ion source. The conventional woven screen appeared to provide too wide a variation in the size of openings, even though the size of openings can be reduced by mechanical rolling.

An electro-etched tungsten screen with uniform hole sizes can be obtained, but the minimum hole size is 0.005 in., which is considered somewhat large. Therefore, an electro-formed screen made of molybdenum is being used; a photograph of the screen is given in Figure III-3. The screen is 0.001 in. thick, with a solid rim for bonding into a holder. The holes are 0.003 in. in diameter and are located on 0.010-inch centers. At the present time, additional screens of the same type are being obtained, with hole sizes of 0.0015-inch diameter.

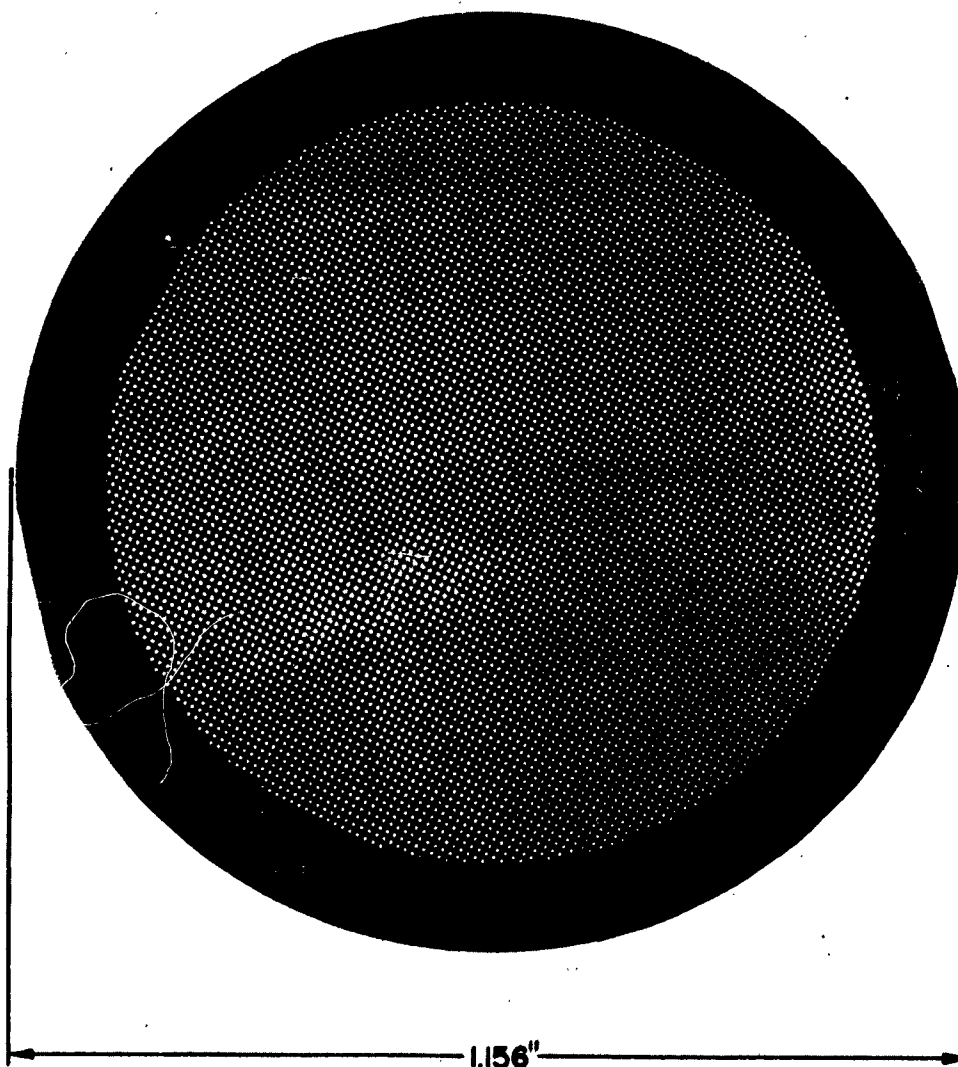


Figure III -3. Photograph of Molybdenum Screen

IV. DIFFUSION EXPERIMENTS

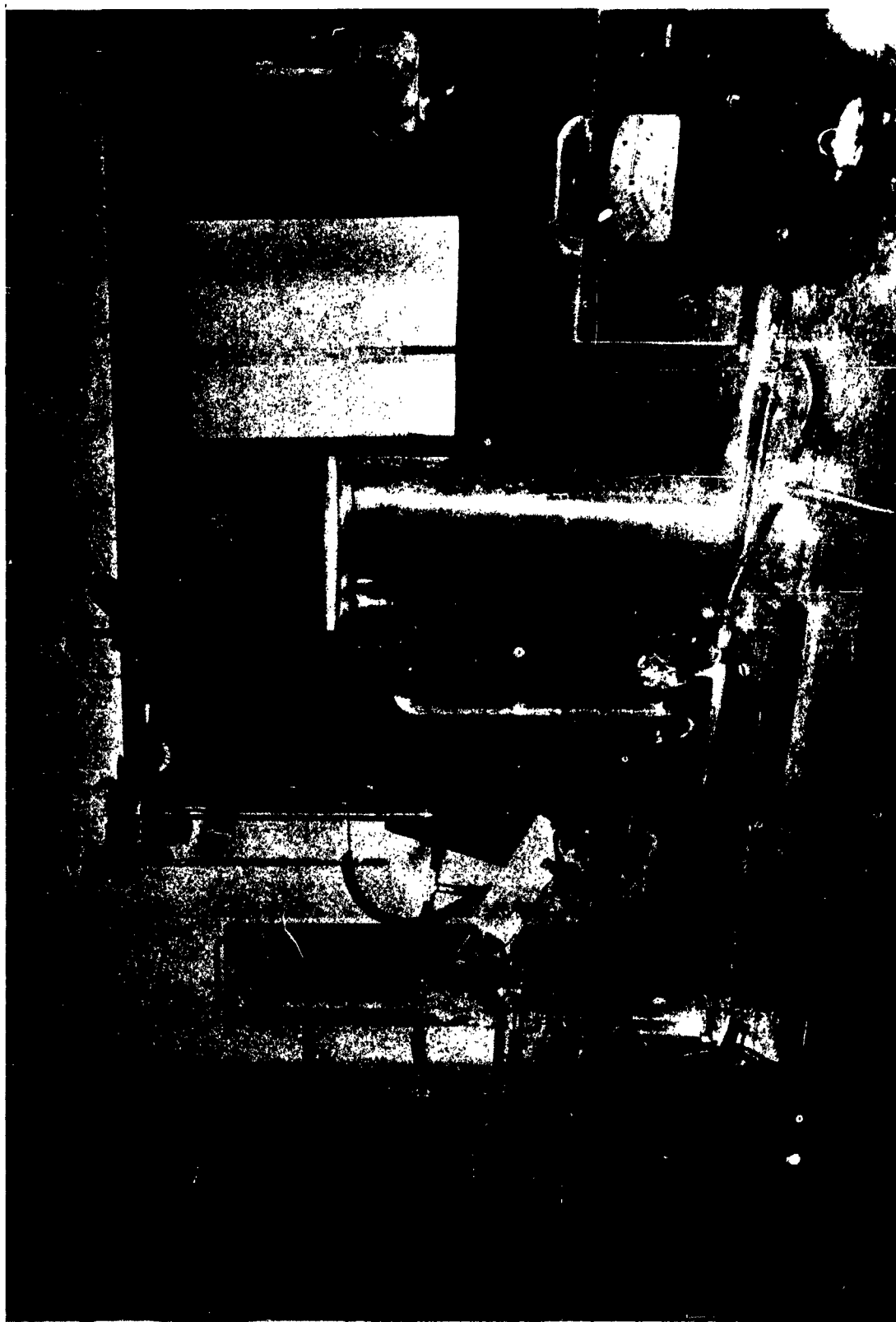
The diffusion flow mechanism was described earlier in Section II of the present report. Comparison of the porous emitter with a bundle of capillaries, as indicated therein, cannot be completely correct because the shape of the pores is variable; furthermore, the pores are interconnected. Recently E. E. Petersen (Ref. 66) and A. S. Michaels (Ref. 67) computed the diffusion through a porous body with the help of a model. The mean capillary diameter and the effective capillary length depend upon the powder size, the powder shape, the plate density, and the plate dimensions. In addition, consolidation of the powder may affect the flow rate, particularly when large powder areas are welded together. It should be noted that the consolidation effect may be negligible for spherical grains because the contact areas, in case of no deformation, are a minimum.

The experimental apparatus being used to measure the diffusion flow rate through a porous plate is shown in Figures IV-1 and IV-2. From right to left can be seen the pressure deflection meter, a gas container with fixed volume, and a needle valve connected to the porous plate for flow control. On the other side of the porous plate, the container is attached to a vacuum pumping system. McLeod pressure gauges are located on both sides of the porous plate.

As indicated earlier in Section II, flow rates in the molecular flow range and surface flow range appear to be of most interest. An estimate of the fuel evaporation rate (for 0.3% surface coverage of the exchange surface) for cesium, rubidium, and potassium can be made using the extrapolated lifetimes given by Knauer (l.c.), and also for rubidium by Hughes (l.c.). Extrapolation of Knauer's data for cesium gives an evaporation rate of 10 amps/cm² for singly charged particles at 2000°K. The data of Knauer were taken at temperatures in the range of 1400°K, therefore this extrapolation may be too optimistic. If we assume a maximum current density of 1 amp/cm², we are still far above the current densities published to date for charge exchange systems. The fuel flow through the porous plate at this high flow rate is in the molecular flow range, if the effective pore length and if the degree of consolidation are moderate. As indicated in Section II, in the molecular flow range the flow rate per unit area decreases with r , but on the other hand the fuel vapor upper pressure limit increases with $1/r$.

For a given vapor pressure, the flow rate decreases as the plate thickness L is increased, therefore for increased L , larger pressures have to be applied and the flow range may change from molecular to slip flow. The flow rate measurements, described below, were made





Diffusion Flow Measuring Apparatus

Figure IV-2

over a wide range of pressure to verify the flow regime. In the apparatus, the flow rate is measured by the change of gas pressure dp in the gas container, as given by the oil level difference in the U-manometer.

Because of its low mass, helium was used initially in the experiments, and also in some cases argon. In the molecular flow range the flow rate is a function of $1/M^2$, where M is the atomic or molecular weight, and of $1/T^2$, when the temperature of the diffusion plate is independent of the gas temperature.

The porous plates tested have been described in Section III. Before starting the flow rate measurements, statistical information was developed on the F-2 porous plate including the mean pore diameter and the isotropy of the pore distribution in three directions. Figures IV-3 and IV-4 show cross-sections of the F-2 plate parallel and perpendicular to the surface; Figure IV-5 is a cross-section of the more dense P-1 porous plate. The number of holes of equal length (± 0.25 micron) were counted out in the range from 0.5 to 20 microns in 0.5 micron steps (TABLE IV-A). In each photograph, right-angle directions were counted independently. The result is shown in Figure IV-6. Of interest is the small deviation in the single counts, so that isotropic distribution of the holes can be assumed in the F material. Only the deviations of the 0.5 micron holes are greater. The differences may be due to the tolerance in the diameter. The number of counts per diameter is a maximum for the 0.5 micron holes and decreases at greater diameters.

The measured mean pore diameter resulting from this statistical study when weighted with the statistical errors gives a value of about 5 microns as shown in TABLE IV-B. The total length of the holes to the total length of the traverses gives the percentage of porous volume. The statistical value of volume, within the statistical error, agrees with the plate density value determined by weight tests.

Computations also have been made on a model of spherical grains of equal size, for three different kinds of package, to find out the pore diameters and the effective pore lengths. The least dense package has a porous volume of 48%, the middle density 38%, and the most dense 26%. The effective length of path or the effective length of capillary also depends on the kind of package and is equal to the plate thickness at 52% density, is increased 1.23 L (with L as plate thickness) for the medium density, and is increased to 1.3 L for the most dense package. The mean capillary cross sections are $2.95 r^2$ for 52% density, $2.1 r^2$ for 62%, and $1.2 r^2$ for 74% density. Figure IV-7 gives for this model the number of capillaries per cm^2 , as a function of the mean pore radius. Figure IV-8 shows the relationship between the mean pore radius and the grain diameter for the three packages. Figure IV-9 shows the flow rate in $amps/cm^2$ for the three models dependent on the mean capillary radius "r" with Cs as fuel. Figure IV-10 gives

TABLE IV-A. PORE SIZE COUNT

FLAT						SECTION					
Microns	#1	#2	#1	#2	Σ n	Microns	#1	#2	#1	#2	Σ
x	+	o	o	Δ	*	x	+	o	o	Δ	*
0.5	50	134	83	150	417	10.5	3	2	2	1	8
1.0	65	81	69	54	269	11.0	2	2	2	2	8
1.5	54	65	59	60	238	11.5		1			1
2.0	56	55	44	41	196	12.0	1		3		4
2.5	18	35	19	46	118	12.5	2				2
3.0	28	35	28	21	112	13.0					
3.5	19	19	18	12	68	13.5					
4.0	21	15	17	11	64	14.0			2		2
4.5	9	9	8	12	38	14.5			1		1
5.0	19	8	8	13	48	15.0	1				1
5.5	7	7	2	7	23	15.5					
6.0	11	14	8	2	35	16.0			1		1
6.5	6	5	4	4	19	16.5			1	2	3
7.0	7	2	3	5	17	17.0	1				1
7.5	3	5	2	6	16	17.5					
8.0	7	1	1	6	15	18.0	1				1
8.5	1	6	-	2	9	18.5					
9.0	3	6	1	-	10	19.0		1			1
9.5	1	1	1	3	6	19.5					
10.0	6	3	1	1	11	20.0		1		1	2
POROUS TUNGSTEN PLATE, F2 .030in. THICK Original data taken from measurements on 1000 x, microphotographs Numbers in body of table (n) are counts of holes "x" microns long						20.5					
						21.0	1				1
						21.5					
						22.0	1				1
						22.5					
						23.0					
						404	513	388	462	1767	
						110	125	95	130		
ORIGINAL READINGS						LENGTH EACH LINE - MICRONS					
(Traverses #1 & #2 taken at right angles to each other on the same photograph)											

TABLE IV-B. MEAN PORE DIAMETER

FLAT						SECTION					
Microns	#1	#2	#1	#2	Σ	Microns	#1	#2	#1	#2	Σ
x	+	◇	o	Δ	*	x	+	◇	o	Δ	*
0.5	3.535	5.788	4.555	6.123	10.210	1.05	18.186	14.847	14.847	10.500	29.694
1.0	8.062	9.000	8.307	7.348	16.401	1.10	15.534	15.534	15.534	15.534	31.108
1.5	11.022	12.093	11.521	11.619	23.140	1.15		11.500			11.500
2.0	14.966	19.832	13.266	12.806	28.000	1.20	12.000		20.784		29.000
2.5	10.607	19.790	10.898	16.955	27.157	1.25	17.675				17.675
3.0	15.873	17.748	15.873	13.749	31.749	1.30					
3.5	15.257	15.256	14.851	12.124	28.861	1.35					
4.0	18.332	15.492	16.492	13.268	32.000	1.40			19.796		19.796
4.5	13.500	13.500	12.726	15.588	27.738	1.45			14.500		14.500
5.0	21.735	14.140	14.140	18.030	34.640	1.50	15.000				15.000
5.5	14.553	14.553	7.777	14.553	26.378	1.55					
6.0	19.902	22.452	16.968	8.484	35.496	1.60			16.000		16.000
6.5	15.918	14.534	13.000	13.000	28.334	1.65			16.500	23.331	28.578
7.0	18.522	9.898	12.124	15.652	28.861	1.70	17.000				17.000
7.5	12.990	16.770	10.605	18.368	30.000	1.75					
8.0	21.168	8.000	8.000	19.592	30.984	1.80	18.000				18.000
8.5	8.500	20.816	-	12.019	25.500	1.85					
9.0	15.588	22.041	9.000	-	28.458	1.90		19.000			19.000
9.5	9.500	9.500	9.500	16.454	22.266	1.95					
10.0	24.490	17.320	10.000	10.000	33.170	20.00		20.000		20.000	28.280
POROUS TUNGSTEN PLATE, F2 .030 in. THICK 1000x PHOTO SUMMATION OF $x\sqrt{n}$ Body of table gives $x\sqrt{n}$ with n and x both taken from table IV A						20.50					
						21.00	21.000				21.000
						21.50					
						22.00	22.000				22.000
						22.50					
						23.00					
$\Sigma(\Sigma x\sqrt{n})$						450.495	369.924	337.584	326.117	883.474	
$\Sigma\sqrt{n}$						87.976	88.678	77.765	90.128	178.658	
$\Sigma(\Sigma\sqrt{n})/\Sigma\sqrt{n}$						5.121	4.171	4.212	3.607	4.945	
						STATISTICAL MEAN DIA.					

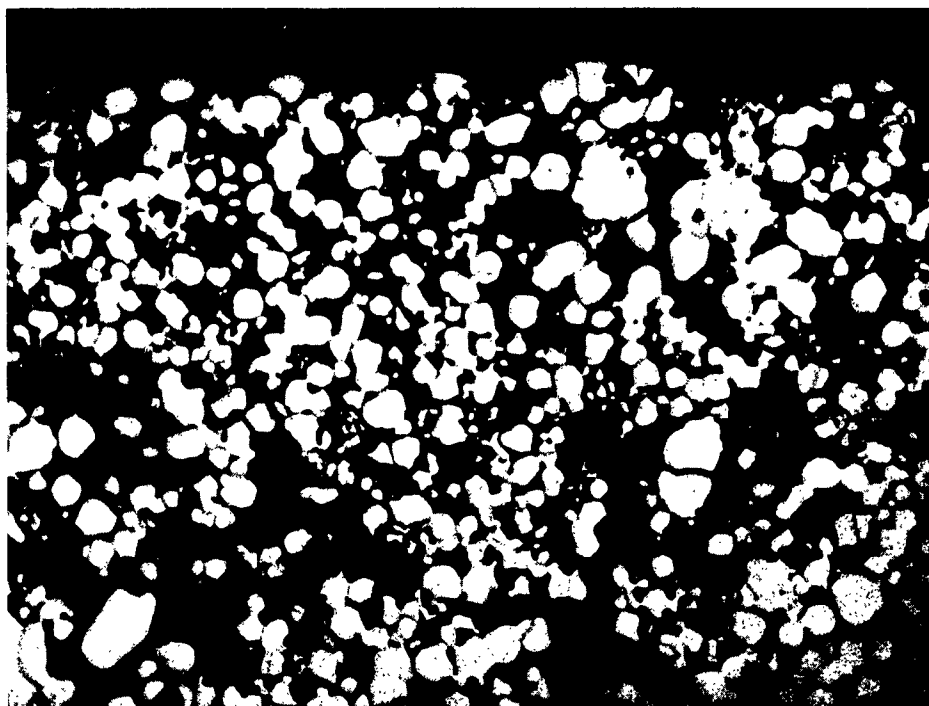
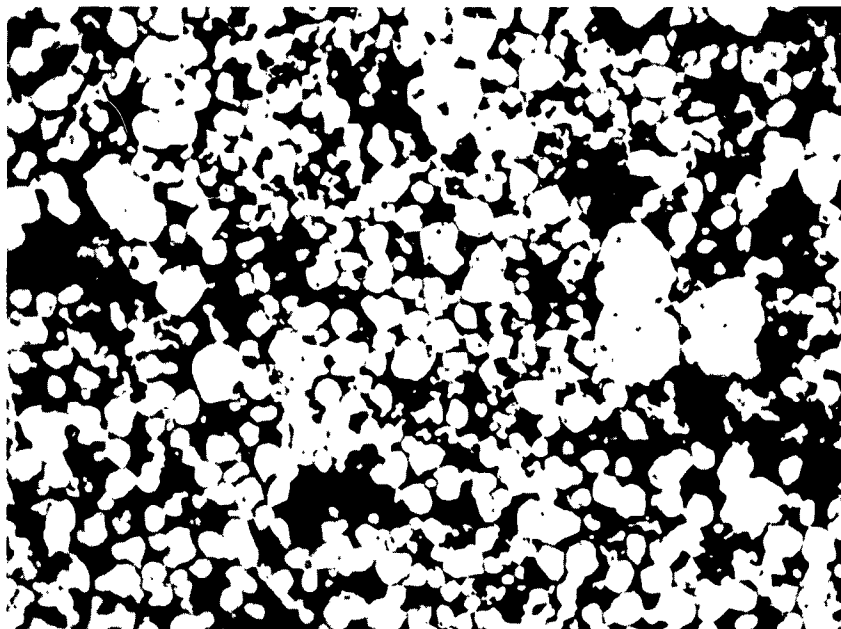
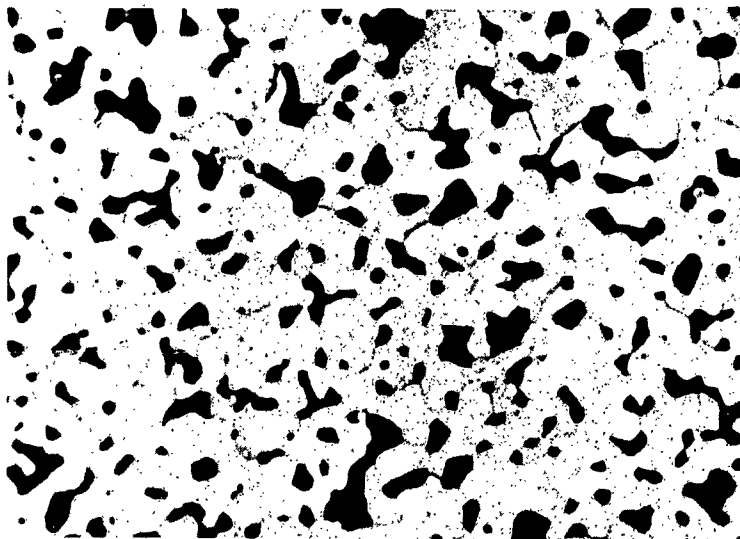


Figure IV-3. Cross-Section of F-2 Porous Plate, 1000X
Surface of Plate at Top



**Figure IV-4. Cross-Section of F-2 Porous Plate,1000X
Parallel to Plate Surface**

..
--
--
--
I
I
I
I
--
--



M-1085

Figure IV-5. Cross-Section of P-1 Porous Plate, 1000X

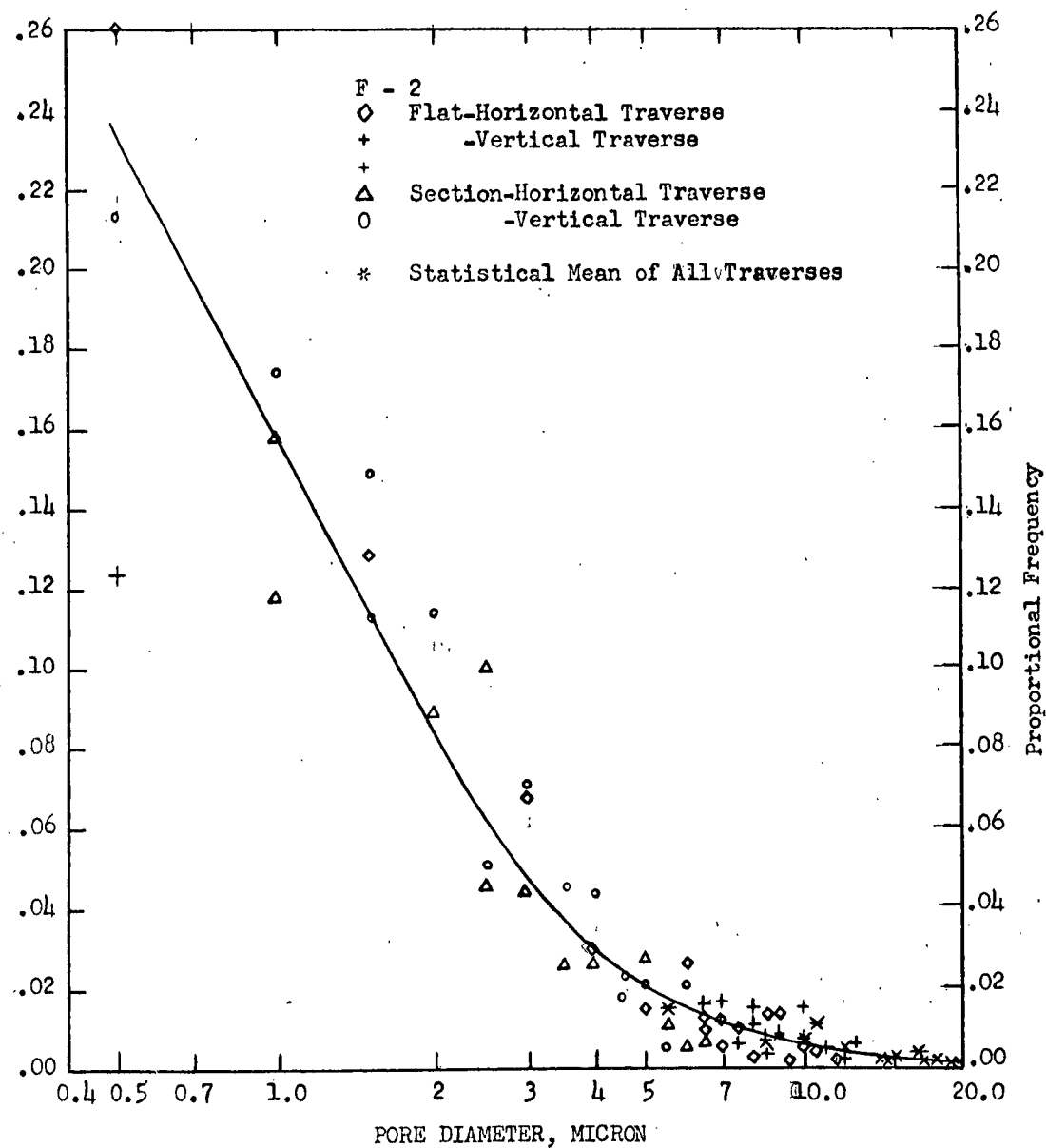


Figure IV-6

PROPORTIONAL FREQUENCY OF VOID LENGTHS

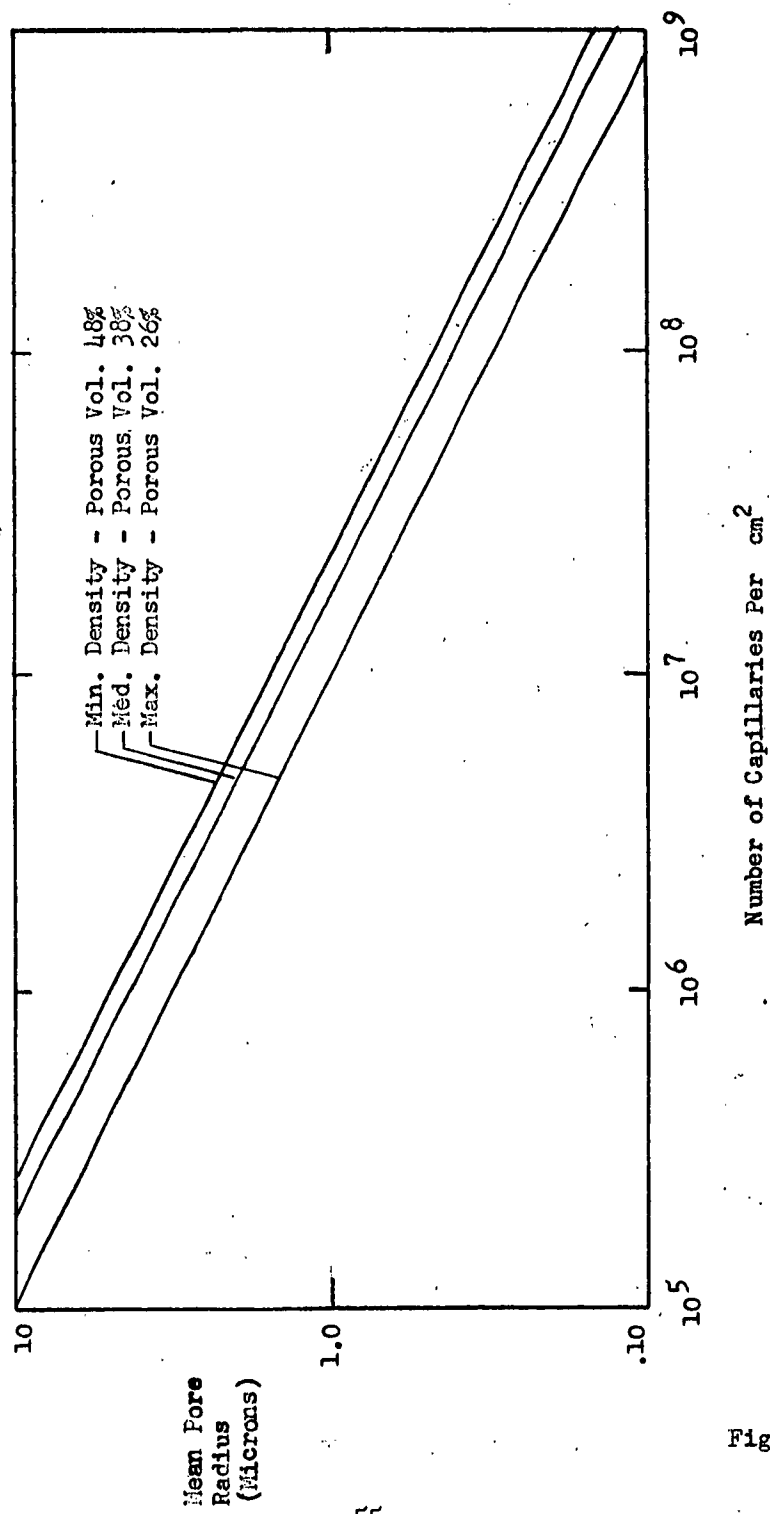


Figure IV-7

THEORETICAL POROUS PLATE MODEL, WITH UNIFORM SPHERICAL GRAINS

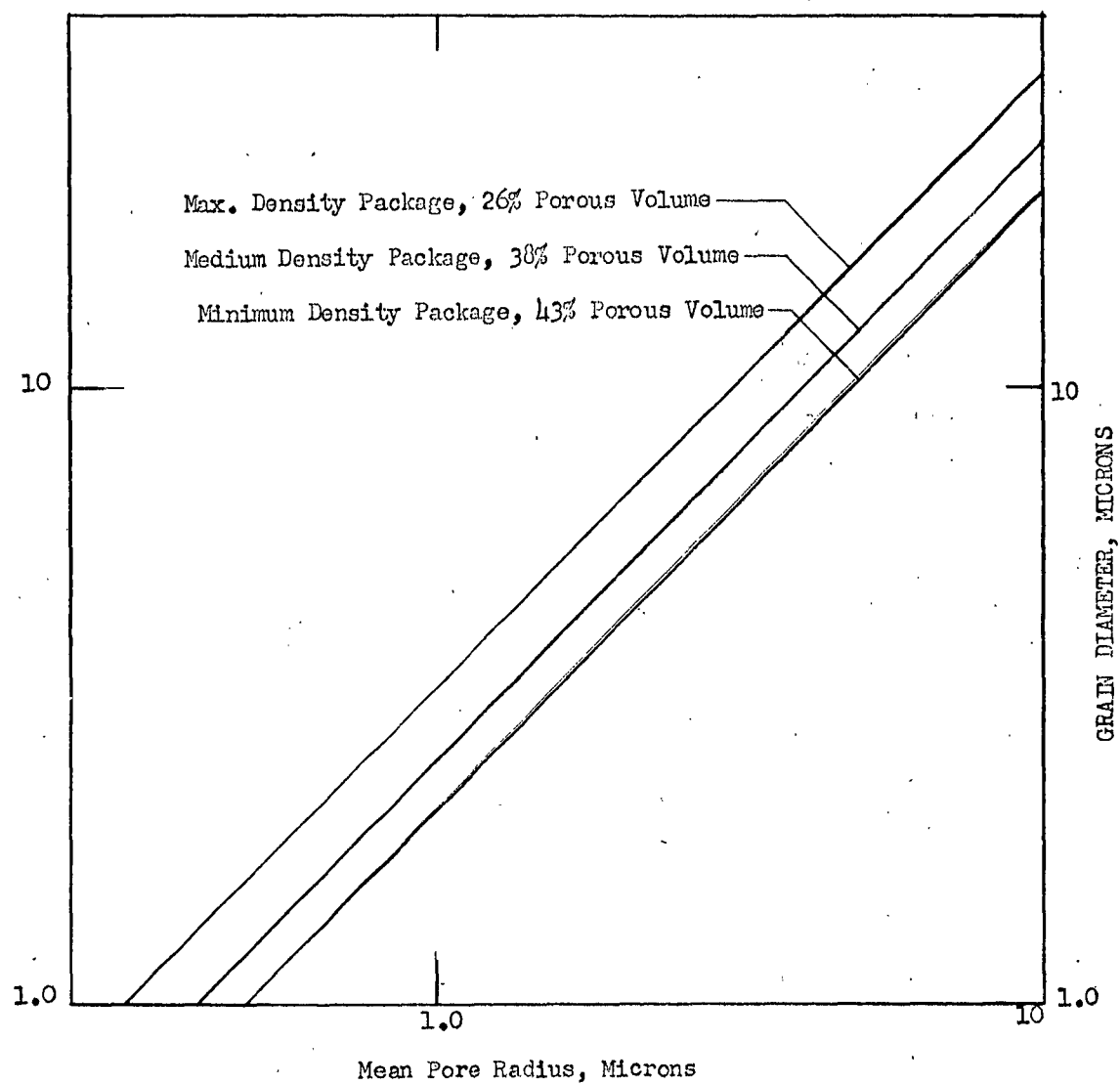


Figure IV-8

MEAN PORE RADIUS VERSUS GRAIN DIAMETER FOR
THEORETICAL MODEL WITH UNIFORM SPHERICAL GRAIN

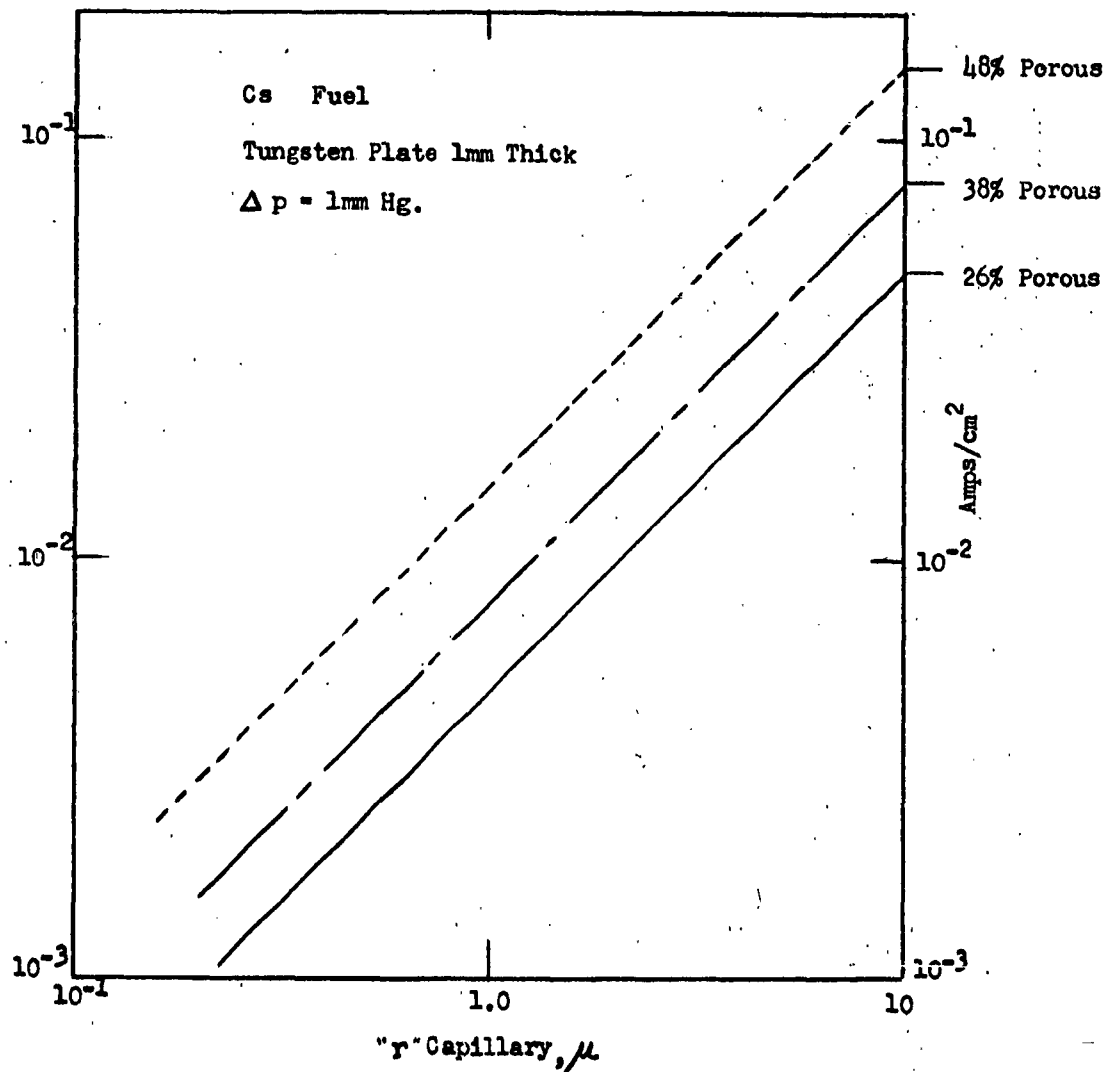


Figure IV-9

THEORETICAL FLOW IN AMPS PER cm² IN
 MODEL PLATE AS A FUNCTION OF PORE RADIUS

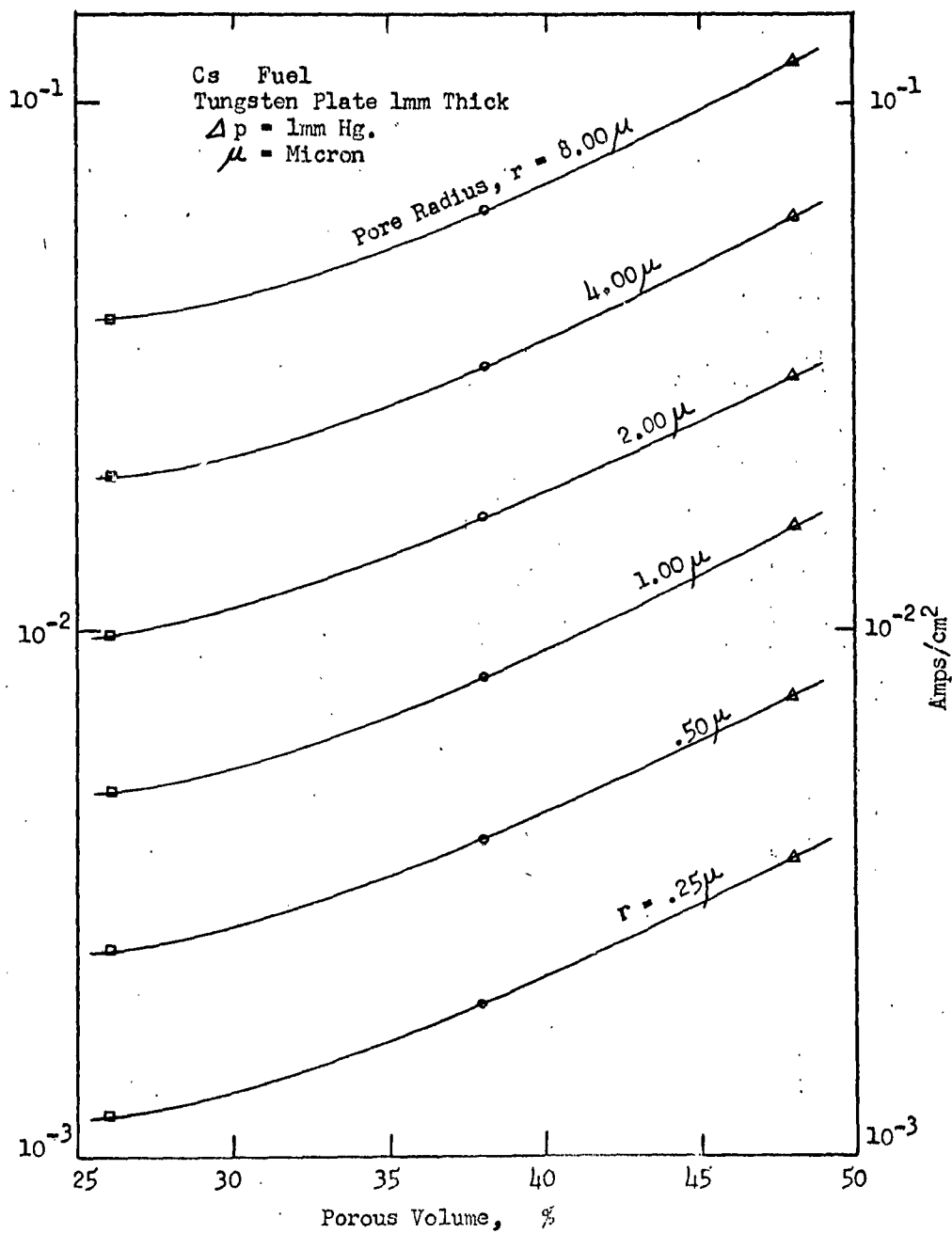


Figure IV-10

THEORETICAL FLOW IN AMPS PER cm^2 IN
 MODEL PLATE AS A FUNCTION OF POROUS VOLUME

the flow rate again in amps/cm^2 as a function of the porous volume with the mean pore radius as a parameter.

The aforesaid model was used for comparison purposes with the measured flow rates of the three porous plates.

A less complicated assumption is the use of a bundle of capillaries instead of a porous plate. Figure IV-11 gives the flow rate in amps/cm^2 for such a bundle as a function of the vapor mass, and Figure IV-12 gives the flow rate through a bundle of capillaries as function of the pore radius. Depending on the two possible kinds of package the porous volumes are 90.7% and 75.8%.

In making the flow rate measurements with the apparatus of Figure IV-1, the pressure on one side of the porous plate is adjusted with the needle valve. The flow rate is measured by dh , the change of the oil level in the U-manometer, as a function of time. TABLE IV-C gives some data for the gases used and also for xenon, which is close in weight to cesium.

TABLE IV-C. SOME GAS PROPERTIES

Gas	M (gr)	Molecular diameter (cm)	Viscosity	Sutherland Const. 20 to 100°C
Helium	4.003	$2.18(10^{-8})$	$1.8(10^{-4})$	73
Argon	39.94	$3.66(10^{-8})$	$2.11(10^{-4})$	148
Xenon	131.3	$4.88(10^{-8})$	$2.11(10^{-4})$	250

The diffusion experiments were started with Pt - screen (spinnerette), in which 1000 holes had been punched. The flow rates, TABLE IV-D, agree well with the expected flow rates after cleaning the plate by preheating.

TABLE IV-D. PLATINUM SCREEN DIFFUSION RESULTS

Maximum mean free path 20 μ
 P_{max} (argon) 1.9mm Hg P_{max} (He) 5.3mm Hg p_2 in micron range
 Clausing factor 1.27

Gas	dp (Tor)	Plate Temp. °K	dh (cm/10 Min)	V_g (cm ³ /10 Min) at 760 Tor, 0°C	Remarks
Argon	16.3	296	11.2	38.9	Before Outgassing
Argon	14.75	300	21.0	72.5	After Outgassing
Argon	1.4	1033	1.3	4.5	
Argon	1.2	1273	1.28	4.4	
Argon	1.25	296	2.27	7.8	
Helium	3.37	298.5	19.0	65.2	

CURTISS-WRIGHT CORPORATION • RESEARCH DIVISION



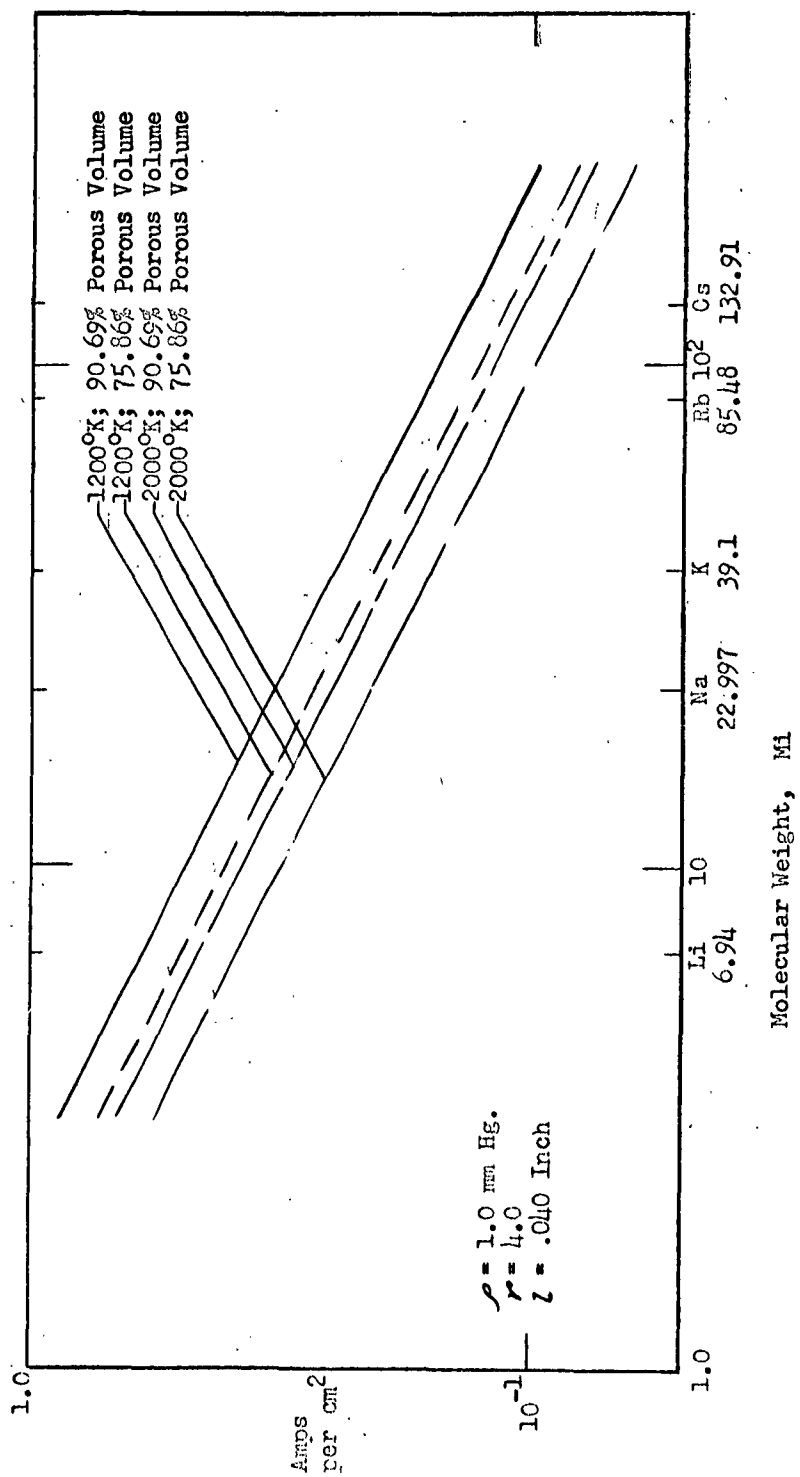


Figure IV-11

MOLECULAR FLOW RATE THROUGH A BUNDLE OF CAPILLARIES

AS A FUNCTION OF MOLECULAR WEIGHT

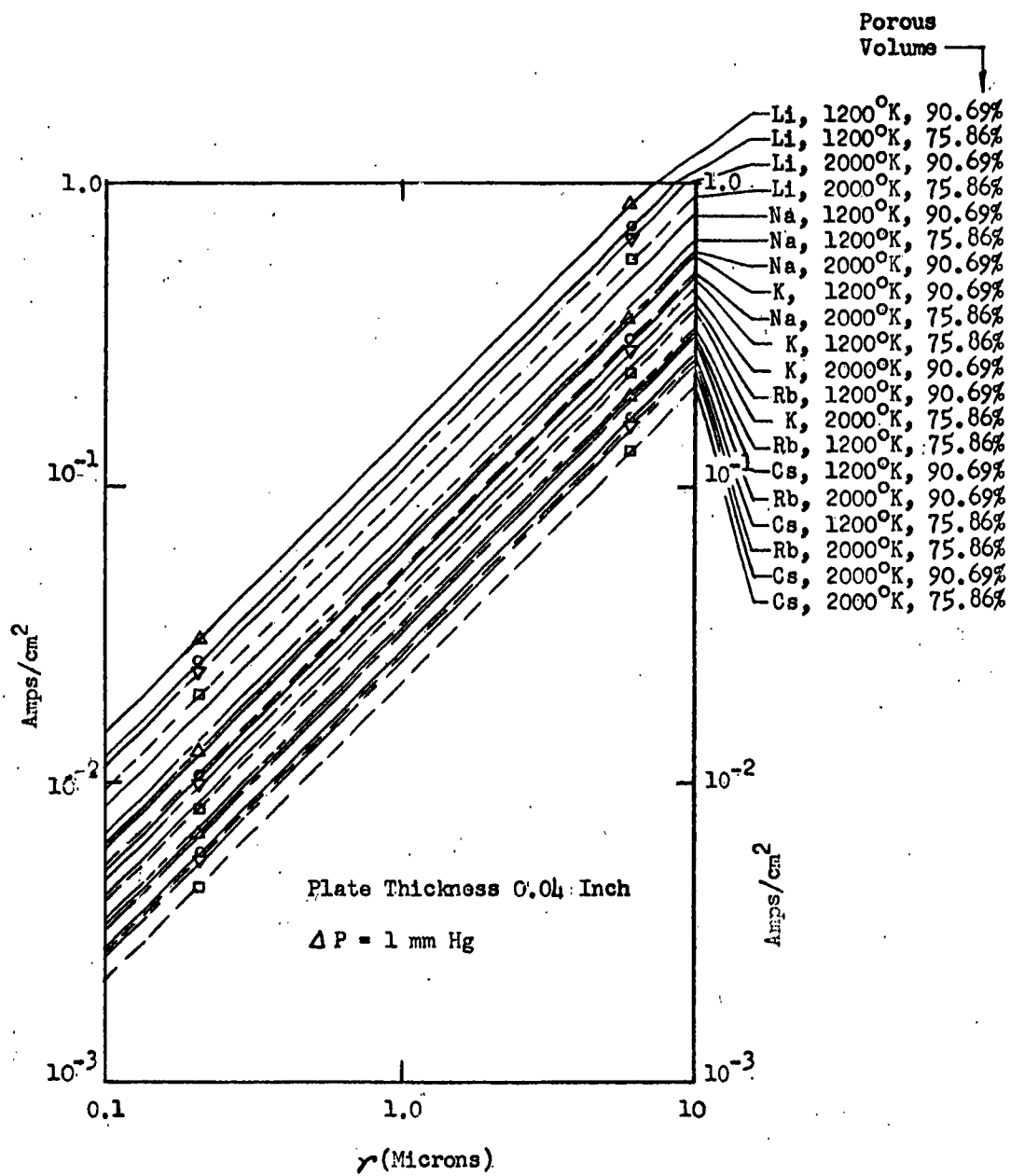


Figure IV-12

MOLECULAR FLOW RATE THROUGH A BUNDLE OF CAPILLARIES

AS A FUNCTION OF PORE RADIUS

As TABLE IV-D shows, the flow rate before outgassing was about half of the measured value after the heat treatment. Since the capillary length is not much greater than its diameter, a correction factor (Clausing factor) must be applied, as given in TABLE IV-E.

TABLE IV-E. CLAUSING FACTOR

$4L/r = \infty$	$f = 1.00$
20	1.35
16	1.44
12	1.58
8	1.86
4	2.60

Figures IV-13 and IV-14 show that the $1/T^{1/2}$ and the $1/M^{1/2}$ laws are well obeyed. In Figure IV-13 the flow rate is shown versus the vapor pressure.

Measurements with the molybdenum screen do not agree as well with theory as the previous platinum screen. Data is given in TABLE IV-F.

TABLE IV-F. MOLYBDENUM SCREEN FLOW TESTS

1280 holes per cm ²			Surface area, 3.01 cm ²		
Total number of holes, 3860			Hole length, 25 u		
Hole diameter, 67 u to 72 u			P _{max} (He)1.9mm Hg.		
<u>Gas</u>	<u>dp (Tor)</u>	<u>Plate Temp. °K</u>	<u>dh (cm/10 Min)</u>	<u>V_g(cm³/10 Min) at 760 Tor, 0°C</u>	<u>Remarks</u>
He	0.76	292	0.89	13.68	
He	2.00	292.5	3.79	58.16	
He	1.85	296.5	1.15	17.41	
He	1.20	292	1.73	26.59	
He	1.00	297	1.04	16.0	2 plates on top of each other, 0° angle.
He	0.92	293	0.97	14.85	2 plates on top of each other, 5° to 10° turned.
He	0.90	293	1.21	18.4	2 plates on top of each other, 15° turned.
He	1.25	293	1.575	24.1	2 plates on top of each other, 30° turned.

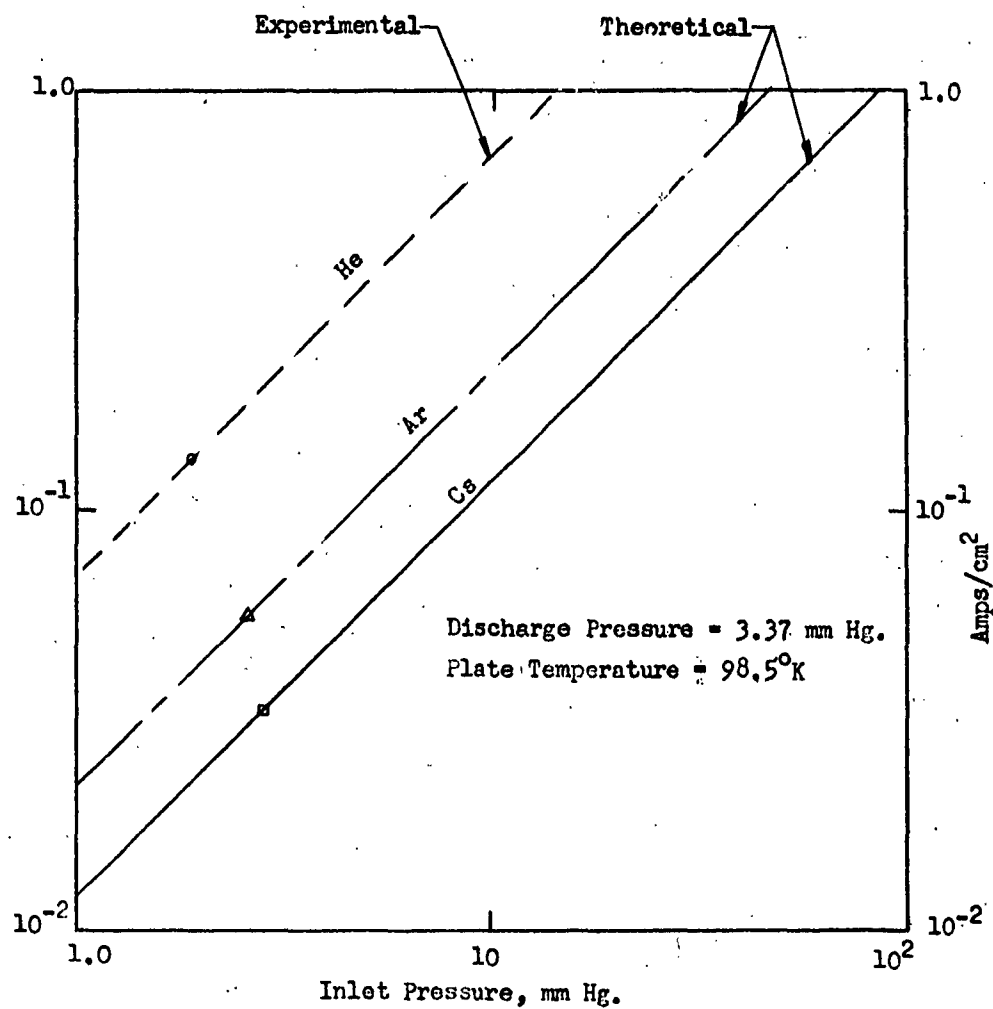


Figure IV-13

EXPERIMENTAL AND THEORETICAL DIFFUSION FLOW
FOR PLATINUM SCREEN

P_{max} (Argon) = 1.9 mm Hg.
 P_{max} (He) = 5.35 mm Hg.

— Argon
 - - - Helium
 - - - He: Theoretical value with clogging correction

} 1 mm Hg.

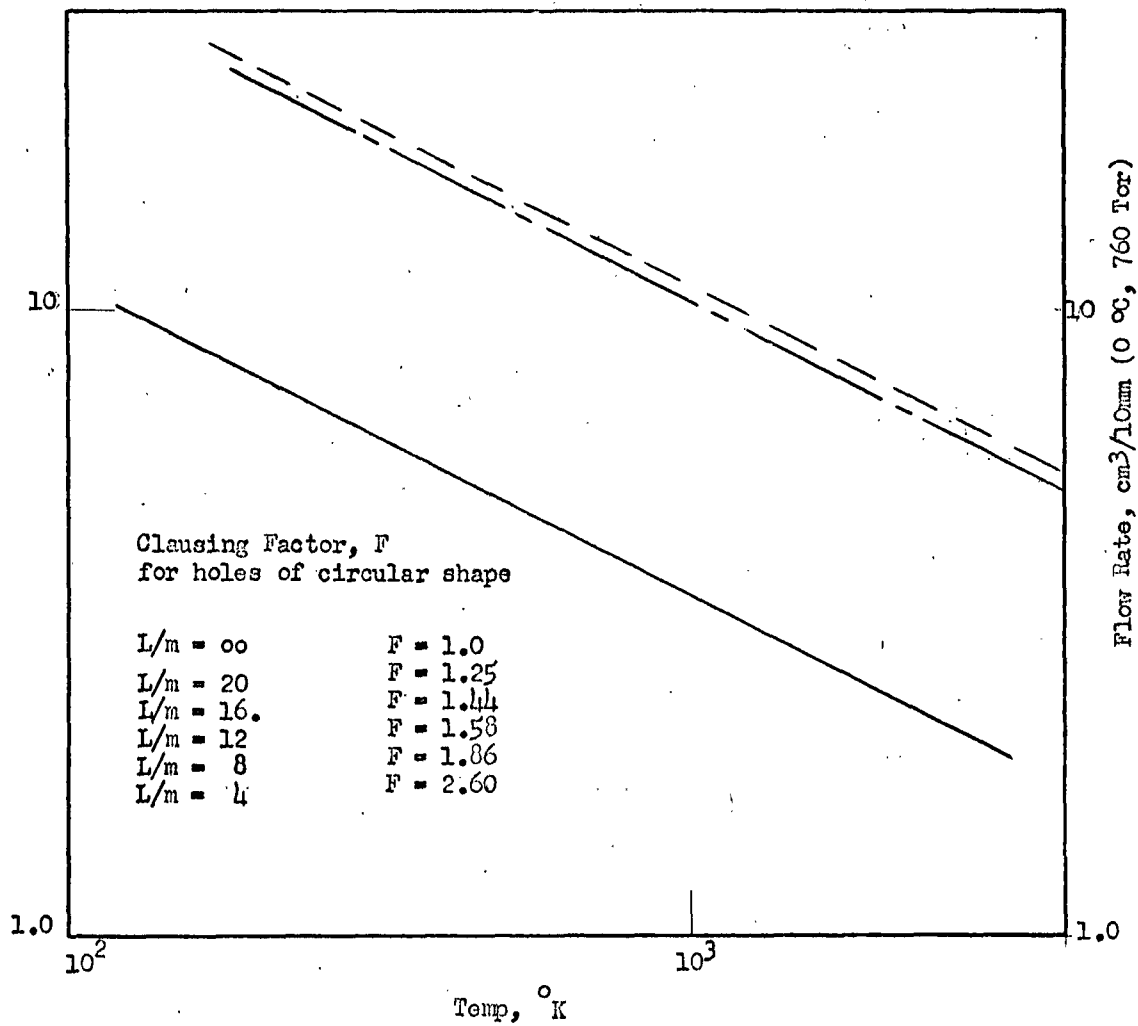


Figure IV-14

PLATINUM SCREEN DIFFUSION FLOW AS A
 FUNCTION OF SCREEN TEMPERATURE

The measured flow rate per capillary is about one order of magnitude less than the computed (Figure IV-15). The main reason may have been due to the difficulty of heating this plate in the vacuum system. The investigations will be repeated shortly.

TABLE IV-G gives values of the flow rate measurements with the P-2 0.040 in. porous plate, 17% porous volume.

TABLE IV-G. FLOW TEST OF P-2 TUNGSTEN PLATE

Porous Volume: 17% Surface Area 1.138 cm² (later investigation showed that the surface partially has been covered with Ni - perhaps up to 90%)
 Plate Thickness: 0.040 in.

Gas	dp (Tor)	Plate Temp. °K	dh (cm/min)	Vg (cm ³ /min)
He	16	308	0.252	0.865
He	14	1305	0.231	0.795
He	27	297	0.62	2.14
He	33	1393	0.9	3.09
He	30.5	795	0.495	1.7
He	27.8	489	0.456	1.595
He	28.5	296	0.48	1.66
He	13	296	0.21	0.722
He	12	873	0.127	0.436
He	10	1233	0.127	0.436
He	14.1	292	0.28	0.99
He	36.3	292	0.98	3.46
He	39.5	1183	0.805	2.84
He	36	1183	0.745	2.64

After the flow rates had been measured, a microscopic investigation of the plate surfaces showed one side as much as 90% covered with nickel material. The flow did not increase in proportion to pressure, as expected, but changed to some extent independent of pressure. Bypassing of part of the gas between the porous plate and the molybdenum holder tube is a tentative explanation. Therefore the expected temperature slope is not well confirmed; for a mean flow rate the computed mean pore radius is 0.12 micron (Figure IV-16). The computed slope for cesium is included. The factor 1.35 for the effective capillary length is linearly extrapolated from the three-dimensional model with the spherical grains. Measurements on this plate will be repeated, without bypass flow and surface blockage.

TABLE IV-H gives the flow rate data for the F-1 porous plate; Figures IV-17 and IV-18 show the corresponding fuel flow rates depending on the gas pressure. In contrast to the statistical investigation, the mean hole diameter appears to be far smaller, i.e., 0.51 u. This



----- Orifice
 ----- Capillary with $l=2.5 \times 10^{-4}$ cm

$$L^* = 22.8 \times 10^2 \times F$$

$$L = 22.8 \times 10^2 \times \frac{F}{1 + \frac{3}{10} \frac{U}{F}}$$

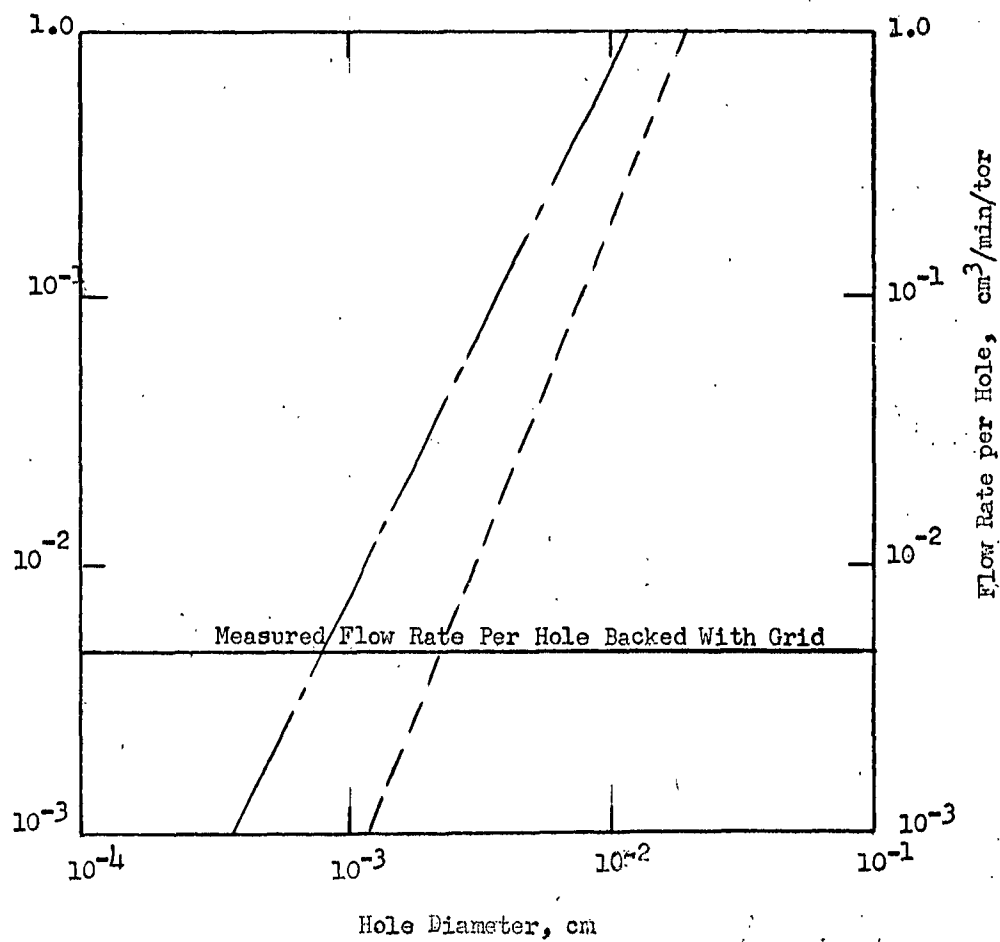


Figure IV-15

FLOW RATE FOR MOLYBDENUM SCREEN

1.138 cm² (no blockage) Surface

17% Porous Volume

$r = .12\mu$

$T = 308^\circ\text{K}$

$P = 16.0$ tor

$l = 1.35 \times \text{plate thickness}$

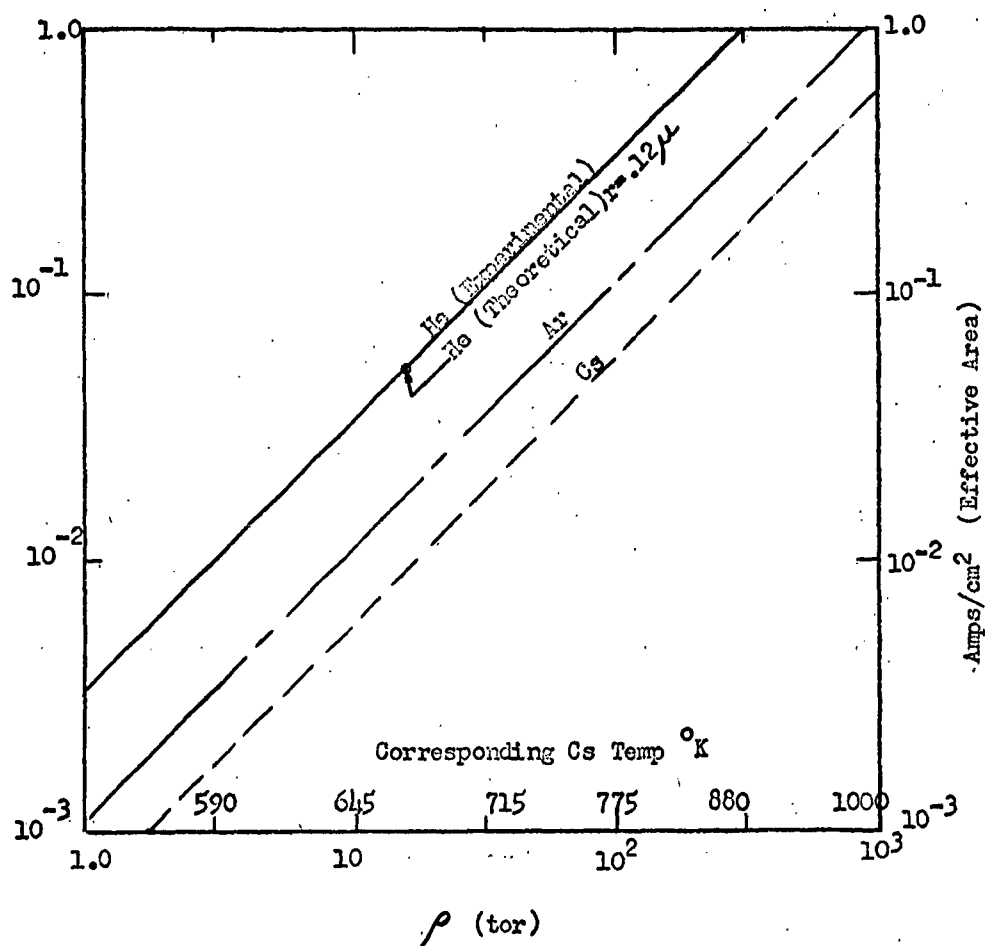


Figure IV-16

EXPERIMENTAL AND THEORETICAL
FLOW DATA FOR P-2 TUNGSTEN PLATE

43% Porous Volume
Surface Area, 0.797 cm²

a = Aging Effect

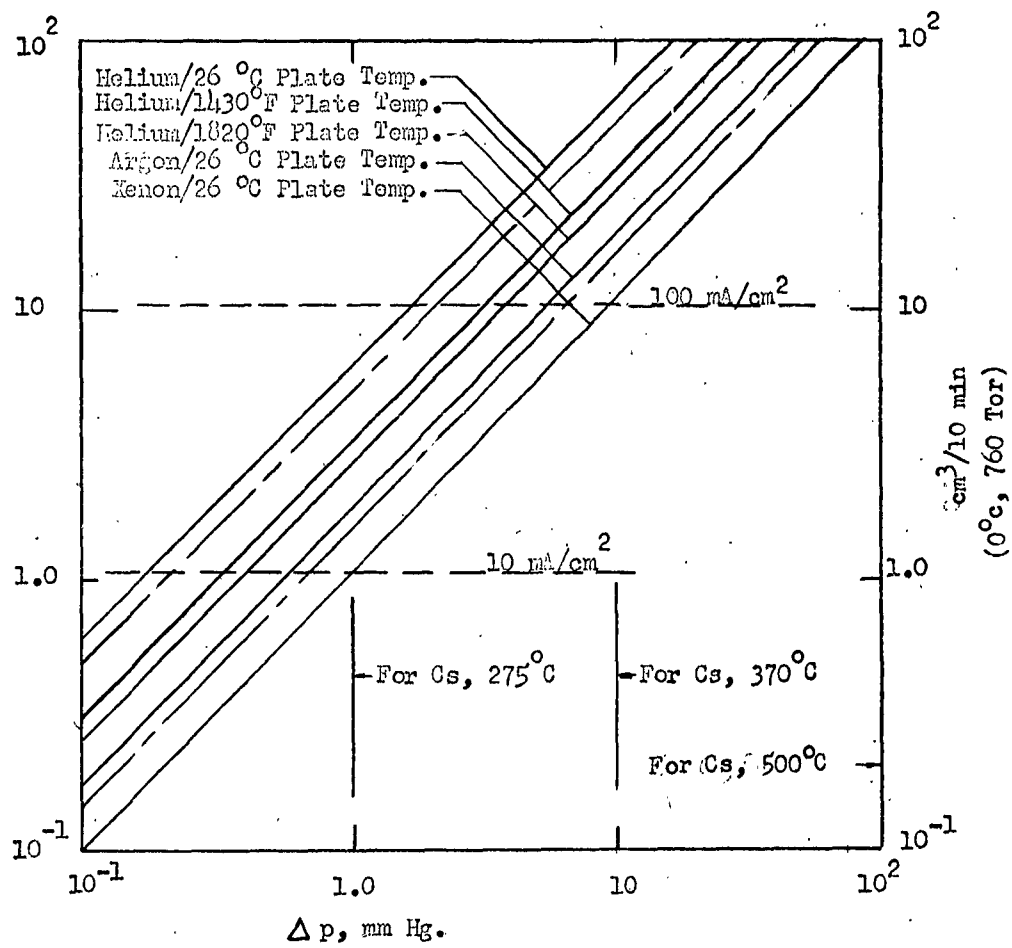


Figure IV-17

FLOW DATA FOR F-1 POROUS TUNGSTEN

PLATE SHOWING AGING EFFECT

$.798 \text{ cm}^2$ Surface
 42.2% Porous Volume
 $T = 293^\circ \text{K}$
 $p = 19.4 \text{ tor}$
 $l = 1.23 \times \text{Plate Thickness}$
 $r = .509 \mu$

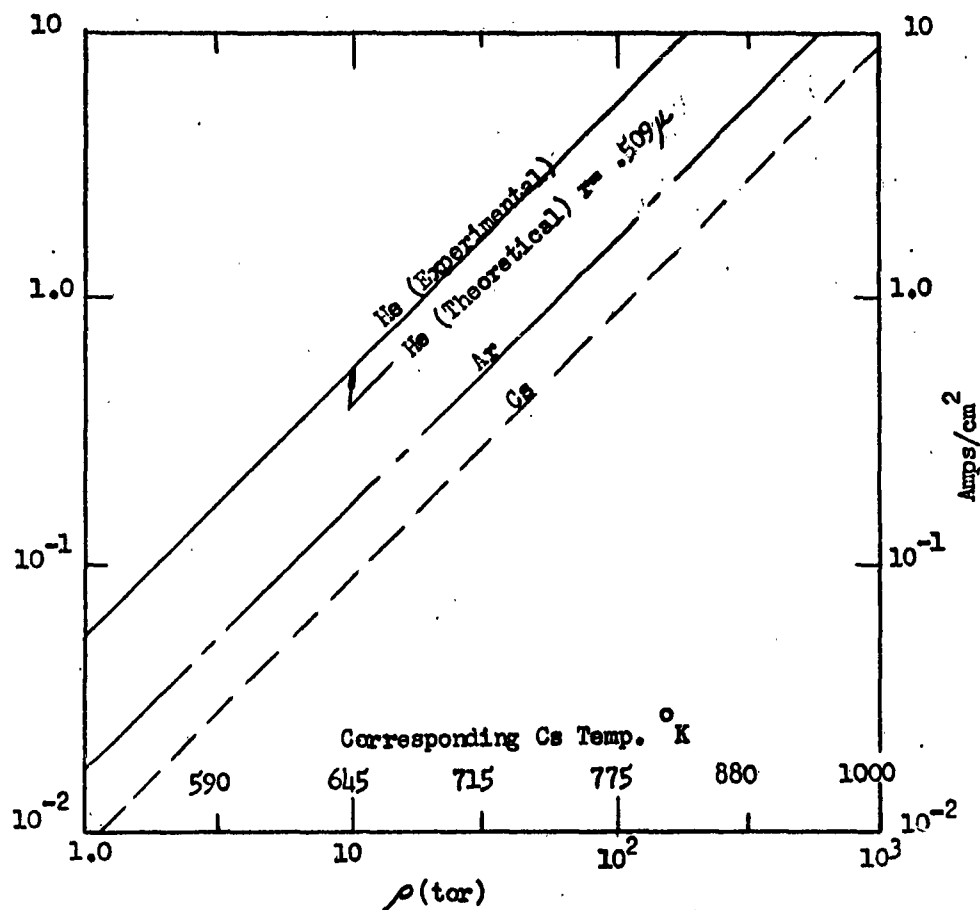


Figure IV-18

EXPERIMENTAL AND THEORETICAL FLOW DATA
 FOR F-1 POROUS PLATE

plate showed considerable shrinkage after heat treatment. Because the plate had been brazed to a molybdenum tube, no bypass leakage was observed. Figure IV-19 shows this plate before and after the heat treatment. The $1/T^{1/2}$ slope is well established.

TABLE IV-H. FLOW DATA FOR F-1 POROUS PLATE

F-1 --- 0.050 in. Porous Tungsten Plate --- Surface Area 0.798 cm^2
Porous Volume 42.2%

Measurements after outgassing at 990°C

Gas	p (Tor)	Plate Temp. $^\circ\text{K}$	dh (cm/min)	V_g (cm^3/min)	Remarks
He	19.9	293	3.41	11.98	
He	13.45	1028	1.26	4.31	
He	12.6	1263	1.18	4.05	
He	19.0	1038	1.83	6.44	
He	5.0	1268	0.4	1.375	
He	10.5	299	1.51	5.18	After heat treatment at 1443 K for 215 minutes.
Argon	5.1	300	0.224	0.765	

The flow rate through the C-1 tungsten plate versus plate temperature is also shown in Figure IV-19. The slopes do not follow closely the $1/T^{1/2}$ slope. The arrows indicate the temperature cycle. With decreasing temperature the flow rate is increased, possibly due to bypassing. Data are given in TABLE IV-I and Figure IV-20. Further tests are required.

Since the completion of the diffusion experiments described herein, a new brazing technique for the porous plates has been developed and it is planned to repeat all these investigations. Data presented thus far shall be considered as preliminary.

In connection with the development of the L-cathode, Rutledge and Rittner (Ref. 68) measured Ba-flow rates through porous plates in the range between 11% and 29% porous volume. Figure IV-21 shows their values of transmission coefficient versus porous volume. Our test results will be compared with the Rutledge and Rittner data after the diffusion experiments are repeated.

Transformation to current of the flow rate in number of particles per time unit is given by: $(K)(e) = J$ amps, with $e = (1.602)(10^{-19})$ coulomb. Therefore 1 amp is equal to $(6.25)(10^{18})$ singly-charged particles, assuming 100% efficiency.

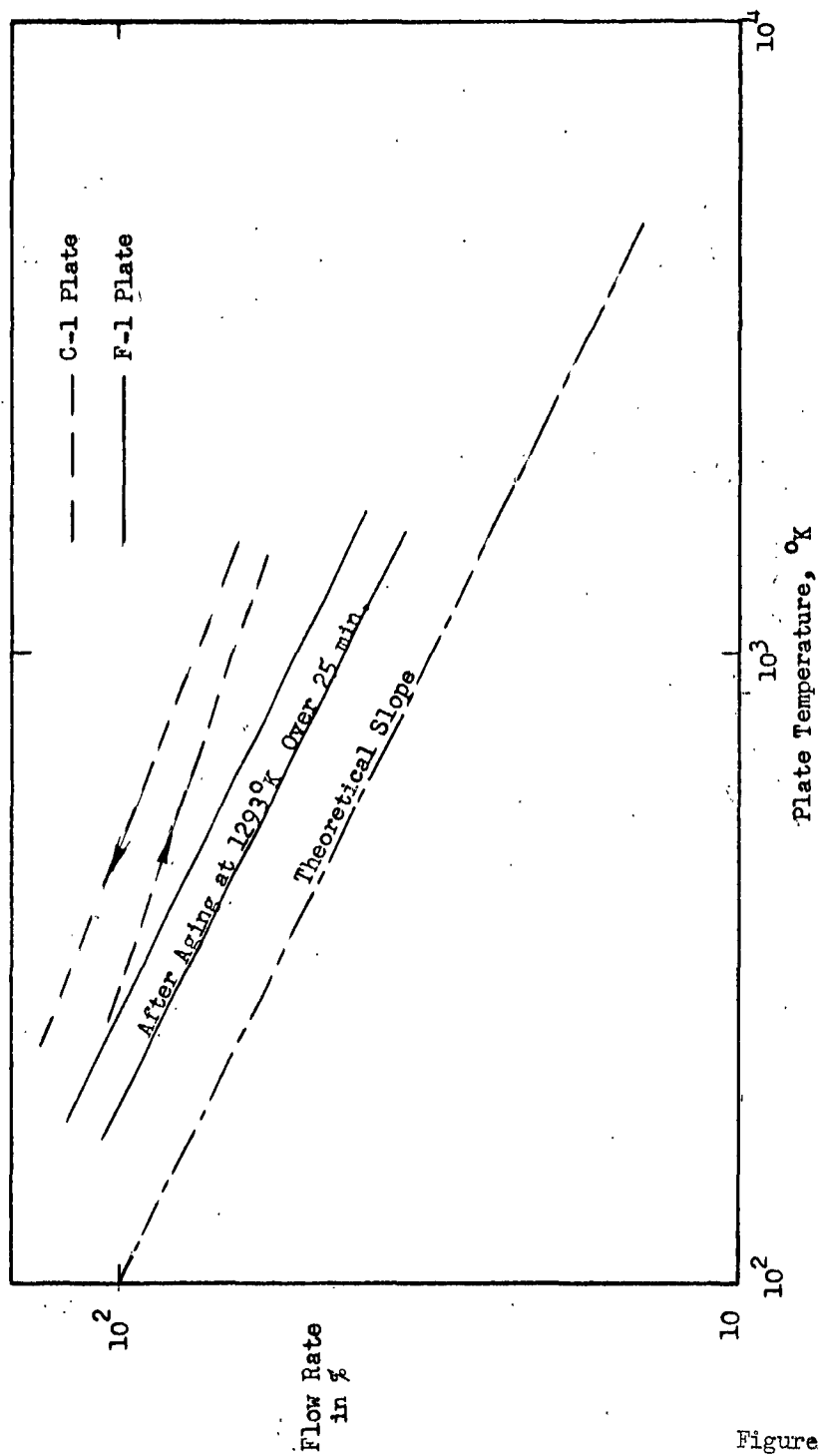
TABLE IV-1. FLOW DATA FOR C-1 POROUS TUNGSTEN PLATE

Porous Volume: 48.2%

Surface Area 1.259 cm²

Plate Thickness: 2.645mm

<u>Gas</u>	<u>dp (Tor)</u>	<u>Plate Temp. °K</u>	<u>dh (cm/min)</u>	<u>Vg (cm³/min)</u>
He	4.4	299	0.81	2.8
He	33.0	299	6.59	22.6
He	3.0	299	0.5825	2.0
He	4.1	300	0.795	2.65
He	12.8	300	2.56	8.8
He	8.0	300	1.365	4.85
He	3.7	377	0.558	1.92
He	5.7	375	1.045	3.58
He	6.4	598	0.938	3.2
He	6.4	783	0.84	2.9
He	4.6	297	0.915	3.15
He	4.5	953	0.54	1.87
He	3.8	1158	0.442	1.52
He	3.6	297	0.28	0.96
He	5.65	1280	0.67	2.335
He	2.1	299	0.491	1.685



HELIUM FLOW RATE THROUGH POROUS TUNGSTEN
AS A FUNCTION OF PLATE TEMPERATURE (Molecular Flow)

Figure IV-19

1.259 cm² Surface
48.2% Porous Volume

$r = .415\mu$
 $T = 299^\circ\text{K}$
 $P = 4.4 \text{ tor}$
 $l = \text{Plate Thickness}$

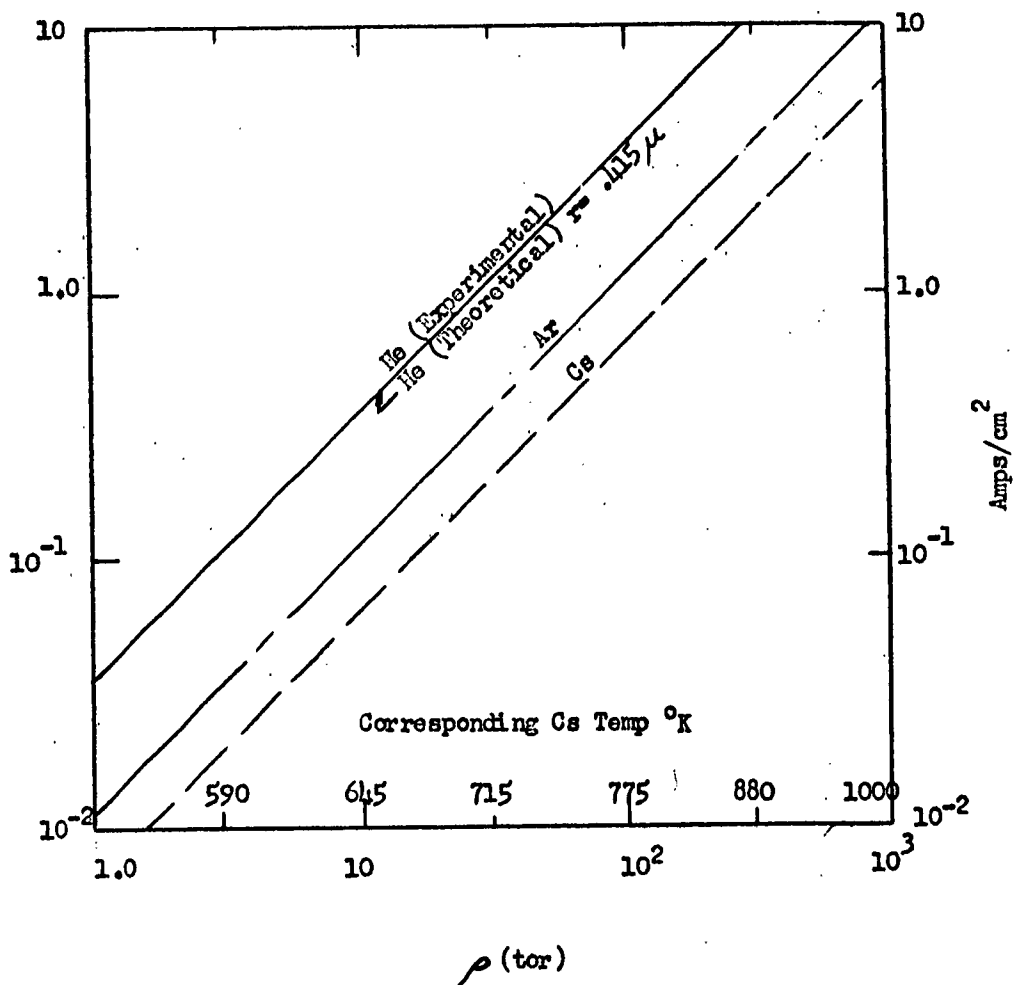


Figure IV-20

EXPERIMENTAL AND THEORETICAL
FLOW DATA FOR C-1 POROUS PLATE

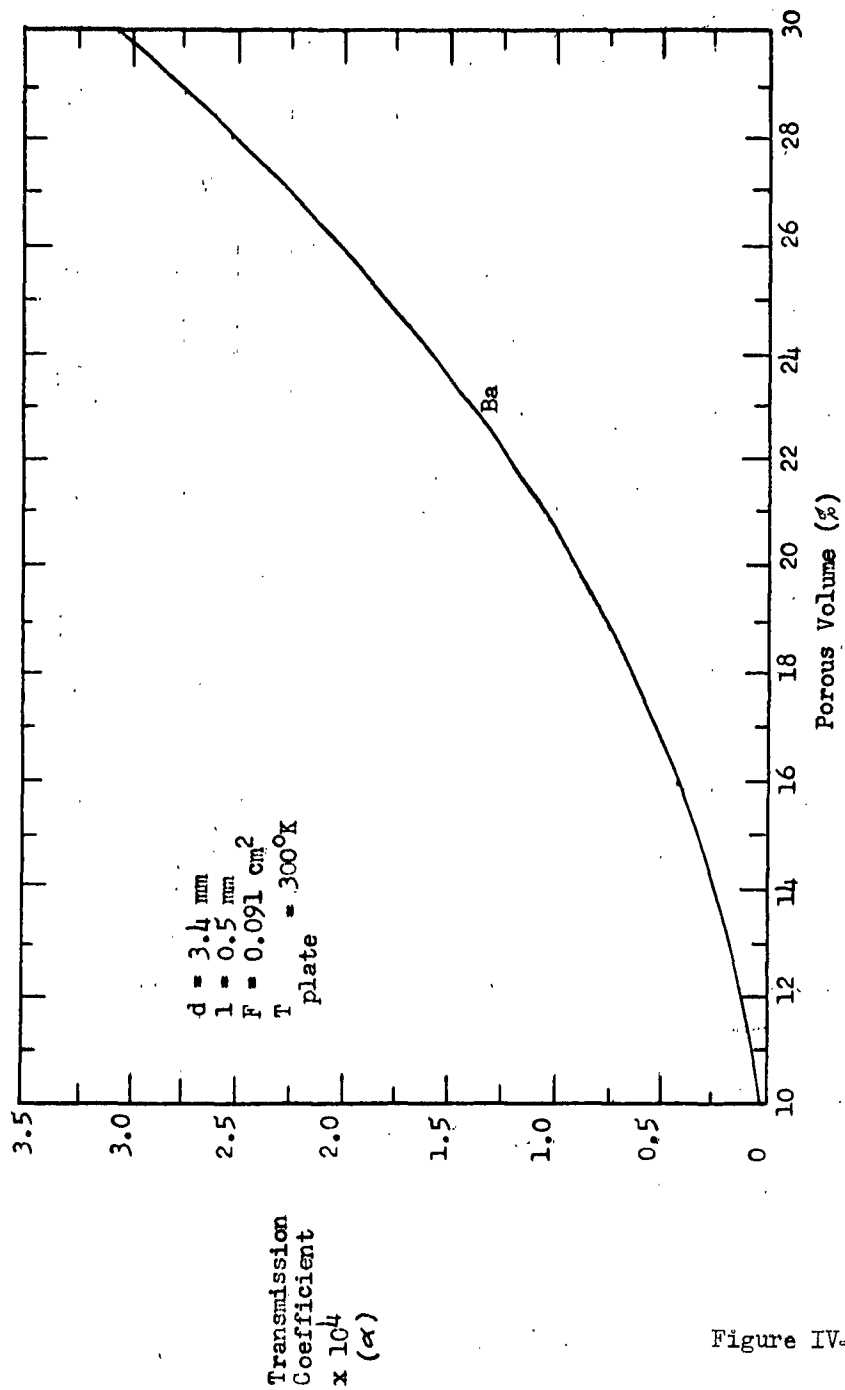


Figure IV-21

TRANSMISSION COEFFICIENT VERSUS POROUS VOLUME FOR BARIUM THROUGH POROUS PLATE

The experiments with the porous plates described previously may give only limited data, which may be insufficient for the design of porous emitters. Therefore, at a later date it is suggested that these investigations be extended to a greater number of porous plates, with porous volumes in the range between 15% and 40%. In addition, the effects of grain size, grain form, grain size distribution, sintering pressure, and temperature should be investigated, with grain sizes in the range of 10μ , 3μ , 1μ , 0.3μ , and 0.1μ . The sintering temperatures should be at least above 2000°K to avoid shrinkage at working temperatures. Because the consolidation effect may be small in comparison with other grain forms, spherical grains seem to be promising and should be evaluated in subsequent experiments, although a disadvantage of spherical grains may be less stability at higher temperatures due to the lower consolidation. Very small grains (between 1μ and 0.1μ) appear to be of most interest, because the fuel distribution over the plate surface tends to equalize and, in addition, surface flow may contribute to the total flow rate, per Sears and Hill (Ref. 69 and 70) and Clausen (Ref. 71).



V. EXPERIMENTAL EVALUATION OF VARIOUS CONTACT EMITTERS

The experimental investigation of an ion source includes the measurement of the maximum ion current and of the ionization efficiency, as a function of such operating conditions or parameters as emitter material, surface temperature, surface contamination, emitter porous volume and pore size, and cesium vapor pressure or temperature. The initial measurements described herein were made in an ion gun using a Pierce gun system for ion current extraction, even though the current density of the Pierce system is known to be limited. In order to prevent back-scattering and secondary emission, a deep Faraday cage is used as the target, in front of which a suppressor grid has been mounted. Because it is difficult to prevent the ionization of the residual gas and metal vapors (other than the fuel) in the system, and in particular the emission of secondary emitters, the ion gun system does not provide accurate readings. It is particularly difficult, even with the application of a magnetic field perpendicular to the beam, to distinguish between ions of different mass. To overcome the aforesaid difficulties, a mass separator had been constructed and will be used in later tests to provide more accurate data. The mass spectrometer is described later.

A. Ion Gun

Figure V-1 is a schematic of the apparatus. The fuel container is connected to the porous emitter plate by a $\frac{1}{4}$ in. tube. The cesium capsule is placed in the fuel container (a nickel tube) and externally broken after thorough evacuation and outgassing. Before the capsule is broken, the fuel side is pumped directly by a bypass system connected to the pump; the connection is closed before the capsule is broken. During the experiments, the fuel container is heated by hot air. It is possible to maintain the fuel temperature constant within about 3°K in the range up to 250°K . The fuel vapor pressure corresponds to the lowest temperature in the fuel system. The vapor which penetrates through the plate is ionized on the surface and accelerated by the Pierce system toward the Faraday cage. Figure V-2 is a photograph of the first ion gun assembly. The system has since been modified and improved, although the principle remains the same.

The emitter is heated by RF; data are given in Figure V-3. The matching between the RF coil and the emitter plate is not particularly good with the design shown in Figure V-1; an estimate of 10% power efficiency has been made. By design and proper coil configuration, the matching can be improved, but is not required at present for the ion gun experiments, since the desired emitter temperature can easily be attained. As shown in Figure V-3, the position of the coil can be altered to



improve the matching. The focusing and acceleration electrodes in the apparatus have been slotted to reduce the undesirable effect of RF heating of the electrodes. In the first experiments it was noted that electrode heating was excessive; therefore the electrodes are now made of parallel tungsten wires, with excellent results. The use of tungsten, with its high work function, results in a reduced field emission from the acceleration electrode.

To the right of the acceleration system are shown the suppressor grid and the Faraday cage. The entire apparatus is mounted in a two-inch Pyrex tube which permits easy outgassing; only glass or metal is used, including the vacuum gasketing. The magnetic pole pieces shown in Figure V-1 are used to deflect the ions so that neutrals can be measured with the Langmuir probe in the Faraday cage. With a four-inch gap between the accelerating electrode and the suppressor grid, a 1200 gauss magnet field will deflect the 200 volt-accelerated beam. The next gun to be built is designed with a 15-inch gap and will permit accelerating potentials up to 10kv.

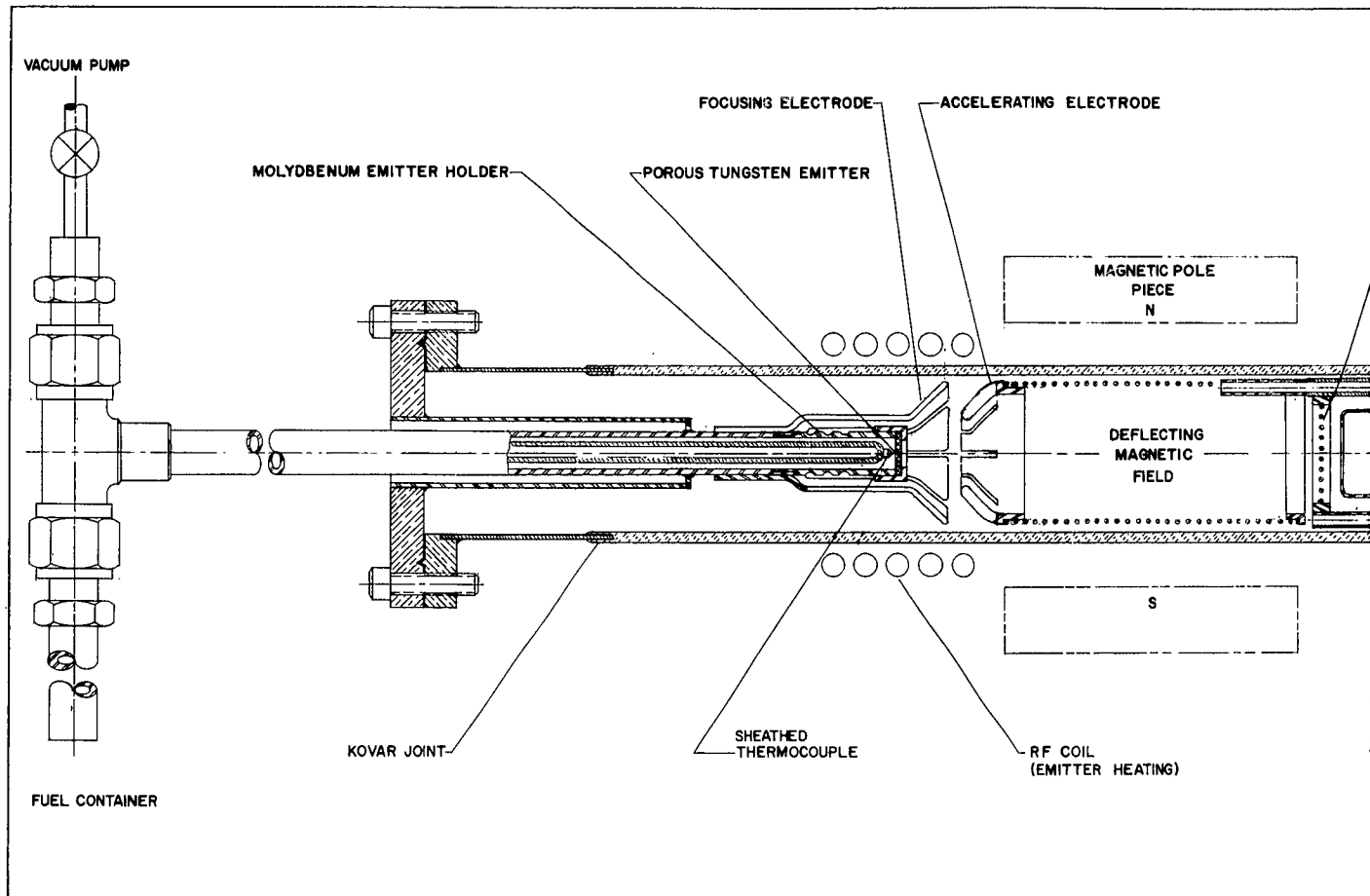
Figure V-4 shows the wiring diagram of the ion gun. The acceleration electrode and Faraday cage currents are measured separately; instrument ranges are from 30 μ A to 300 mA in five steps. The instruments are both on the ground (negative) side of the circuitry and only the fuel temperature is measured on the high voltage side. Because of the low voltage drop in the instruments, the accelerated potential is measured directly at the high voltage source (maximum 9kv and 100mA). Included between the grounded F-cage and the suppressor grid is a second potential source, adjustable between 0 to 500 volts, with the negative potential on the grid side.

The experimental program for the evaluation of the various emitters described in Section III is in progress. The results described below pertain to the P-1 emitter (sintered tungsten plate, 17% porous volume, 0.060 in. thick), mechanically bonded to a molybdenum tube. The test procedure and results are as follows.

After outgassing the ion gun and the fuel container for several hours, the fuel side was disconnected from the pump and the plate heated to $\sim 1900^{\circ}\text{K}$ for approximately 10 minutes. Subsequent experiments were made with emitter plate temperatures in the range of 1600°K . Operating vacua between 10^{-6} and 10^{-7} mm Hg were obtained. It was noted that each time the plate was heated, the pressure in the system increased slightly, possibly because of metal vapors (other than cesium) inside the gun system. During the experiments the pressure (measured with an ionization gauge between the ion gun and diffusion pump) increased



CURTISS-WRIGHT CORPORATION • RESEARCH DIVISION



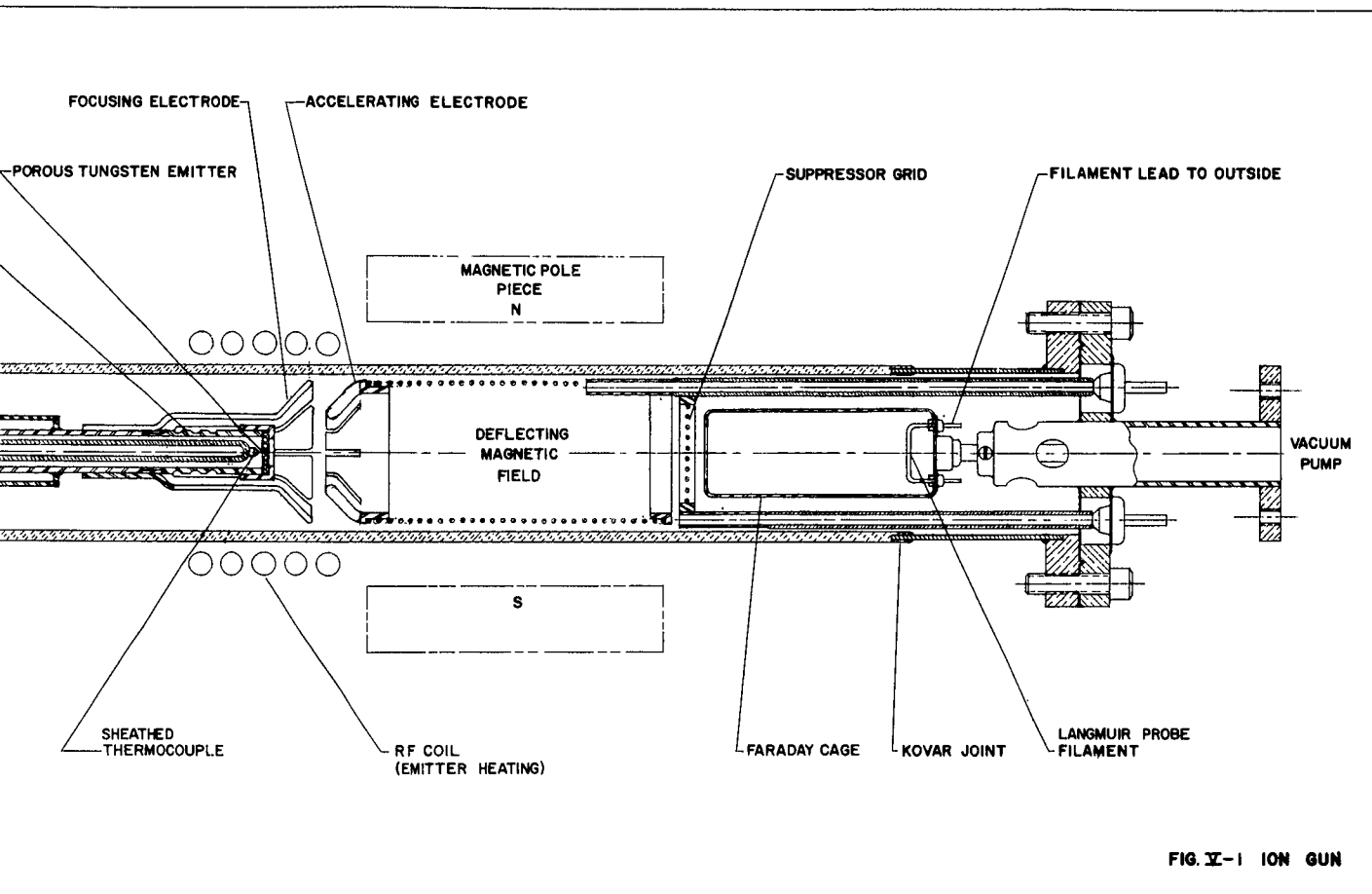


FIG. 1-1 ION GUN

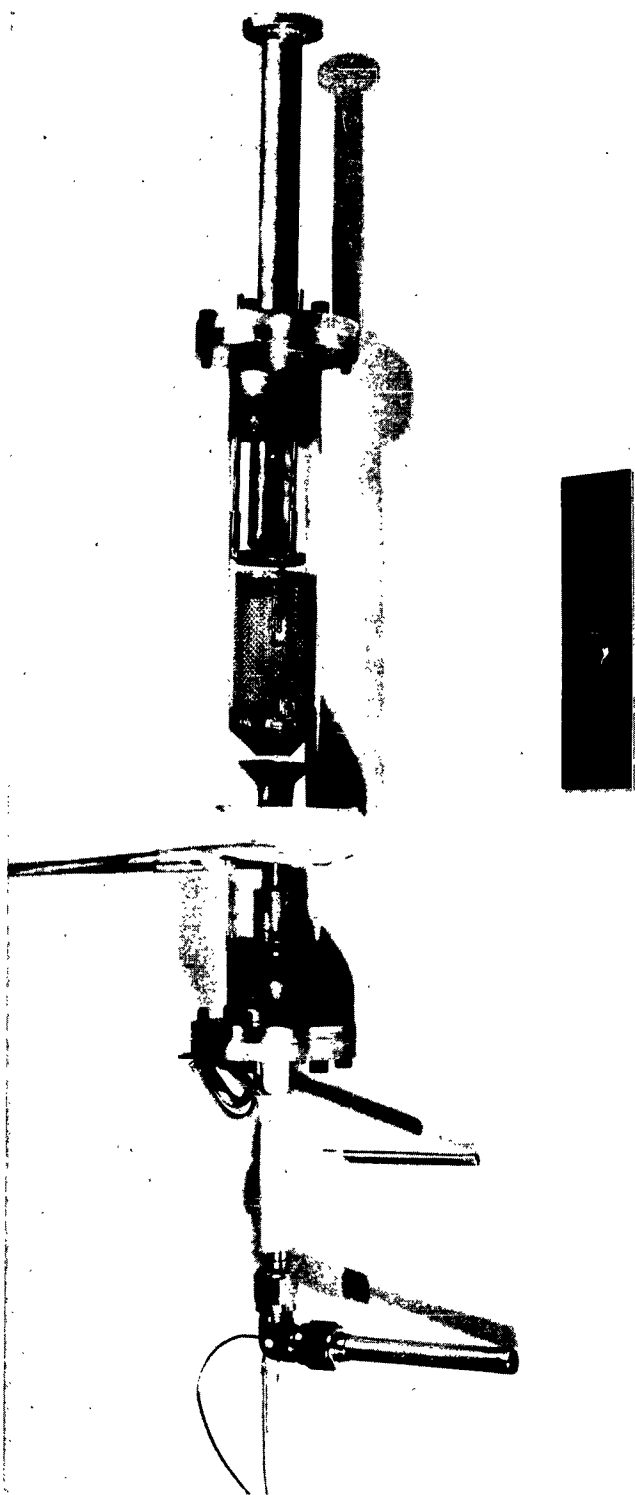


Figure V-2

Ion Gun Assembly - Photograph

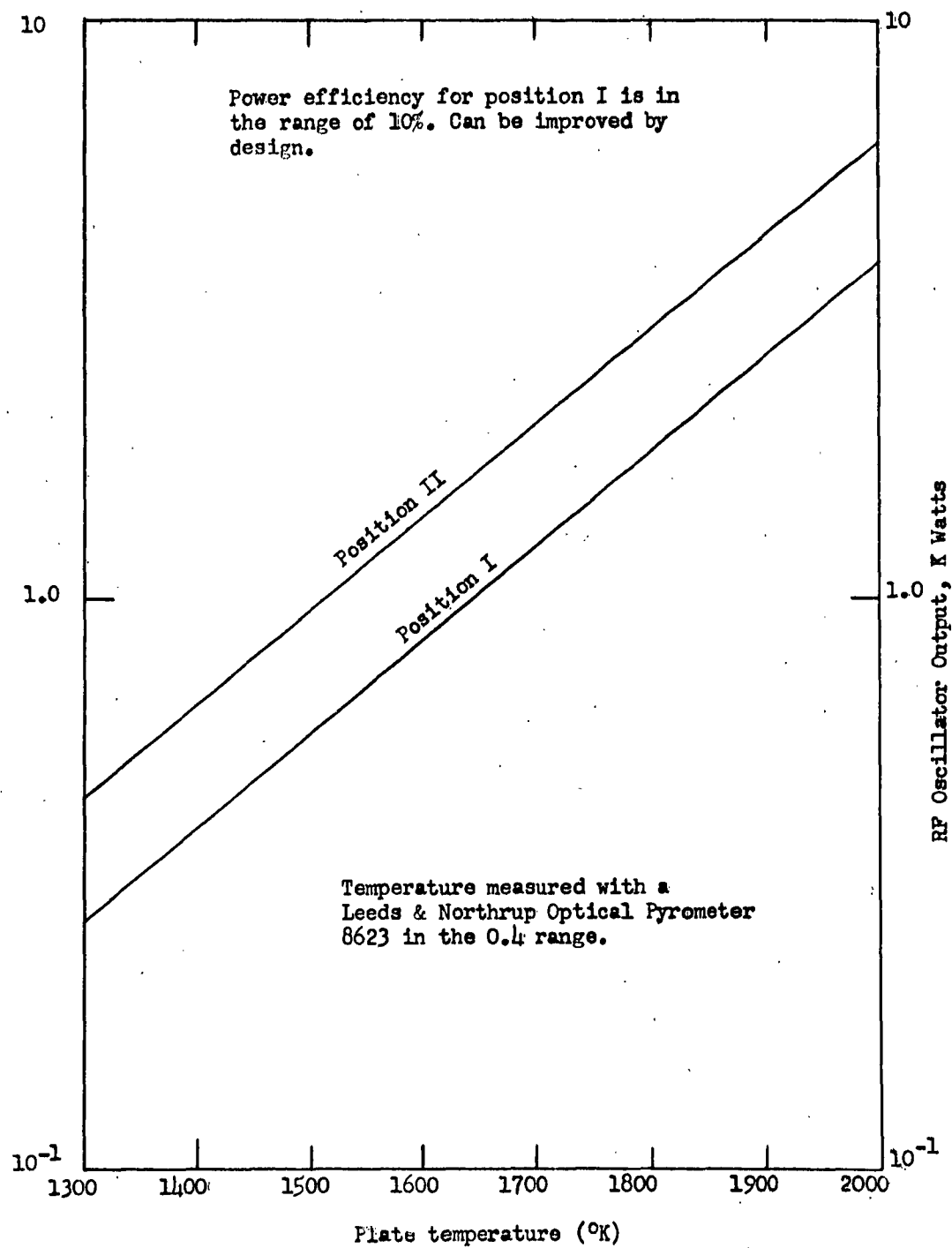
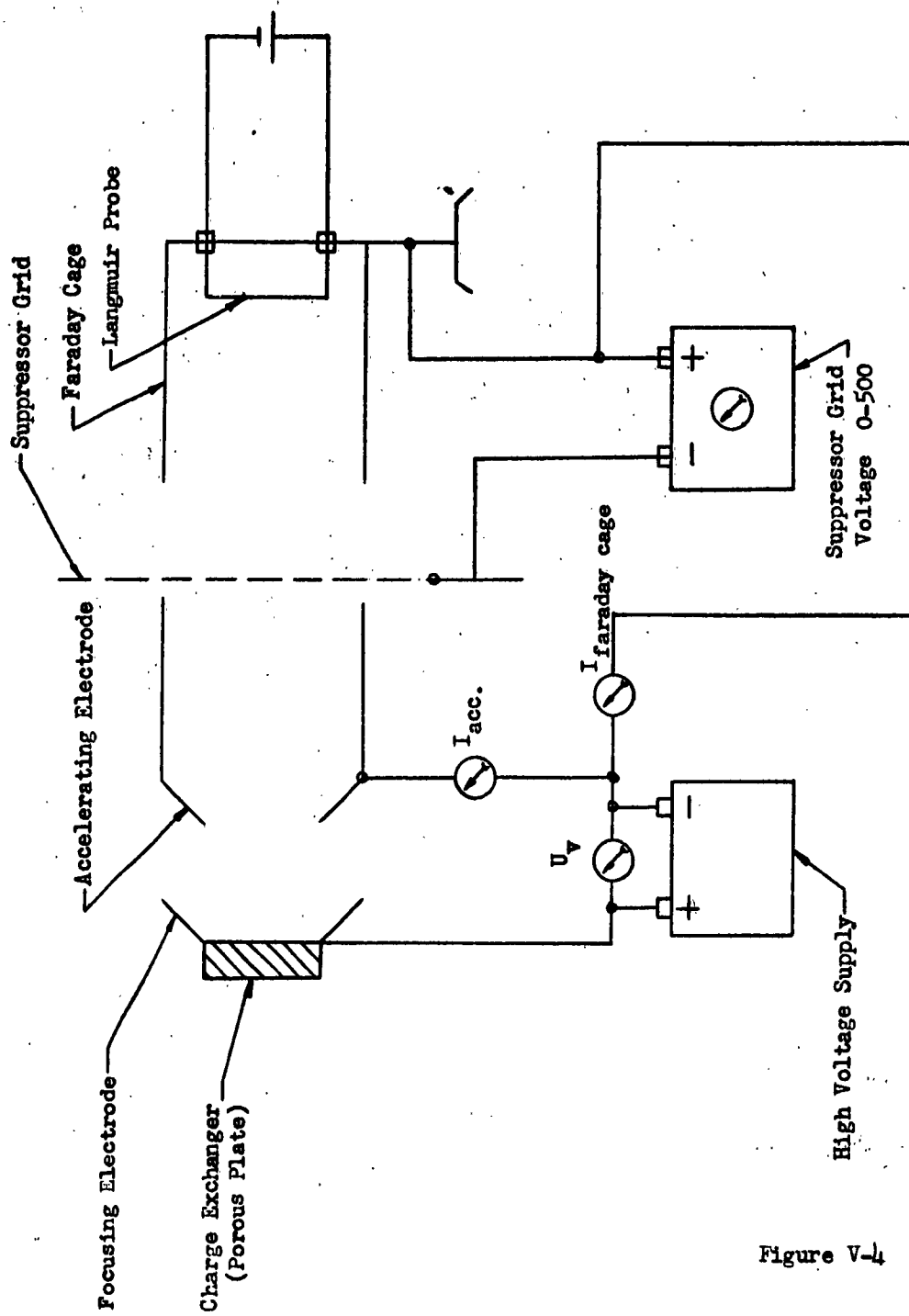


Figure V-3

RF HEATING OF THE P-I POROUS TUNGSTEN EMITTER



WIRING DIAGRAM FOR ION GUN

Figure V-4

also with the acceleration potential, Figure V-5. This effect can be attributed to dirt or residual gases, and is reduced with time.

The first ion gun investigation was made without the focusing electrode. In contrast to the usual Pierce gun beam confinement, the main current was measured at the accelerating electrode, when both the accelerating electrode and F-cage were held at the same potential. Only a small fraction of the current reached the F-cage. The measured data follows the $U^{3/2}$ law. The results are higher than had been predicted theoretically due to secondary emission. As shown in Figure V-6, the ion current is dependent on the fuel temperature (fuel vapor pressure). These first experiments were confined to the molecular flow range, in which the fuel flow rate is proportional to the pressure differential; i.e., the ion current follows the slope of the fuel saturation vapor pressure. In Figure V-7, the diffusion flow rate (theoretical current) measured as described in Section IV with a plate temperature of 1200°K , is shown plotted in microamps per square centimeter and is compared to the experimental results. The dotted curves show the measured ion currents versus fuel temperature at an extraction potential of 1kv. The plate temperature has only a small influence on the diffusion because the reduction in the diffusion rate with $1/T^{3/2}$ is overcompensated by the sharp increase of the flow rate with the vapor pressure. Even with extensive outgassing, apparently enough dirt was in the system to give the result shown in Figure V-7 for the "First Experimental Result." The second test is considered to be more reliable.

At a plate temperature of 1600°K a maximum cesium ion current of $10^4 \mu\text{amps/cm}^2$ is possible, using the values for lifetimes given by F. Knauer, (l.c.) with 0.3% surface coverage as shown in Figure V-8.

Figure V-9 shows the total current (F-cage current plus the accelerating electrode current) and the accelerating electrode current alone versus the extraction potential for the first extraction system (without the focusing electrode), and without fuel. The difference between the curves is small, indicating a small F-cage current. During the measurement the fuel temperature was 70°F , below the cesium melting point. The current changed with each reading and decreased considerably with operating time of the gun. This current is a spurious reading and could be misconstrued as a legitimate reading in an ion gun device.

Addition of a focusing electrode to the system provides proper beam confinement. The Pierce system was designed by an analog method, using electrical resistance paper in which lines of equal resistance, corresponding to lines of equal potential,

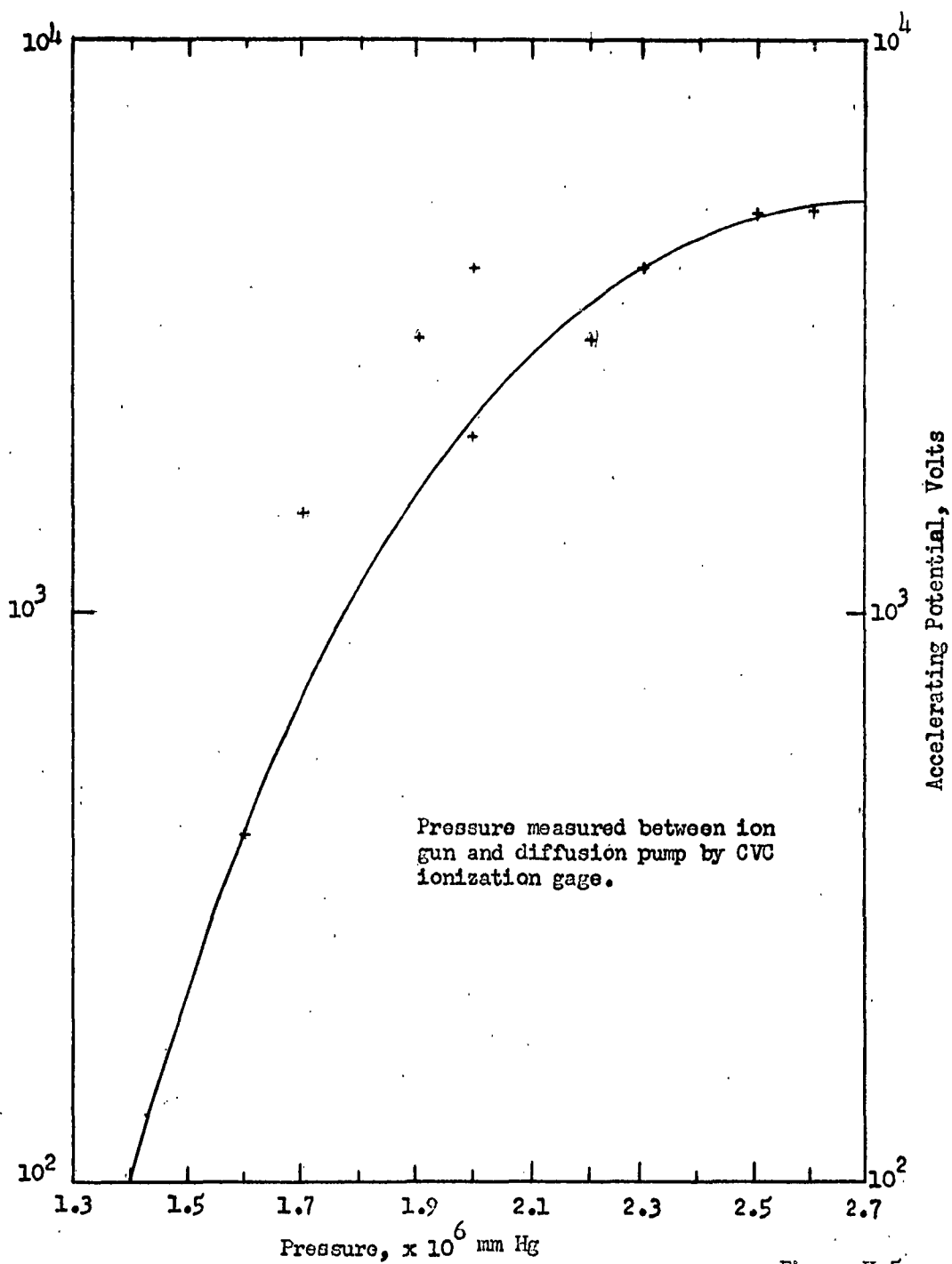


Figure V-5

PRESSURE INCREASE IN THE ION GUN AS A FUNCTION
OF THE ACCELERATING POTENTIAL

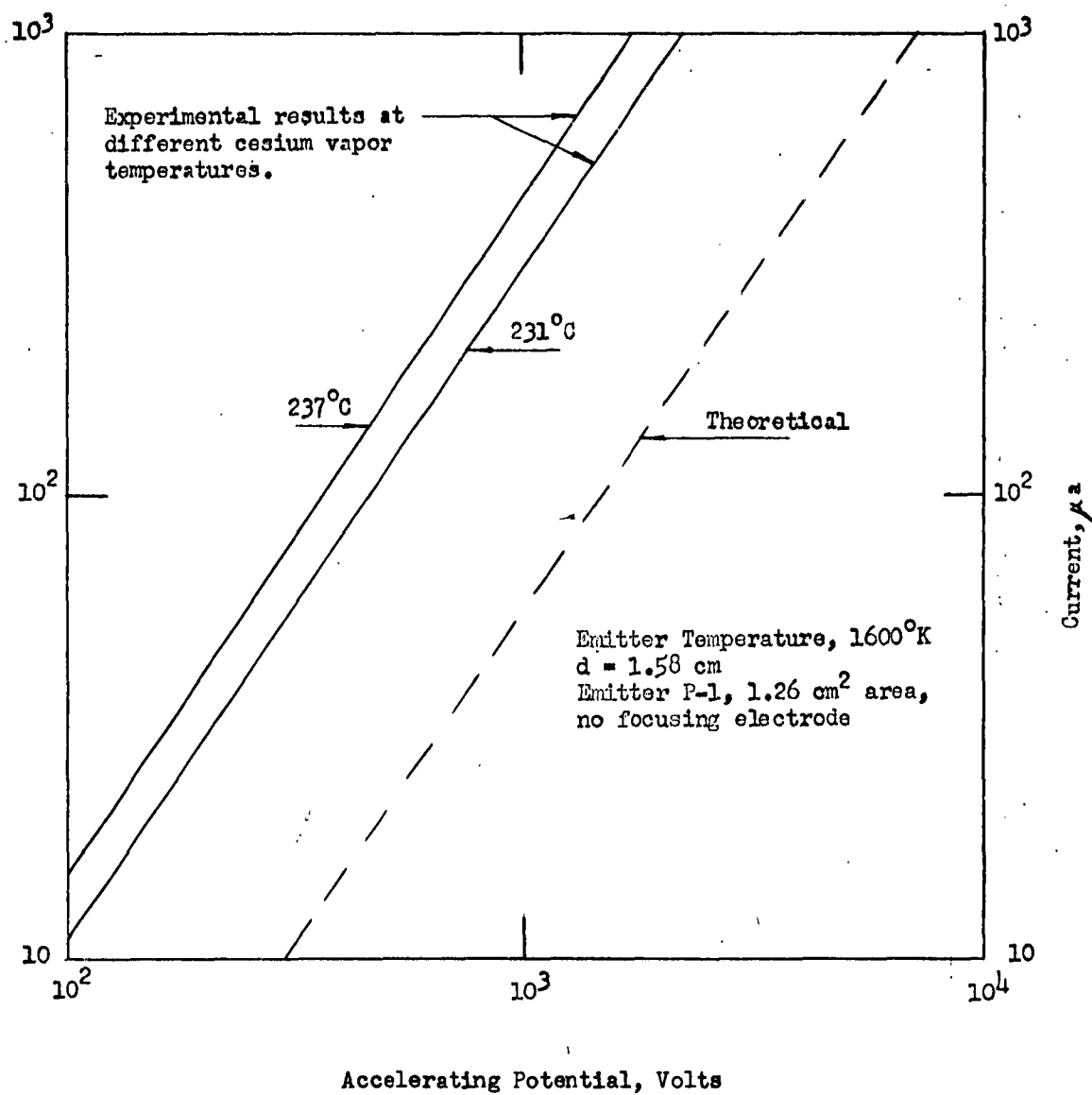


Figure V-6

EXPERIMENTAL RESULTS WITH P-1 EMITTER IN FIRST TEST

Emitter P-1,
1.138 cm² area,
surface temperature 1600°K

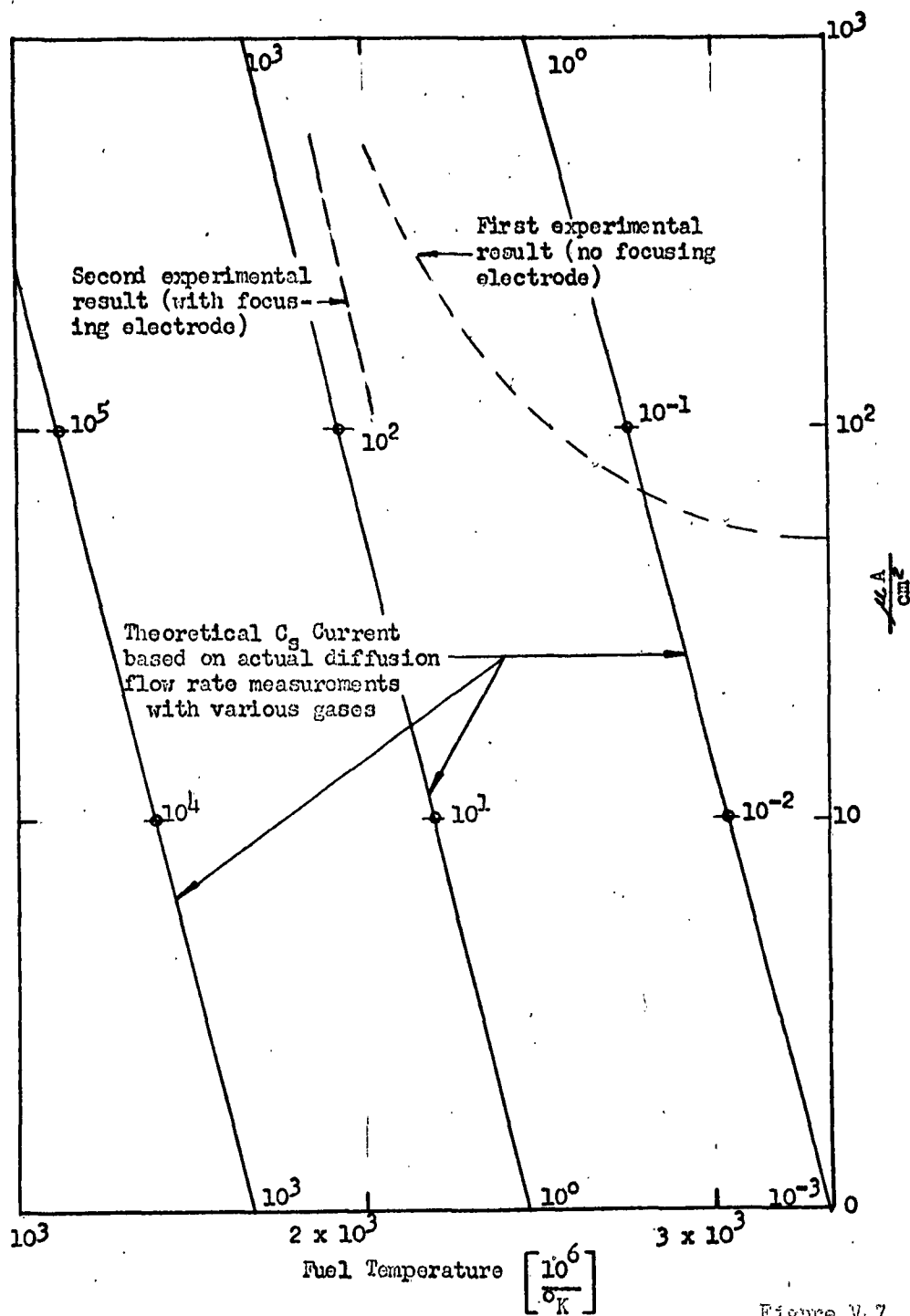


Figure V-7

DEPENDENCE OF ION
CURRENT ON FUEL VAPOR PRESSURE (TEMPERATURE)

Without Consideration of Diffusion Flow Rate
and Extraction Potential

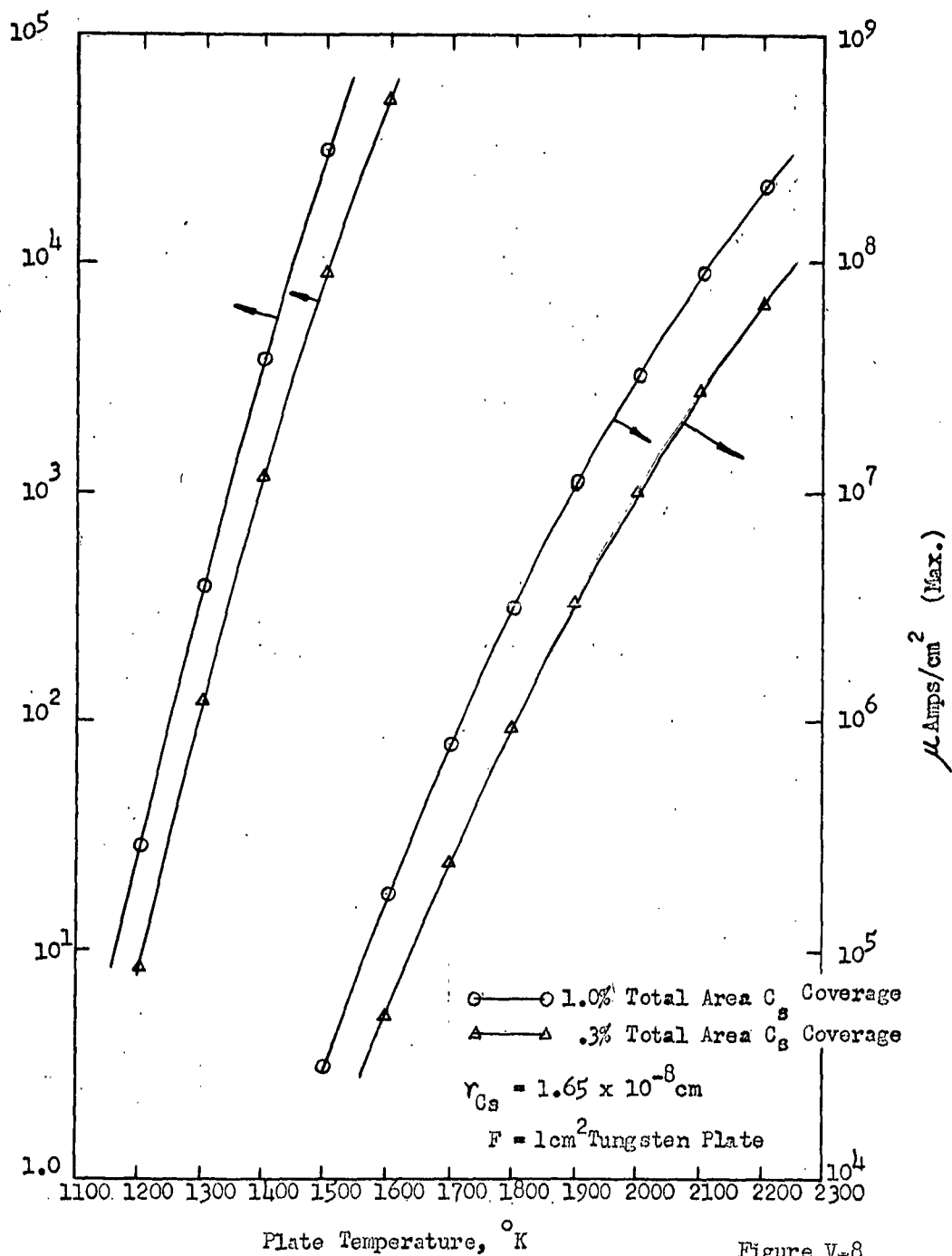


Figure V-8

THEORETICAL DEPENDENCE OF ION CURRENT
ON PLATE TEMPERATURE

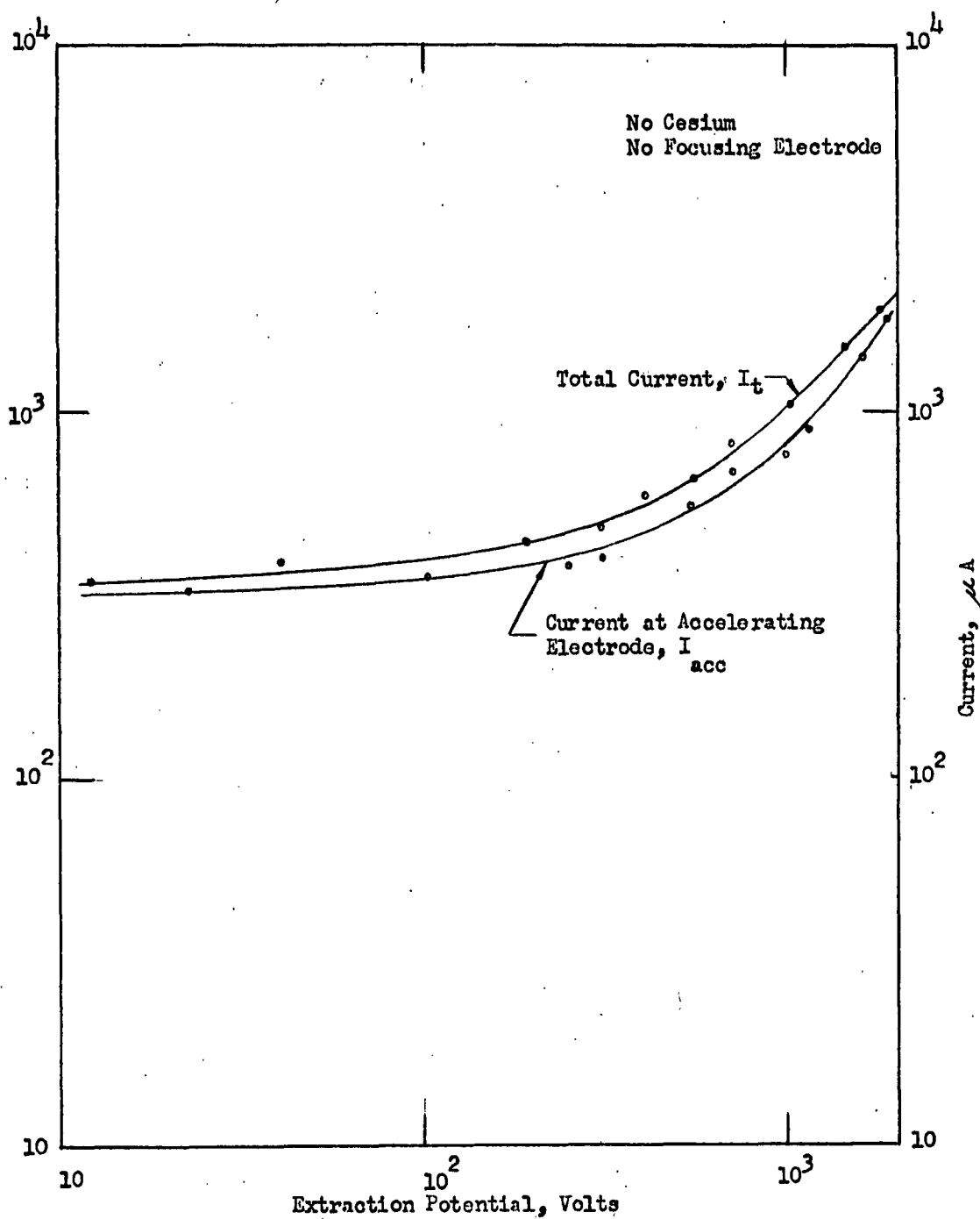


Figure V-9

ION GUN CURRENT WITH RESIDUAL GASES

were plotted for different electrode and F-cage arrangements. The ion path was then constructed by application of the deflection law:

$$\sin\alpha/\sin\beta = (U_2/U_1)^{1/2}$$

Beam spreading between the accelerating electrode and the F-cage is assumed to follow the law

$$\text{tg}\alpha = r_0/4d$$

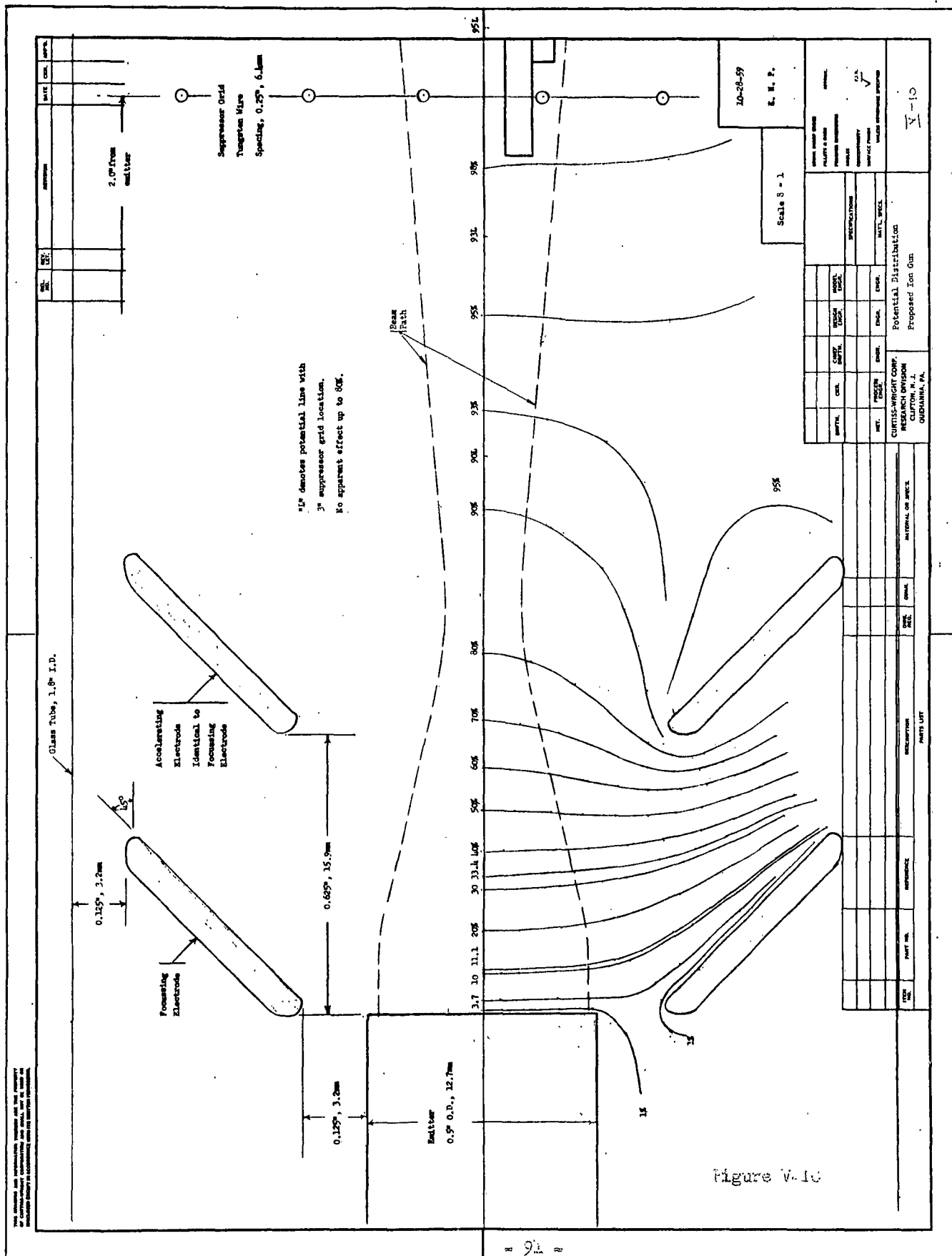
where r_0 is the emitter radius and d is the electrode spacing. Figure V-10 illustrates the analog potential distribution and the computed beam path; the deflection law is illustrated in Figure V-11. Considerably different current distributions are measured in comparison with the previously discussed readings without the focusing electrode. As expected, at high potentials, the principal current is measured at the Faraday cage and only a limited amount reaches the accelerating electrode, as shown in Figure V-12. The F-cage current follows a square rather than the predicted $3/2$ law; the current appears to be approaching a saturation value of several hundred μA .

After the emitter had been in operation for five hours, the current reading due to residual gases (measured at 300°R fuel temperature) had been reduced to a small value as shown in Figure V-13. The accelerating electrode current approached a constant value at higher accelerating potentials. The F-cage current varied between a $3/2$ and a quadratic slope, as the potential was increased and decreased.

In the experiments to date, the accelerating potential has been limited to a maximum of 5kv, but higher voltages will be used in the next investigations. The complete separation of ions from electrons has not yet been accomplished, but is also planned for the next experiments, which will include the determination of the neutral ratio by use of the Langmuir probe. Experimental results for all of the tested emitters will be included in the final report.

B. Mass Spectrometer

A magnetic mass-separator offers some advantages for the investigation of ion beams. The effect of ions coming from oil, grease, or residual gases is eliminated by adjustment of the magnetic field. Secondary electrons are trapped in the deflecting field and as a result the ion current measurement is not affected. In the previously described ion gun the magnetic



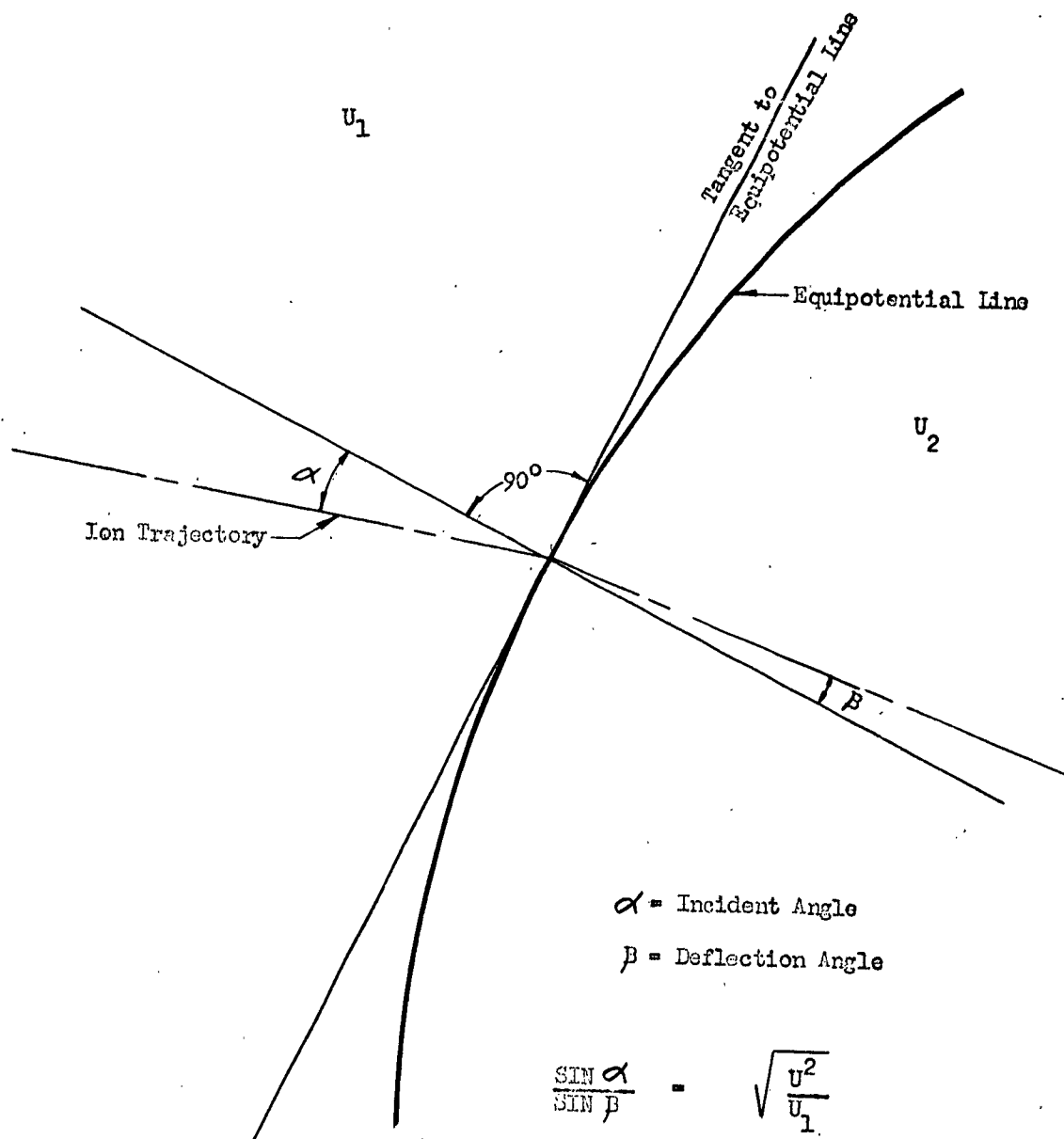


Figure V-11

CONSTRUCTION OF ION BEAM TRAJECTORY

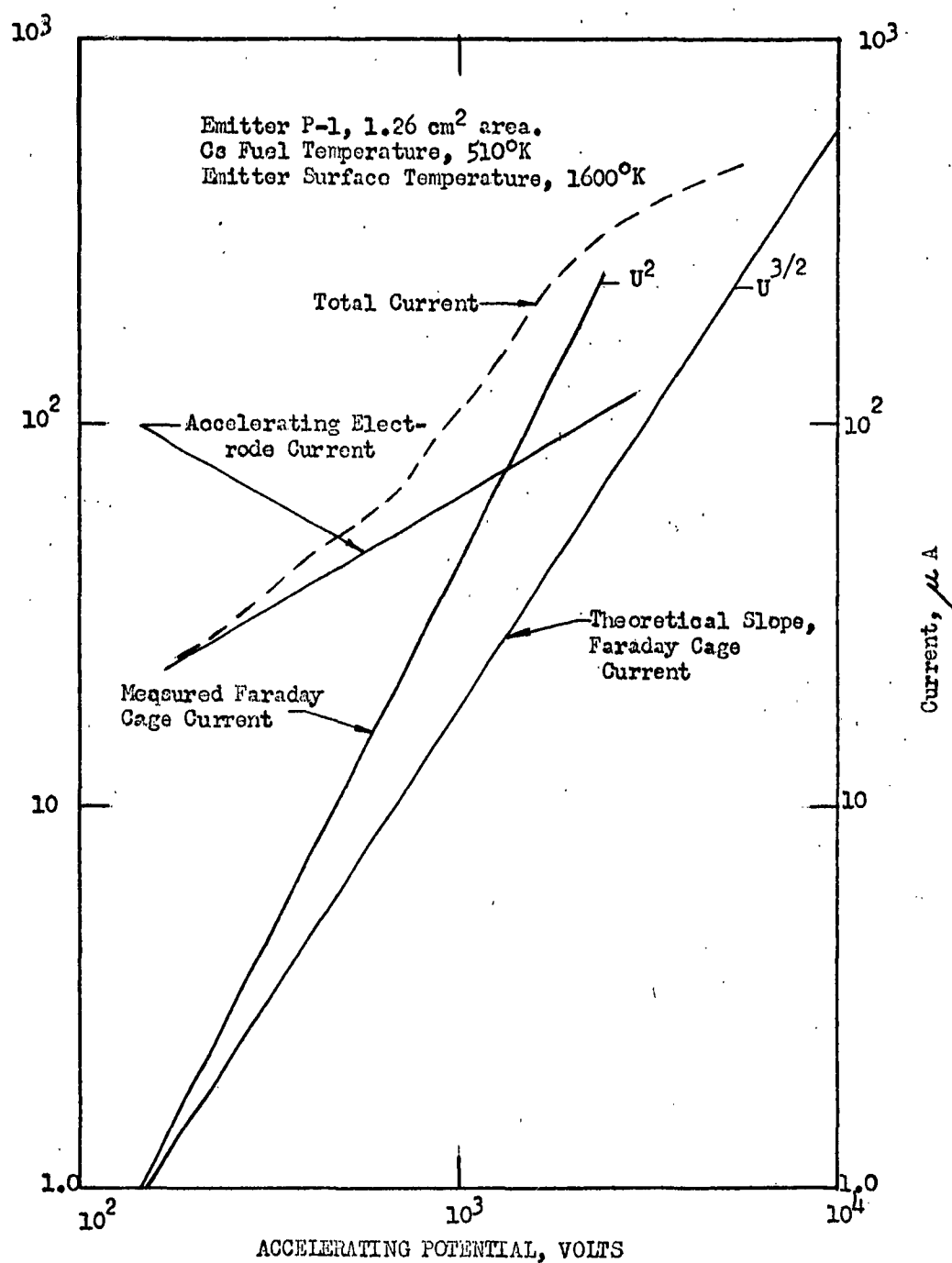


Figure V-12

EXPERIMENTAL ION CURRENT
WITH P-1 EMITTER USING FOCUSING ELECTRODE

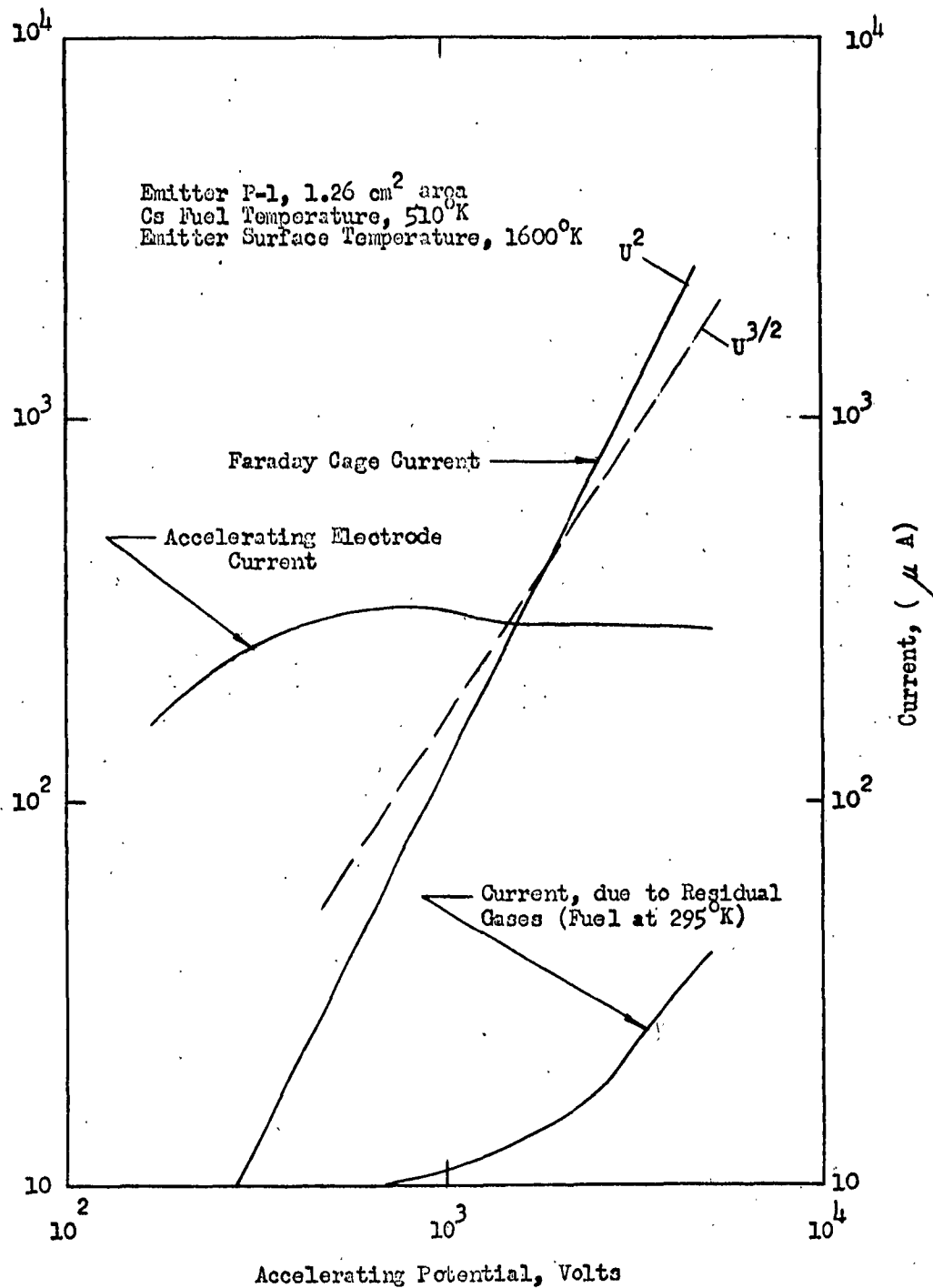


Figure V-13

EXPERIMENTAL ION CURRENT
WITH P-1 EMITTER, AFTER FIVE HOURS OPERATION

field is used only when neutrals are to be detected, whereas in the mass spectrometer continuous measurements can be made.

Figure V-14 is a sketch of the mass spectrometer. Briefly, the ion source is located at the lower left extremity of the beam tube. The beam tube is split within the magnetic field iron blocks, the neutrals flowing in a straight line to the Langmuir probe at the upper right of the sketch. The ion beam is deflected by the magnetic field and is measured in a Faraday cage at the right. Figure V-15 is a photograph of the spectrometer during assembly. The iron blocks with the inserted wrapped magnetic field coils are at the center of the photograph, with the beam tube projecting to the right where the ion source is attached. The tube is gold-plated to provide an equal potential distribution. A hot oil system is used to heat the tube to prevent cesium vapor condensation. The heating tubes are wrapped around the beam tube as visible in Figure V-15; the oil storage tank is at the upper right with a pressure gauge; the oil heater is below the table. At the far left, the valves for the vacuum system (not connected at the time this photograph was taken) are visible.

With the known ion mass, a direct determination of the pulse ($H \cdot \mathcal{V}$) is obtained, and thus an independent method for thrust measurement, where H is the magnetic field strength in gauss and \mathcal{V} is the curvature in the field. Investigation of the ionization efficiency at various operation conditions is possible with this equipment, in particular because the neutral ratio can be measured continuously independent of ion current readings.

For first investigations the unit will be operated with relatively small ion currents, using small-area emitters. The emitter design resembles that of the ion gun with regard to the arrangement of the fuel system, the porous plate set-up, and the Pierce electrodes.

In connection with the high mass of the ions and acceleration voltage up to 20kv a field strength up to 9k gauss in the gap is required. A 60° type spectrometer was designed, where

$$\mathcal{V} = 144 (M_1 U_B)^{\frac{1}{2}} / H$$

and

$$\sin \alpha = 6.95 (10^{-3}) (H) (L) / (M_1 U_B)^{\frac{1}{2}}$$

where

$$\begin{aligned} \mathcal{V} &= \text{deflection radius, cm} \\ M_1 &= \text{fuel atomic weight} \\ U_B &= \text{acceleration potential, volts} \end{aligned}$$

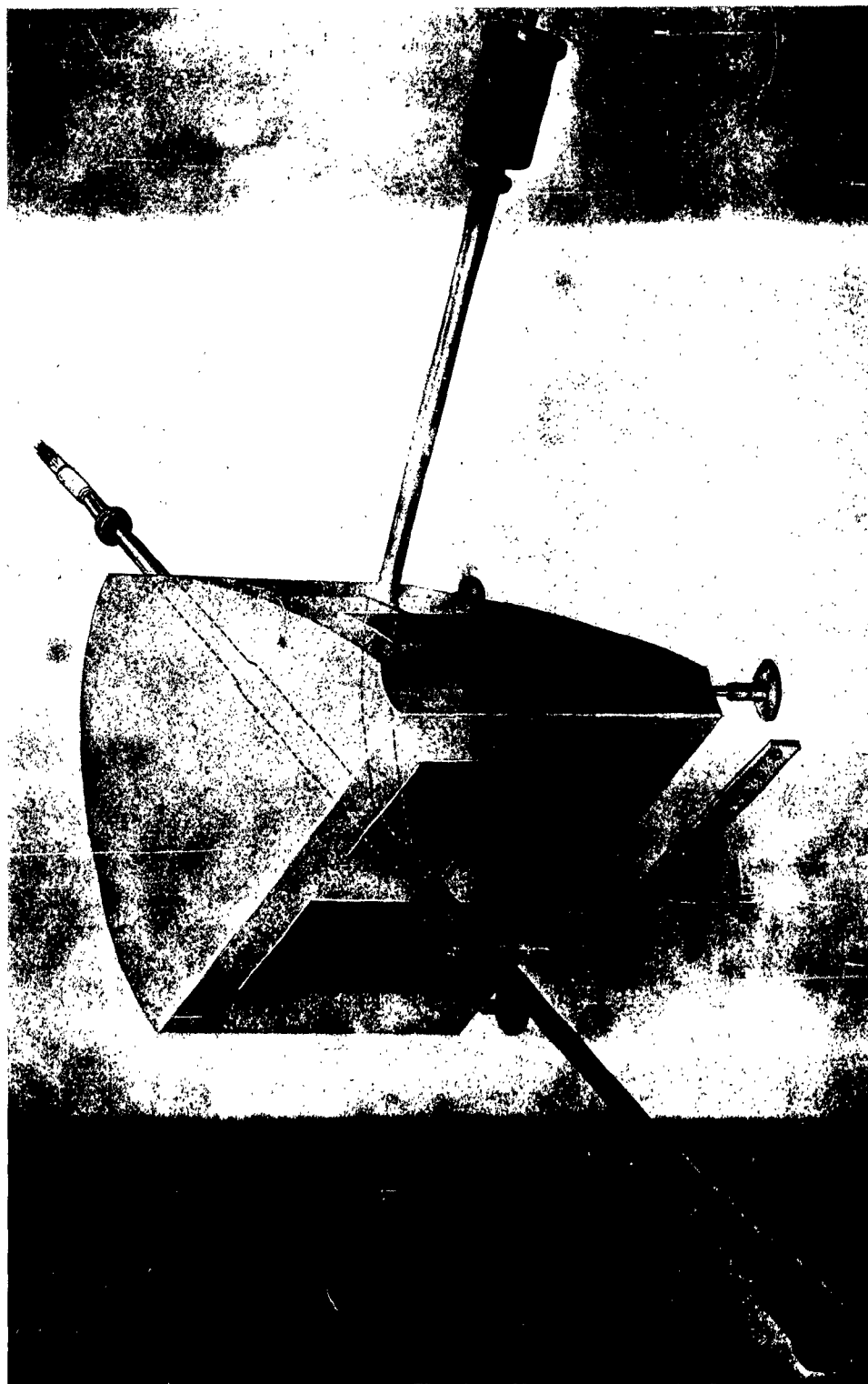
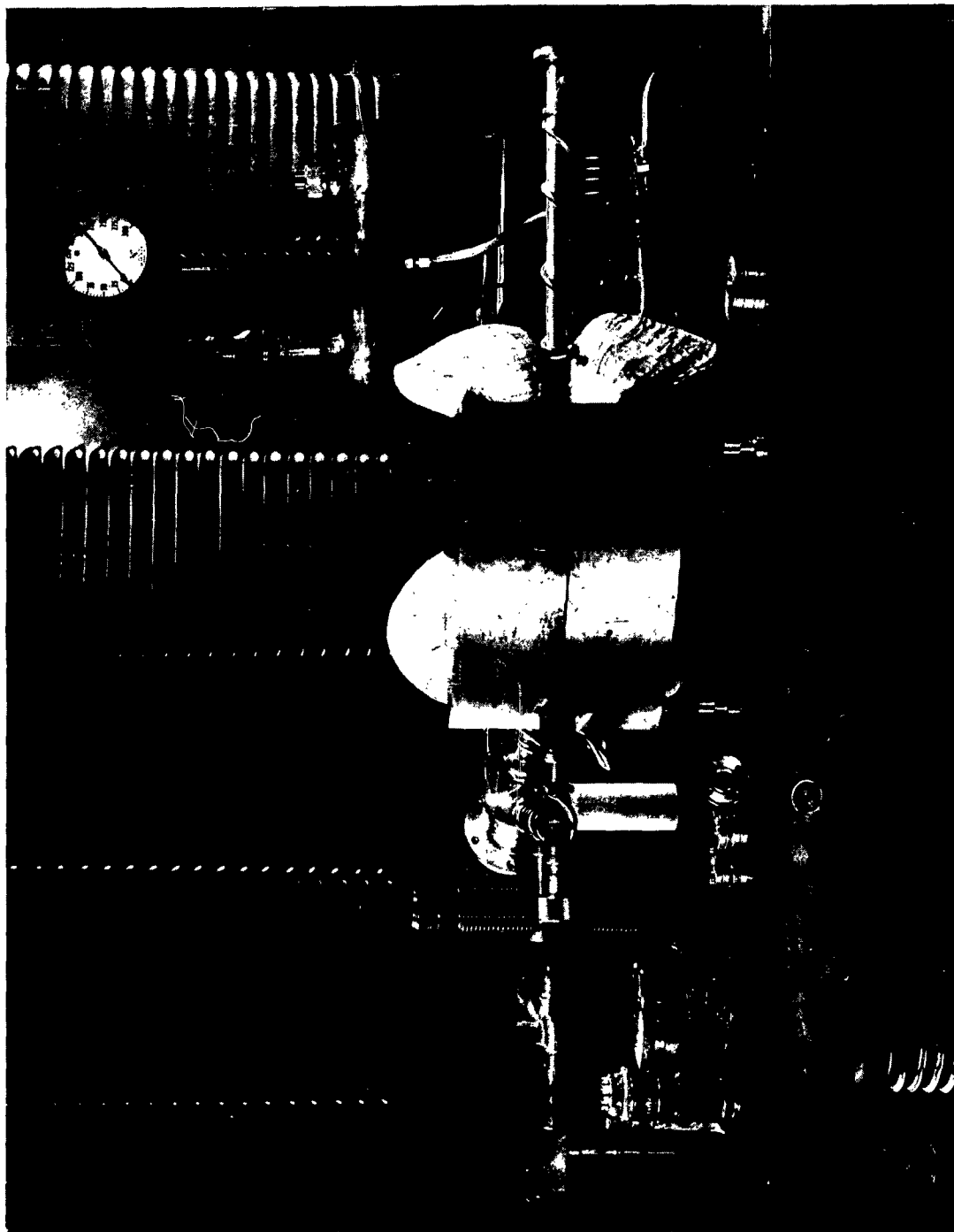


Figure V-14

Sketch of Mass Spectrometer

I I I I I I I



Mass Spectrometer During Assembly

Figure V-15

H = magnetic field strength in the gap, oersted
 L = length of deflection

To provide high saturation magnetization, the split metal block is made of Armco Ingot Iron, well annealed. Figure V-16 shows the dependence of the gap-field strength on the product of current in amperes times the number of coil turns. The coil is made from copper wire with 1 mm² cross-section, thus allowing a maximum current of 1 amp without heating. It is possible to enlarge the gap height to 20 mm, in which case the number of turns of the coil will be reduced from the present 6100 (both coils) to about 4500, or the coil current can be increased for short durations.

In deviation from normal mass-spectrometer design, this equipment has, in addition to the curved ion beam tube, a tube arm straight from the emitter, passing through one wall of the iron block. A Langmuir Probe is placed at the end of this tube for the detection of neutrals, permitting continuous readings as previously mentioned. The curved beam tube ends in the Faraday cage, corresponding in construction to that already described in connection with the ion gun. Herzog correction and a correction of second order are considered for proper focusing of the ion beam.

At vacuum lower than 10⁻⁷ mm Hg, the maximum current is limited by beam spreading due to space charge:

$$r_2/r_1 = [4.1 (10^6) (M_1)^{1/2} (jL/U^{3/2})]^{1/2}$$

where

r_1 = beam radius leaving the Piereve gun, cm
 j = current density, amp cm⁻²
 U = accelerating potential, volts
 L = distance from Pierce gun, cm
 M₁ = atomic weight

The space charge can be compensated by neutralization of the beam with slow electrons. Electrons can be produced by collision of beam ions with residual gas atoms (gas pressures down to 10⁻⁴ mm Hg) or by secondary electrons from the tube walls. To avoid any reaction of the fuel with the gas, an inert flush gas will be used in our design.

The ion space charge in the uncompensated beam is given by

$$P_1 = 6.3 (10^{18}) (j_1)/v_1$$

and the space charge compensation time is

$$t_x = 0.73 (Q_I) (p/p^*) (M_1/U_B)^{1/2} (10^{-6})$$

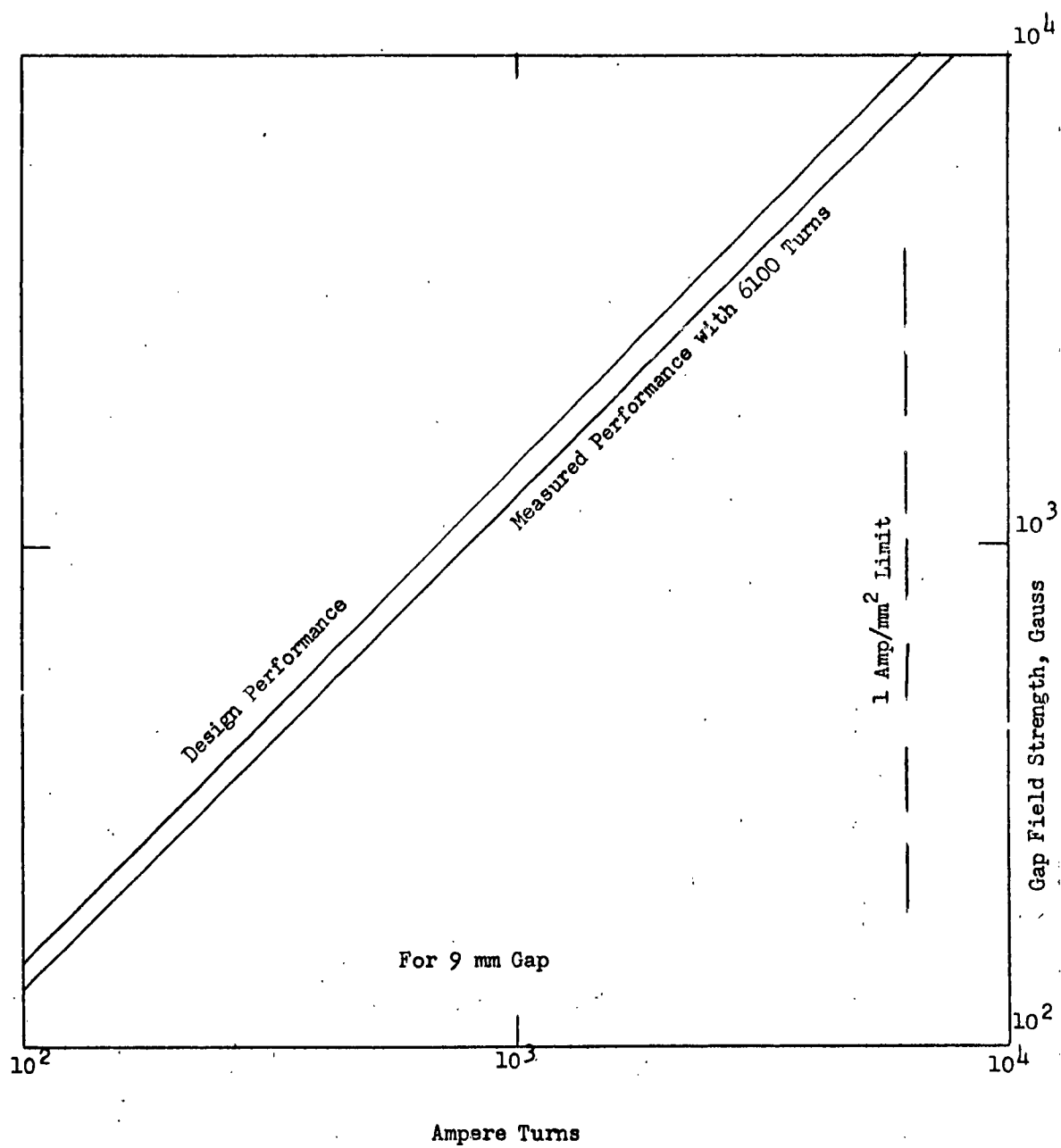


Figure V-16

FIELD STRENGTH IN MASS SPECTROMETER

where

ρ_i = space charge, coul cm⁻³
 v_i = ion velocity, cm sec⁻¹
 t_x = time, sec
 Q_I = differential ionization, depending on ions
and rest gas
 p/p^* = ratio of rest gas pressure to 1 tor

At higher gas pressures compensation times in the order of 10⁻⁶ sec are possible. Investigations on the neutralization of ion beam have been published, including Bernas and Sarrouy (Ref. 72) and Bernas, Kaluszyner, and Arnaud (Ref. 73).

The mass spectrometer apparatus shown in Figure V-15 is currently being assembled and checked.

VI. EMITTER HEATING TECHNIQUES

Several methods of heating the emitter to the required high temperatures have been and are being investigated; including resistance heating, radiation heating, RF heating, and an arc method. RF heating is being used at the present time for experimental purposes because the heating method is "clean" and eliminates components which could unduly complicate the ion source at this stage of investigation. The various techniques are discussed below.

A. Resistance Heating

The nature of the porous emitter material for the ion source makes the use of direct resistance heating difficult. Inasmuch as the fuel has to pass through the porous media with little or no by-pass effects, the rim of the porous plate must be sealed to its carrier or holding mount. Pure resistance heating rules out in many cases the possibility of a metal rim without insulation. In an early experiment, a mount was fabricated for resistance heating a round porous tungsten plate. The experimental parts and completed rig are shown in Figures VI-1 and VI-2. As can be seen from the parts layout, the round porous disc was connected on opposite sides to two copper contacts. Both the contacts and the disc were held by a split plate of high temperature insulation. Power was applied to the plate through two copper rods, passing through insulating bushings with high temperature "O" ring seals. The entire plate assembly was held in place by an upper and lower stainless steel casing. The upper face of the assembly was ground so that a small bell-jar could be placed on top; a vacuum was pulled through a connecting pipe. The plates used for this experiment were .050 in. thick and 2 1/2 in. in diameter, with 43% apparent density.

High current low voltage AC power was applied to the experimental rig from a variable high current transformer. At a power rating of 500 amps at 4 volts the plate temperature reached approximately 1000°C. At that time the insulating bushings carrying the copper connections to the plate assembly failed, causing loss of vacuum and resultant oxidation of the porous plate. The use of ceramic type insulating material in contact with the hot tungsten plate has structural limitations, as will be discussed further in Section VII of the present report. The technique shown in Figure VI-2, therefore, was judged to be inadequate for a long life emitter with no by-pass flow.

An investigation also was made of the technique of using a post electrode applied to the center of the plate, with an outer rim metal support as the second electrode. Due to the uneven temperature distribution, with the high temperatures severely concentrated at the center of the plate, the thermal stresses resulted in plate failure. Use of a screen emitter, rather than a porous plate, could minimize the failure problem, but the severe temperature distribution is a disadvantage, particularly in the evaluation of emitter performance where the plate temperature is a parameter.



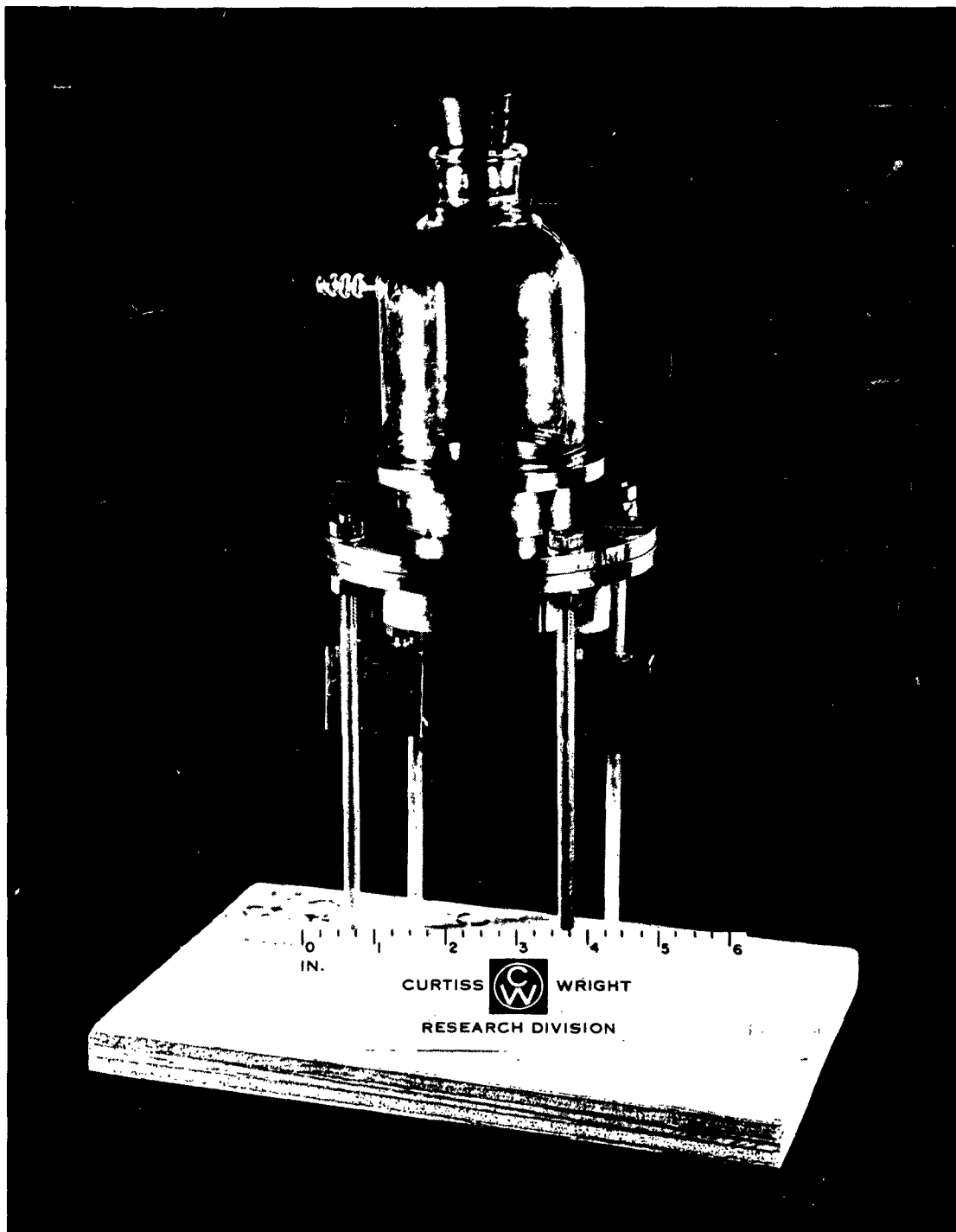


Figure VI-1. Direct Resistance Heated Ion Source - Assembly

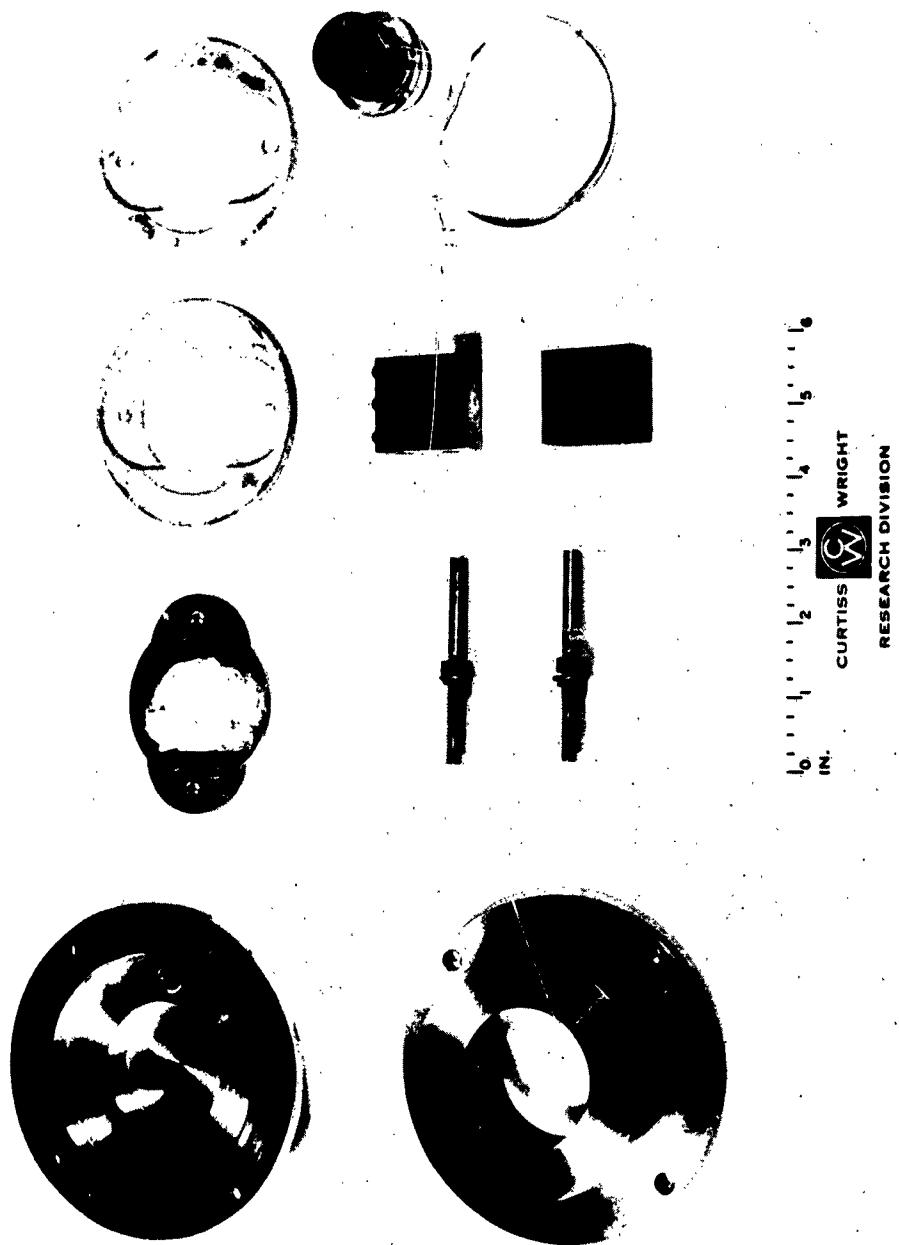


Figure VI-2

Direct Resistance Heated Ion Source - Components

B. Radiation Heating

As applied to a porous emitter, radiation heating takes place indirectly by thermal radiation from adjacent heating elements. Tests have indicated the method to be relatively effective. The tests were carried out using a porous tungsten emitter sealed into the end of a 1/2 in. molybdenum tube. A sketch of the arrangement is given in Figure VI-3. As can be seen, a tungsten filament within the tube is brought into close proximity to the porous plate. Due to the black-body condition, heating is rapid. The principal disadvantage is the undesirable complexity introduced by lead wires, insulators, and filament connectors in the ion source, where exposure to both high temperature and cesium vapor is involved. A new and simpler design, however, has been evolved and further tests will be conducted.

C. RF Heating

In considering methods of heating an ion emitter it would seem that one of the best and most efficient would be the application of RF heating. A considerable number of tests have been carried out, and this method is being used in our present ionization experiments, with a commercial RF generating unit. A tank circuit loading and matching coil allows the unit to be applied to both small and large masses for heating. Although the RF system allows "clean heat" to be applied to such items as porous tungsten plates and other types of emitters, the RF also tends to heat any metallic holding fixtures in which the plate is fastened, and the adjacent focusing electrodes. In a system, such spurious effects can be effectively reduced by proper design. The electrode heating factor is also apparent in the operation of a full ion gun assembly. By slotting the electrodes, however, the RF pick-up can be minimized and, in fact, at the present time a wire fan-shaped electrode configuration is being investigated.

An obvious question in the use of RF heating is the effect of the RF field on the ionization process itself. This effect is easily established in the experiments by observing the ion current as the RF heating current is momentarily switched on and off. Under the conditions of our present experiments, (Section V), the RF field has no effect on the ionization process.

D. Arc Heating

An arc method of heating the emitter is now being tested. This method employs a small arc which strikes from an internal central electrode to the emitter plate itself as the second electrode. A sketch of the internal arrangement of such a heating system is given in Figure VI-4. The principal disadvantage of this system is the possible erosion of the electrodes, one of them the emitter, due to "sputtering" which could alter the flow characteristics of the emitter plate. The maintenance of the arc in the cesium vapor is expected to pose no difficulties, and the subsequent internal ionization and recombination

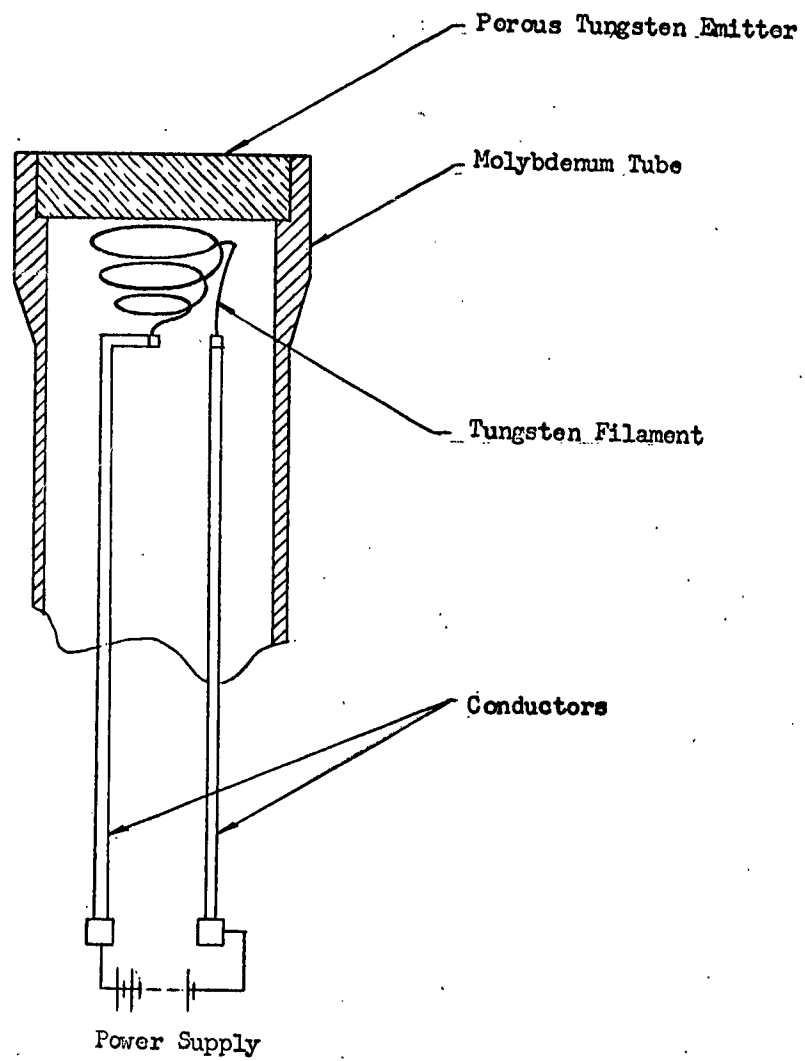


Figure VI-3

RADIATION HEATING

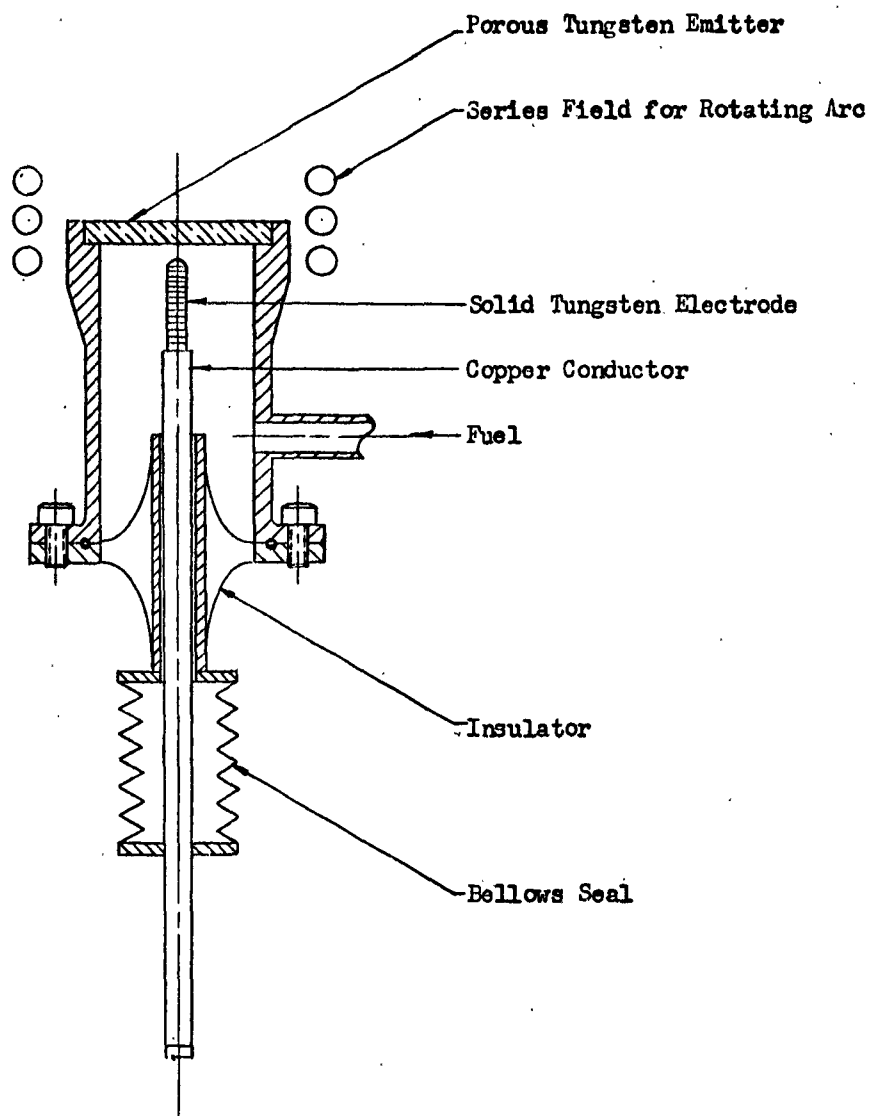


Figure VI-4

ARC HEATING

of the ions on the emitter will contribute to the plate temperature. The method is being evaluated with both an AC and DC power supply.

The choice of an emitter heating technique is highly dependent on the type of power supply available. A DC supply favors the radiation heating method without undue weight addition to the system. On the other hand, the RF system can be designed to be lightweight, and eliminates all internal components in the ion source. Each of these methods, and the arc method, are being further investigated.



VII. BONDING THE EMITTER

Investigation of methods of holding a porous sintered tungsten plate in such a manner that it can be heated to 2000°K without by-pass flow of cesium vapor around the edges of the holding arrangement, has required considerable effort. Different expansion coefficients for the materials, together with the necessity for preventing contamination of the porous media itself, complicate the problem. Four principal methods of bonding have been investigated:

- (a) mechanical joints,
- (b) brazing,
- (c) welding, and
- (d) sintering in place.

Each of the above methods is described below. At the present time, brazing with pure metals has provided the best results, although the method of sintering in place holds promise and is being further investigated.

A. Mechanical Joints

An obvious method of holding a porous tungsten plate is by means of a clamping device. As already discussed in Section VI of this report, early experiments on the resistance heating of a tungsten plate made use of a clamping method. The results indicated that if the plate is clamped tightly around the edges, in most cases cracks occur due to differential expansion. Furthermore, the rough surface of the tungsten plate is not a flat contact surface, even when tightly pressed against a completely flat mating surface. As a result, by-pass flow occurs.

A variation of the above method of holding the porous plate is used in the commercially available "L" cathode, illustrated in Figure VII-1. The holding effect is produced by pressing in the rim of the holding tube to obtain a pinch effect around the plate. It was noted in testing this type of emitter that due to differential expansion, considerable by-pass occurred. Furthermore, longitudinal cracks in the molybdenum holder (near the porous plate) were observed after approximately ten hours of emitter operation.

Another mechanical method is the use of a powder seal, wherein the plate is retained in a fine powder edge seal, as shown in Figure VII-2. The powder used for this test was tungsten oxide. The seal worked moderately well at room temperatures, but upon heating proved to be unsatisfactory due to localized compacting of the powder.

None of the above mechanical joints exhibited the desired sealing; therefore the next step was to investigate brazed joints.



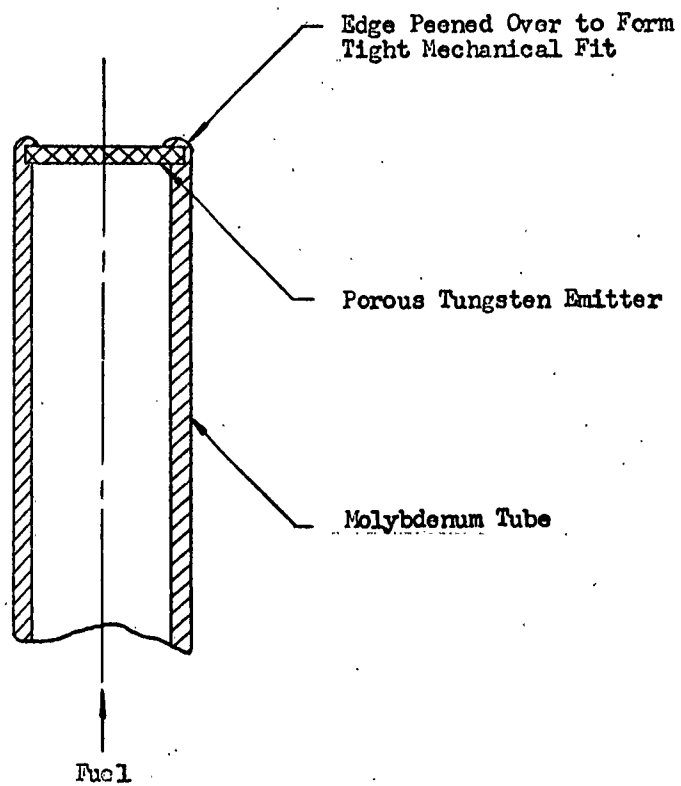


Figure VII-1

"L" CATHODE

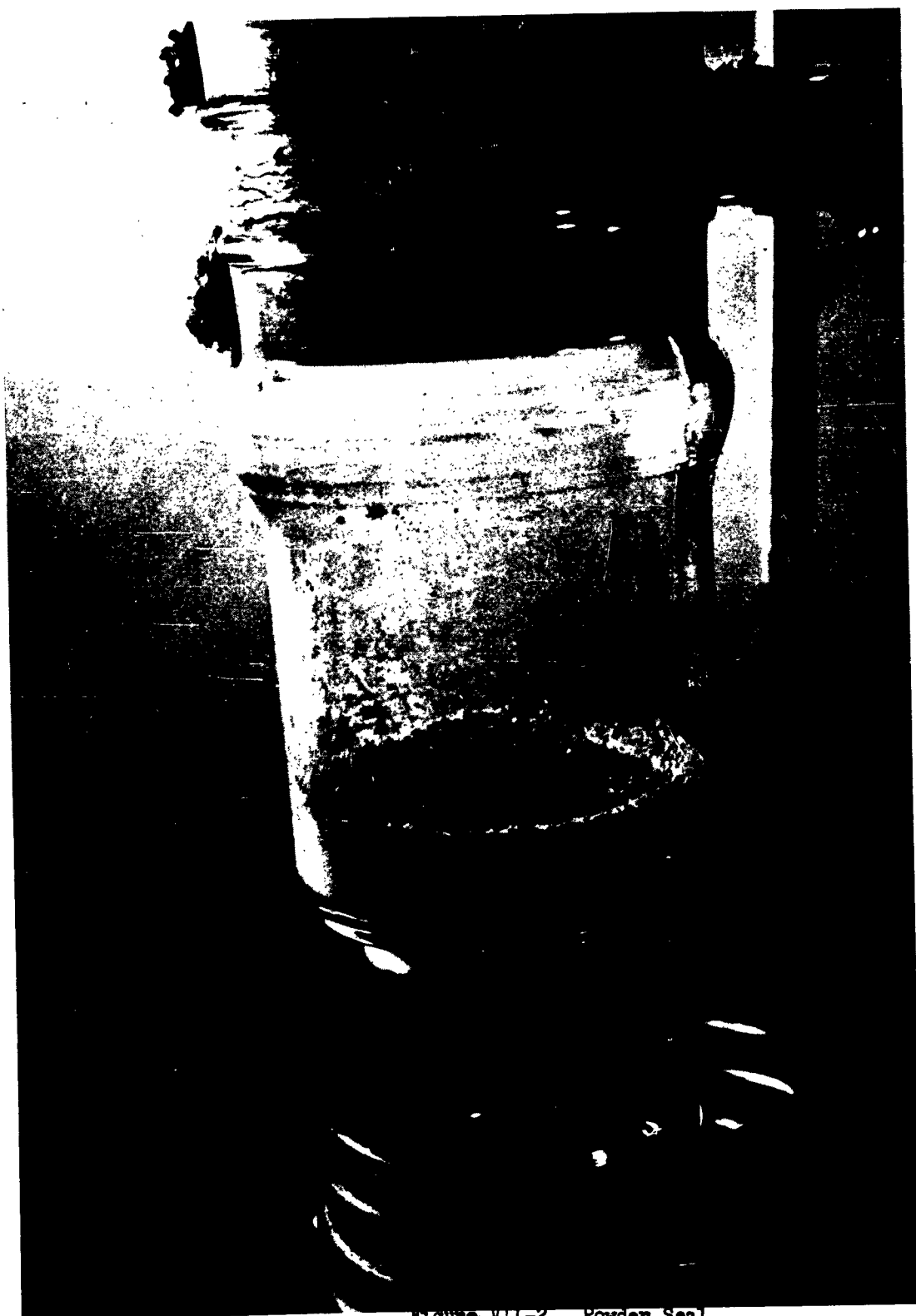


Figure VII-2. Powder Seal

B. Brazing

The drawback to any type of braze joint with sintered porous tungsten is the penetration of the braze material into the pores, and the possible contamination which could reduce the work function of the emitter. If such effects can be eliminated, however, a good braze joint made under controlled conditions gives a measure of ductility between the emitter plate and the holding fixture, which is particularly advantageous when dissimilar materials with different expansion coefficients (or similar materials at different temperatures) are being used. The experiments conducted to provide an acceptable brazing technique are described below in their chronological development.

Nickel Braze: Molybdenum cups, three inches long and one and one-half inches in diameter, were used as the holders to which the porous tungsten plates were first attached. In the closed end of the cup a hole of one-half-inch diameter was bored. The normally open end of the cup was closed and attached to a quarter-inch nickel tube for pressure checking and diffusion flow experiments. First brazing tests were carried out with a nickel compound as the braze material. The brazing set-up consisted of a Vycor tube, stoppered at each end and connected to a mechanical vacuum pump capable of pumping the system to approximately 1 micron. The braze material was applied as a powder to the top of the molybdenum cup and a porous plate (three-quarters of an inch in diameter) was placed over the drilled hole in the molybdenum cup. RF coils around the Vycor tube provided heating by induction. Power was applied slowly over a period of five to ten minutes until the nickel braze flowed, bonding the tungsten plate to the cup. In making the described brazes, three different thicknesses of porous tungsten plate were used (.030 in., .050., and 0.104 in.). The thin plates proved to be the most difficult, due to their tendency to crack, despite the fact that a very slow, controlled cooling cycle was applied over a period varying up to one hour. Another difficulty encountered was warpage in the tungsten plates, resulting in uneven brazing around the edges. In some cases at certain points the braze failed to join the two metals. The penetration however, was not excessive, and could be controlled by the quantity of braze material used. Figure VII-3 is a close-up view of the bonded plates (.030-inch-thick plate at top left, 0.050-inch-thick plate at lower right), showing the limited spread of the braze material into the emitter surface area.

The experimental bonding technique showed promise; therefore the next step was to use a higher temperature braze material. Nickel braze with a melting point of 1050°C would unduly limit the operating temperature of the emitter, as well as increase the possibility of emitter poisoning.

Molybdenum Braze: A commercial molybdenum-boron braze material was investigated next. The material was found to be very sensitive to surface cleanliness, and frequently did not flow readily. More important, however, was the possibility that the compound would poison the emitter. It was decided that

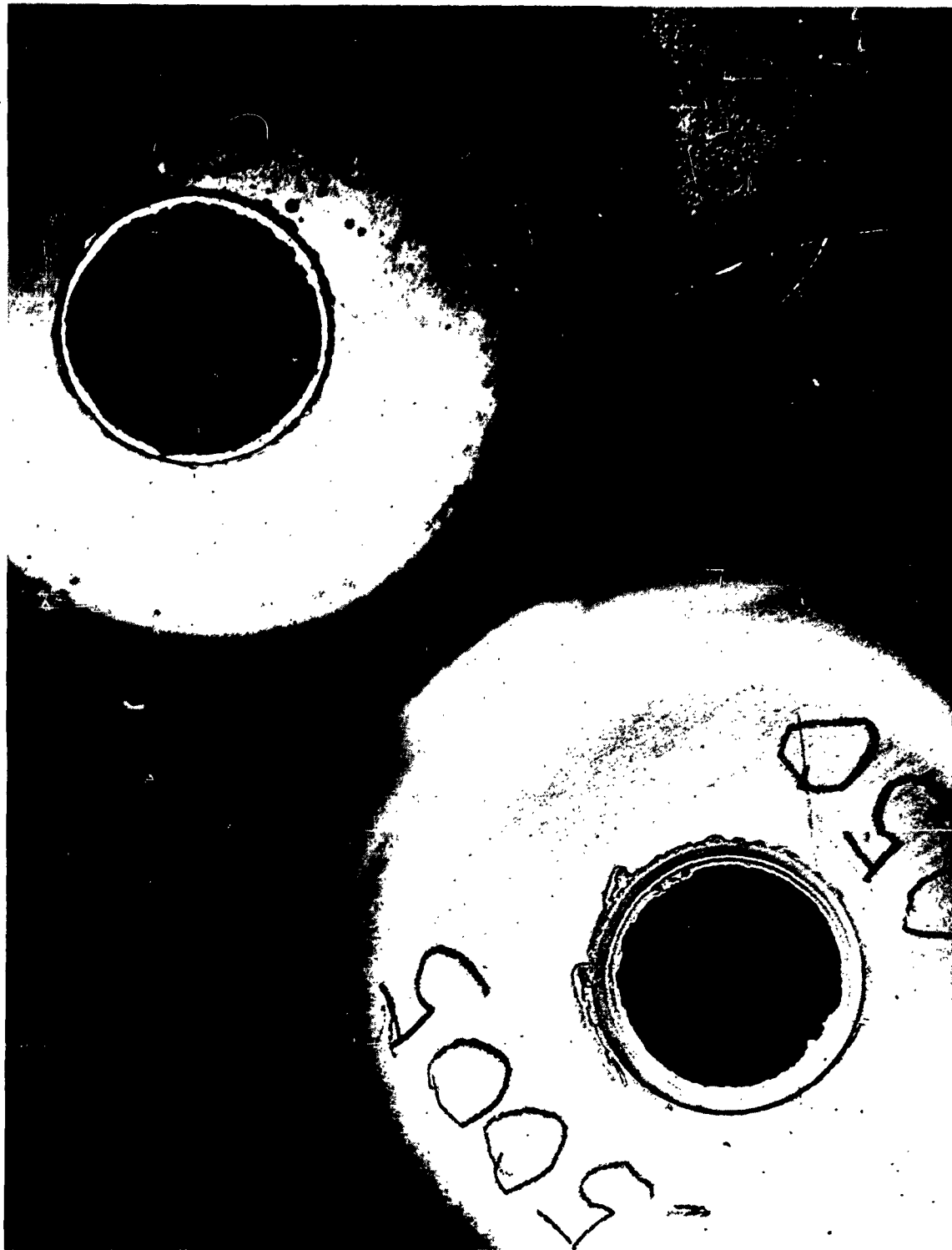


Figure VII-3. Nickel Brazed Porous Tungsten Plate

only pure metallic substances of high work function would be used for further bonding experiments; therefore platinum was investigated next.

Platinum Braze: The inductive heating set-up for platinum brazing is shown in Figure VII-4. Before heating, the complete assembly was purged with argon gas; the heating and braze operation was conducted under a hydrogen atmosphere. The brazing temperature was between 1775°C and 1800°C, at which point the platinum flowed freely. Figure VII-5 illustrates the first configuration of emitter tube which was fabricated and joined. Better results subsequently were obtained with a modified design.

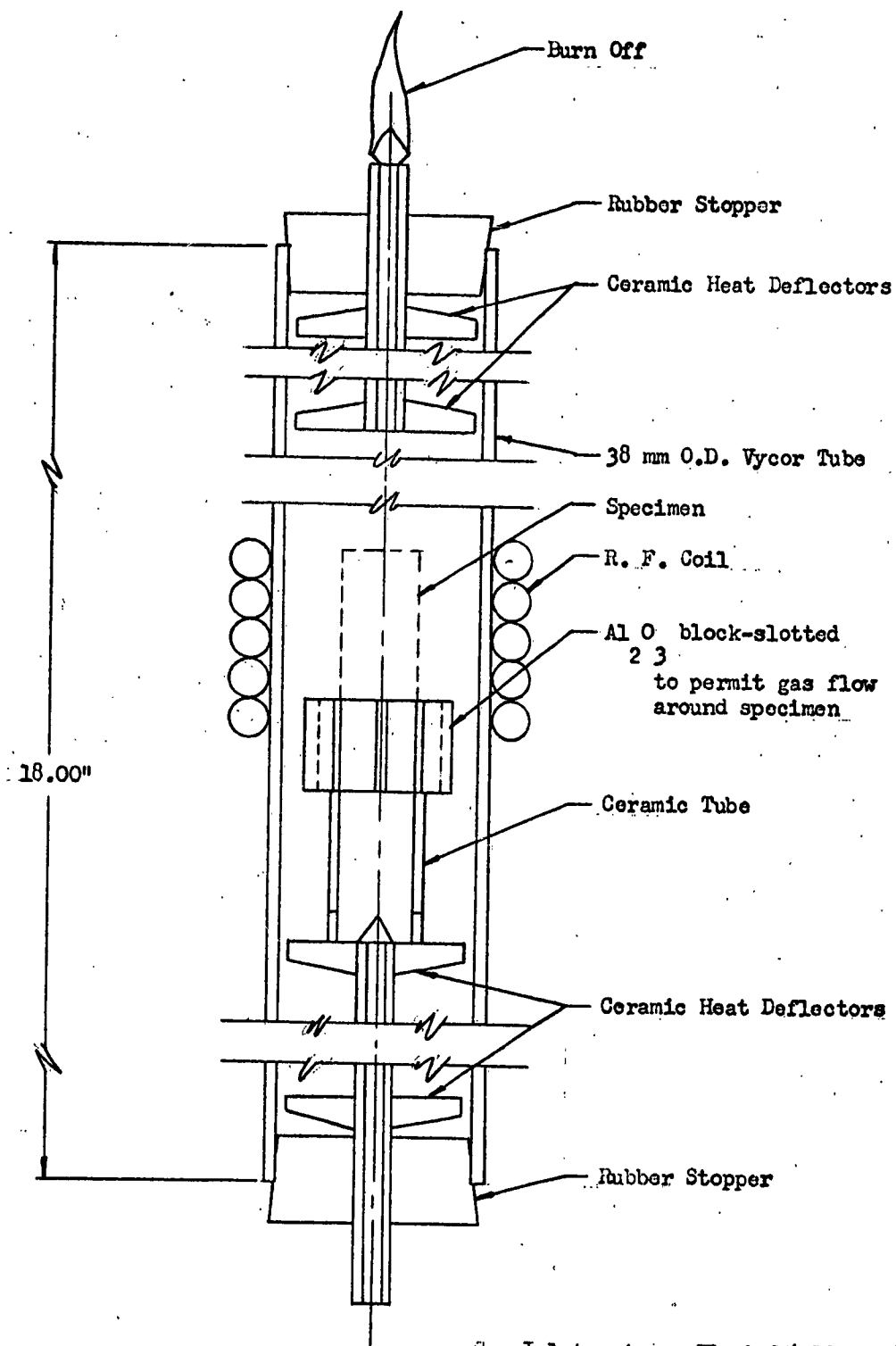
As can be seen from Figure VII-5, the porous tungsten plate was placed between two molybdenum washers. Great care was applied to making sure that the surfaces to be brazed were free from contamination by degreasing and cleaning. The platinum was applied as a thin foil, in the form of two "gaskets" on each side of the porous tungsten plate, and a thicker layer between the sides of the molybdenum washer, tungsten plate, and the sides of the molybdenum tube. After completing the braze, the specimen was subjected to a heat/cool re-cycling test in a hydrogen atmosphere to determine if the porous tungsten plate would crack due to differences in expansion rates, and also to determine if there would be further penetration of the brazing agent toward the center of the plate. After completion of five cycles up to 1600°C, both visual inspection and a pressure check revealed that the bond had been satisfactory. In order to measure the penetration of the platinum during the bonding process, the sample was sectioned and photomicrographed. This photomicrograph is reproduced as Figure VII-6 and shows that the bonding and the limitation of penetration were excellent. The section is taken at the edge of the plate, and includes the 0.030-inch-thick porous plate, washers, and tube. Penetration toward the center of the tube, past the inside diameter of the molybdenum washers, did not exceed the maximum penetration visible in Figure VII-6.

The molybdenum screen emitter described in Section III is bonded with platinum using a similar technique.

As a further step in brazing methods, a higher temperature bonding material could be used. Depending on the capability of the present RF furnace system to attain the required temperatures, niobium is being considered next as a brazing material.

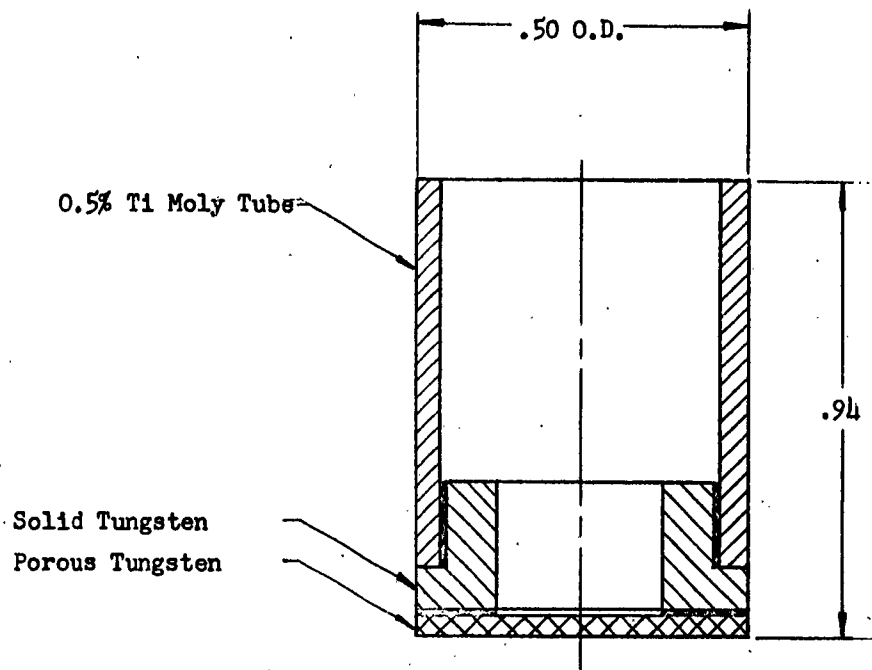
Ceramic Bond: In the early stages of the efforts to obtain a good bonding technique to hold the porous tungsten plates, it was readily apparent that if a bond of the tungsten to a non-inductive material such as glass or ceramic could be made, a reduction in RF heating power would be possible. The investigation was undertaken by an outside vendor who had considerable experience in prototype experimental work of this nature, primarily as applied to electronic tubes.

Glass, even in the Vycor ranges, was quickly ruled out due to the considerable differences in expansion rates from that of the porous tungsten. The choice was for a joint to be attempted between a high



Gas Inlet - Argon Flush 15 CFH
Hydrogen 8-10 CFH

Figure VII-4
TYPICAL BRAZING SET-UP



Black areas are Platinum Braze

Figure VII-5

FIRST PLATINUM BRAZE CONFIGURATION

- 116 -

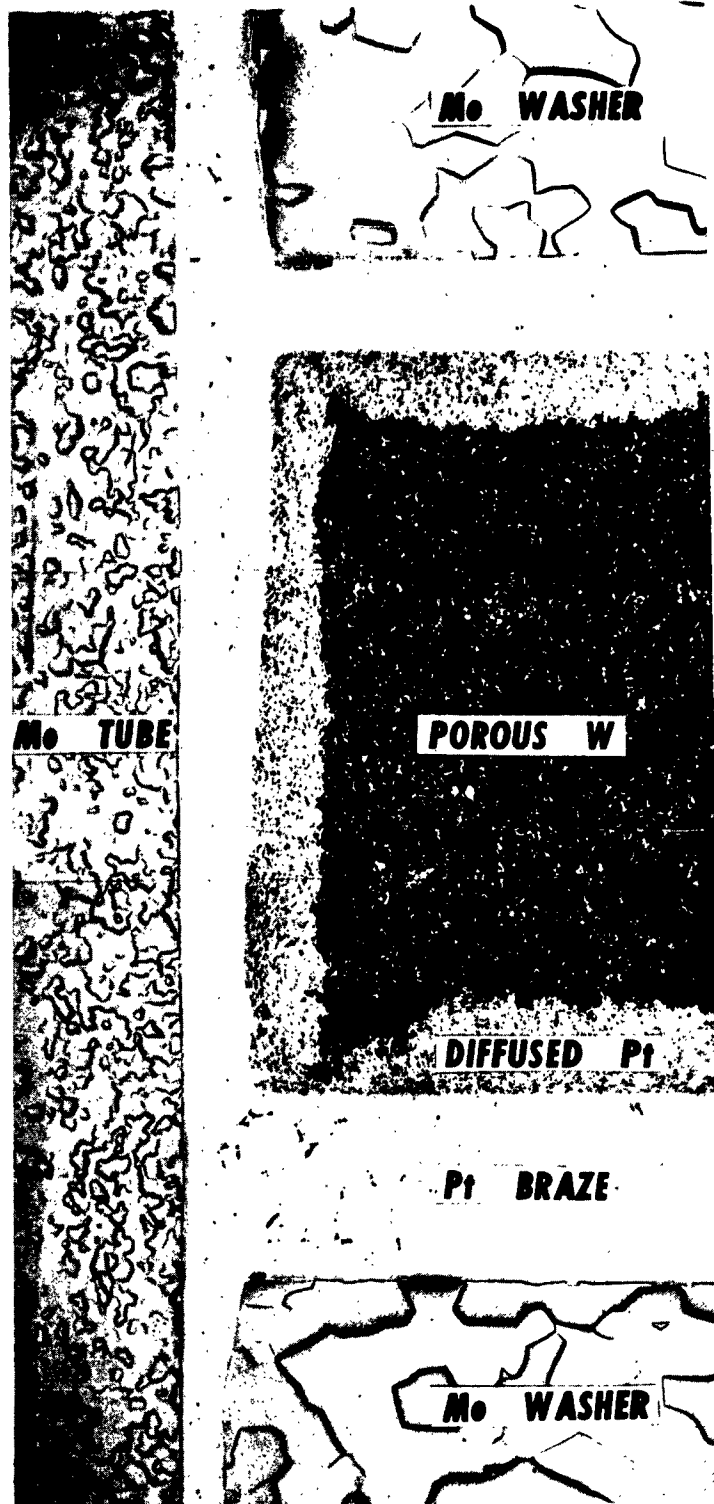


Figure VII-6. Cross-Section of Brazed Assembly

temperature ceramic with suitable expansion coefficient, and the porous tungsten emitter. A survey of the ceramic field yielded the result that a ceramic made by the Morganite Company, "Triangle H.5 - Mullite," might suit the purpose. The objective was to metallize the edge of a ceramic tube to which the porous plate would then be bonded. The specified softening point of the mullite was in the order of 1700°C. During the initial metallizing process, however, it became apparent that this specification was not correct; softening occurred at 1350 to 1400°C. Despite this restriction, a number of samples were successfully metallized with a molybdenum-manganese alloy in preparation for the braze. For the purpose of the braze, a gold-palladium alloy, Permabraz #201, was selected. The alloy liquifies at 1410°C and solidifies at 1380°C.

Brazing took place in an inert atmosphere of hydrogen using RF, with an inner block of carbon serving as the main brazing furnace. The complete assembly of ceramic and tungsten could be lifted or lowered in respect to the RF heating coils, as shown in Figure VII-7. Although care was taken to ensure that the assembly was brought slowly up to temperature and then slowly lowered, the thermal shock proved too great for the ceramic and immediate cracking occurred. In many of the ceramic samples it was found that frequently the ceramic itself contained faults and voids. It thus became quite apparent that little would be accomplished by the further use of this type ceramic.

Preliminary tests with the ceramic material "Diamonite" offered better promise of success. The material is an impervious alumina material with a softening point above 1650°C, and has been used successfully in high-power radio tubes where ceramic to metal bonding is required. Experiments on a ceramic bond, however, have been discontinued because of the inherent fragility, the possibility of emitter poisoning, and the better success obtained with the platinum braze.

C. Welding

One of the principal difficulties in welding a porous tungsten plate to a carrier tube is the extreme temperature distribution encountered in the welding operation itself. This sets up high thermal stresses within the porous tungsten which, in the majority of cases, cause failure of the tungsten even before the weld is completed. This is particularly true for plates of larger diameter, in the range of one-half inch and above, and for plates of large porous volume. As an initial experiment, a small disc of porous tungsten was welded to the top of a molybdenum cup under normal atmospheric conditions, using a heli-arc weld. As expected, some oxidation took place upon the tungsten surface and edge. The cracking effects previously mentioned occurred even before completion of the weld.

In order to reduce oxidation, a follow-up experiment was conducted by welding with a heli-arc electrode under vacuum conditions. A sketch of the apparatus is given as Figure VII-8. Due to the high temperature, the vacuum seal was not sufficient to enable the operator to successfully carry out the welding operation.

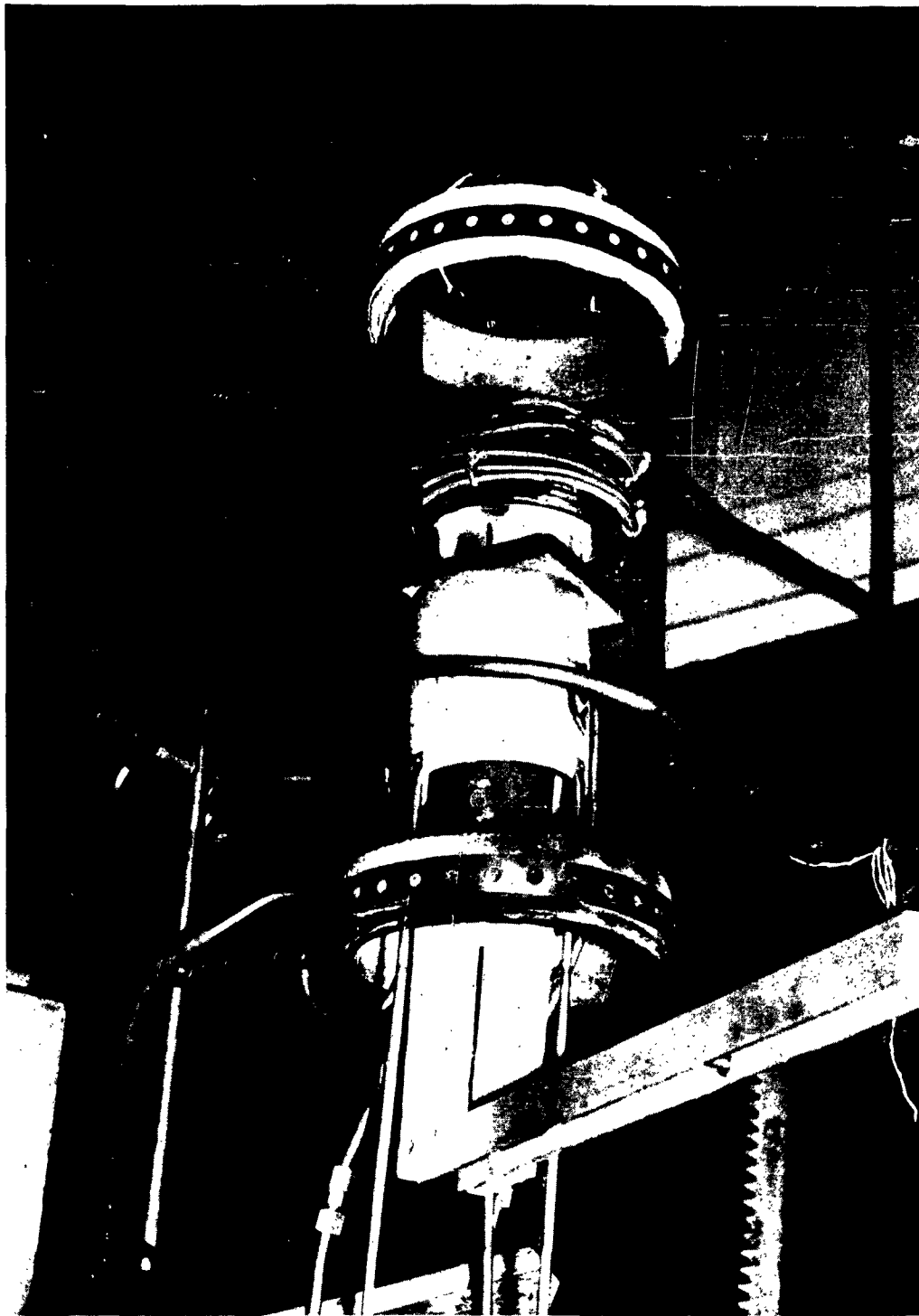


Figure VII-7. RF Heating Assembly for Joining Ceramic Tube to Porous Tungsten Plate

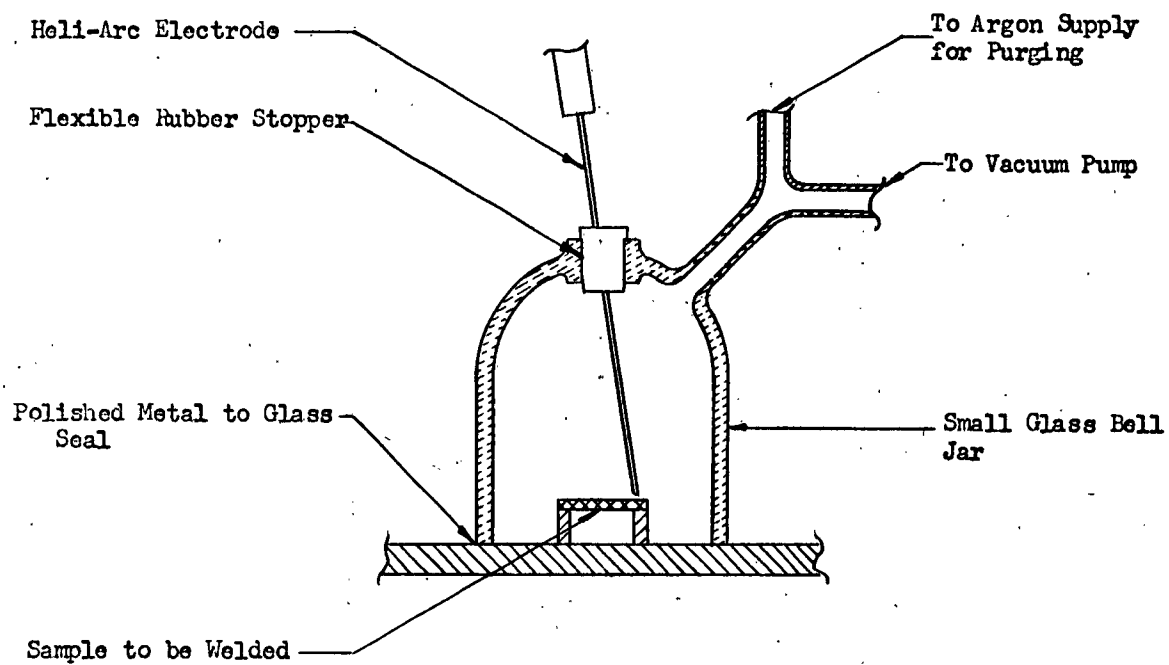


Figure VII-8
VACUUM ARC WELD APPARATUS

The design of a small welding rig recently has been completed which can be operated within the confines of a dry box containing an inert atmosphere such as argon. The welding electrode is held in a fixed position and the work piece can be rotated slowly at a predetermined speed. It is intended to investigate the welding of the porous plates (and the molybdenum screens) into a molybdenum holder, in order to fabricate a complete emitter assembly. However, the large thermal stresses during the welding operation are expected to continue to be the principal restriction to this method of bonding.

D. Sintering in Place

In order to eliminate the requirement for bonding, with the attendant difficulties described previously, a method is being investigated of sintering the porous tungsten emitter plate directly into the holder tube. To describe the technique briefly, a groove is machined on the inside wall of a tungsten tube, following which the tube is placed into a suitable die wherein tungsten powder is compacted and sintered to form a porous plate at the groove location. The fabrication technique is being investigated in conjunction with two outside refractory metal companies who have suitable facilities. One of the emitters is shown in Figure VII-9.

The technique is not sufficiently advanced to report complete success. In order to be acceptable, it was decided to subject the emitter assembly to five temperature cycling tests in which the temperature is raised rapidly to 1600°C, held for five minutes, and then removed. To date, shrinkage has been obtained in the porous plate with subsequent leakage around the edges. The bonding method, however, is being further investigated.



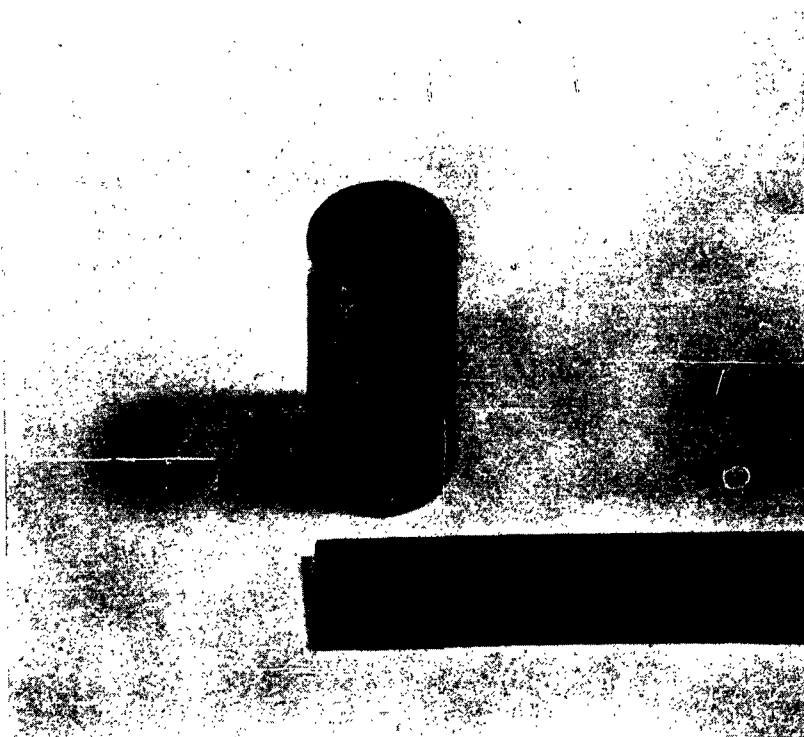


Figure VII-9. Porous Tungsten Plate Sintered
Directly into Tungsten Tube

VIII. CORROSION OF MATERIALS BY CESIUM

A. Introduction

One of the most significant problem areas in considering a cesium ion source is the compatibility with cesium of various structural materials including the ion source itself, insulators, electrodes, and conductors. Operating conditions include hundreds of hours at temperatures ranging from 500°K at the cesium boiler to above 1400°K at the emitter.

A literature survey failed to disclose information on the effect of cesium on various materials operating under conditions similar to those described above. A program, therefore, was undertaken to provide data which would be beneficial in the selection of materials to be used for construction of a cesium ion source.

The following sections include a discussion of the materials tested, the test methods, and the results. At the present time, two types of tests have been completed, with qualitative results obtained. The technique of testing has been improved; in the next test series quantitative data will be obtained.

B. Materials

The objective of corrosion testing is to screen various materials from a compatibility viewpoint, and ultimately to establish experimentally the best materials from a durability and fabrication viewpoint. Some of the materials of current interest include the following:

<u>EMITTER</u>	<u>INSULATOR</u>	<u>STRUCTURE (Including Electrical Conductors)</u>
Tungsten	Aluminum Oxide	Stainless Steel
Molybdenum	Boron Nitride	Nickel
Platinum	Borosilicate Glass	Copper
	Pyrex Glass	Aluminum

In the first test series, a larger number of materials than listed above were included, as described later under Results. The tests served to screen some of the materials; the most promising are being included in the next test series. The refractory metals such as tungsten, molybdenum, and platinum were selected because of their work functions for ionization purposes, as well as for their melting points, which are above the anticipated operating temperatures and, therefore, permit their use as structural materials. The metals may be used in the sintered porous condition, or as screens, for ionization



grids, and in solid form for structural members. Since the sintered form is composed of small particles, any detrimental effect which manifests itself at surfaces, such as corrosion, could seriously affect the strength of the grid component. Inter-granular attack in sintered joints would make the already brittleporous grid even more sensitive to thermal shock. It is essential, therefore, that the effect of cesium upon the refractory metals be accurately known for high temperatures and long time periods.

The stainless steels and nickel are applicable for use as structural materials in areas of moderate temperature and will be exposed to liquid cesium or cesium vapor. The use of such materials which will not be actively attacked by the cesium is desirable for long-term operation; proper selection must be made to prevent contamination of the vapor with corrosion products which could subsequently poison the emitter grid and, hence, reduce the ionization efficiency.

The materials being considered for electrical conductors include aluminum, copper, and platinum, and may in some areas be exposed to cesium vapor. Aluminum is also of interest for structural members because of its light weight. Both aluminum and copper, however, are susceptible to galvanic corrosion which, added to cesium corrosion, is an obvious detriment. The use of a corrosion resistant protective coating may be mandatory if the design requires the use of these materials.

Welded and brazed joints have always been a serious problem with systems which are to be associated with an alkali metal at high temperatures. A cracked weldment can easily render the ion source inoperative. Weldments and brazed joints are also particularly sensitive to intergranular corrosion in some cases even though the base metal appears to be unattacked.

The non-metals are required for use as electrical insulators; voltages in the kilovolt range are used for ion acceleration. Principal emphasis is on aluminum oxide as an electrical insulator.

C. Test Procedure

Two corrosion studies have been performed to date, using a glass container for the first test and a stainless steel container for the second. The selection of a glass system for the first corrosion container was made for the following reasons:

- (a) visual observation of cesium metal and specimen conditions, and
- (b) excellent vacuum tightness.

The limiting factor in the glass system is the melting point, and for this reason only low temperature (500°K) corrosion tests were performed.

For higher temperature corrosion tests, a stainless steel container was used to enclose the specimens, but this procedure had several drawbacks, namely:



CURTISS-WRIGHT CORPORATION • RESEARCH DIVISION

- (a) visual observation could not be made of the condition of the specimens and the presence of cesium, and
- (b) exact vacuum conditions at the operating temperature were difficult to determine.

In the high temperature test, several specimens were mounted in the same corrosion chamber in order to permit the testing of a larger number of samples. At the higher temperatures, a cross-contamination effect between samples was observed; therefore in the next test series the samples will be investigated on an individual basis.

The procedure for the tests was as follows. The various specimens, in the form of wire or rods, are mounted on a central holder. Figure VIII-1 illustrates the metallic samples mounted in a glass container for low temperature testing. A similar arrangement in stainless steel was used for the high temperature test. The glass well above the holder contains a thermocouple for internal temperature measurement during tests.

The complete apparatus for loading the glass container with cesium is shown in Figure VIII-2. The following loading and testing procedure was used for both the glass and the metal containers.

The liquid-nitrogen cold trap on the right of Figure VIII-2 is connected to the vacuum pump; the left cold trap is connected to an argon cylinder. The following steps are used for loading the specimen container with cesium.

- (a) The system is alternately flushed with argon and evacuated to remove oxygen.
- (b) At the last flushing, the argon side is sealed and the system is evacuated to approximately 10^{-6} mm Hg. During this step, the apparatus is heated externally until thoroughly outgassed.
- (c) The sample container is then charged with cesium metal (the cesium ampule is visible in the upper left leg of Figure VIII-2 directly above the container). Evacuation is continued to maintain a low pressure.
- (d) Finally, the container is closed by sealing the legs directly above the container. For the glass container, the sealing is accomplished by torch. In the case of the metallic container, the legs are soft nickel tubes which are forged with heat and pressure to provide a vacuum tight closure.

The evacuated sample container (with the sealed-in liquid cesium) is then placed into a controlled temperature furnace.

After exposure at a given temperature for a stipulated time, the samples are removed, weighed to determine weight change, and sectioned for metallographic examination.

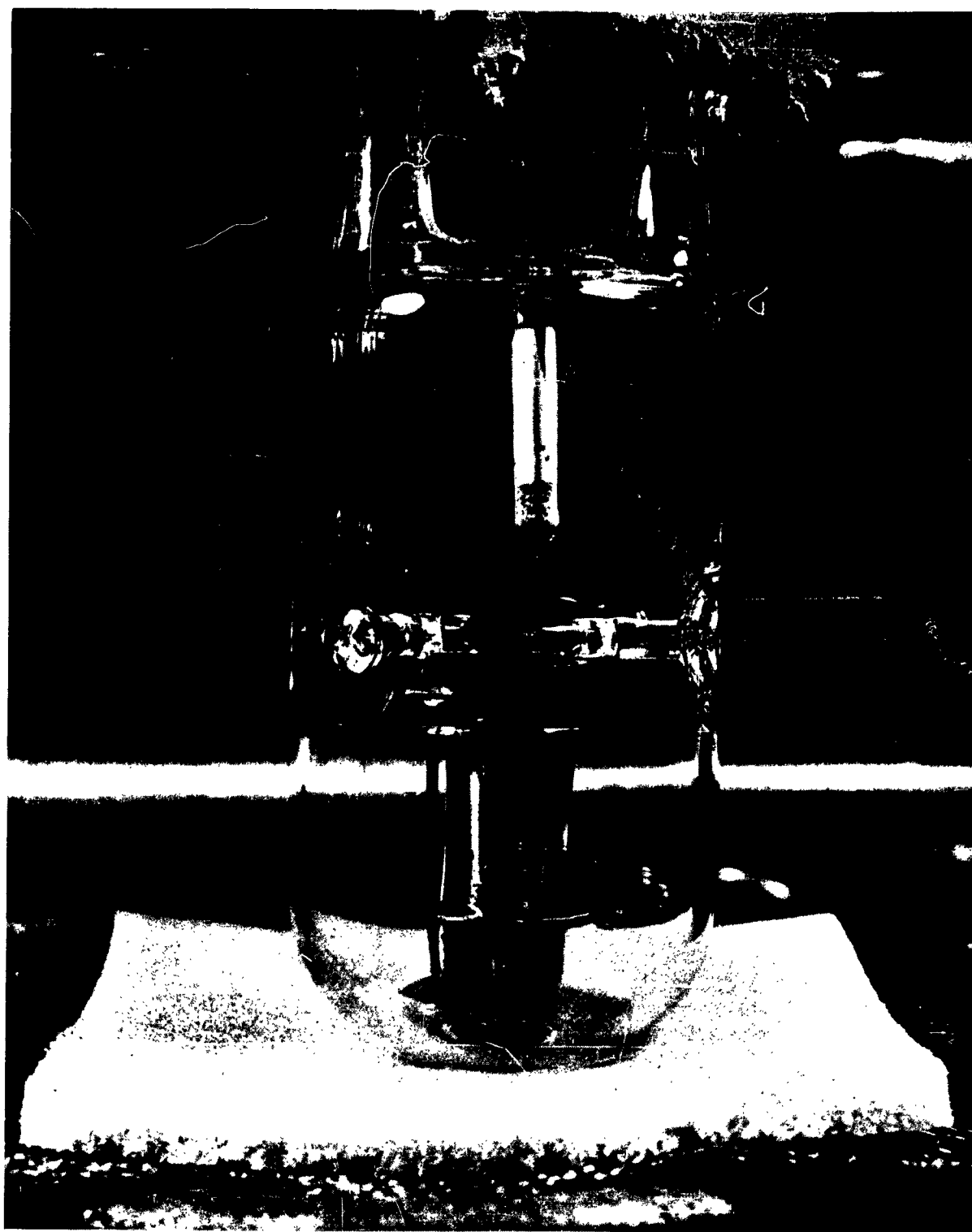


Figure VIII-1. Metallic Samples in Glass Vacuum Container

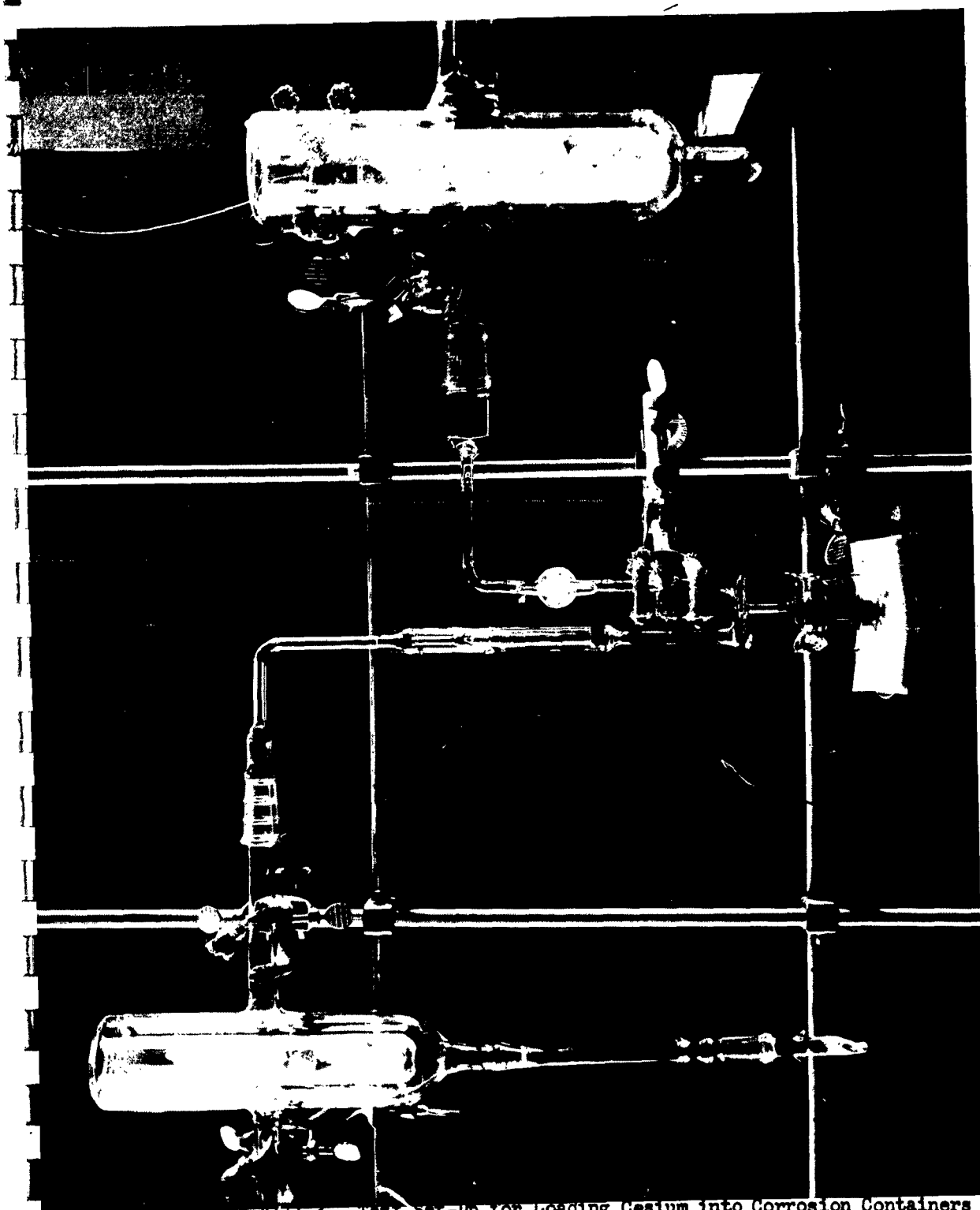


Figure VIII-2. Test Set-Up for Loading Cesium into Corrosion Containers

D. Results

The results of the tests at low temperature conditions are given for metals in TABLE VIII-A and for non-metals in TABLE VIII-B. Exposure was for 100 hours. Referring to TABLE VIII-A, nichrome, nickel, stainless steel, and tungsten were not greatly affected. The severe effect on aluminum is shown in Figure VIII-3. The effect of cesium on non-metals as shown in TABLE VIII-B, indicates that the glasses could suit as insulators, although the use of a ceramic such as aluminum oxide may be preferred from a structural consideration. The various other materials, such as teflon and rubber, were included as part of the original possibilities for system gasketing. Since that time the use of such materials has not been considered further for a long-life application. The results with non-metals, however, are of interest, although more tests would be required to confirm the data.

Certain metallic materials were next tested at a higher temperature for a longer period of time, using a stainless steel container as described previously. In some cases, as shown in TABLE VIII-C, the available samples were too small in diameter for good testing and could not be evaluated. Nevertheless, the results are of interest, and served as the screening test for the next series of corrosion experiments. The test results of TABLE VIII-C were further masked by various side-effects such as formation of low melting point alloys, high vapor pressure of some of the elements, and oxygen within the specimens. Since the specimens were in close proximity to each other, these effects obscured the effect of cesium on the individual materials. As described later, the next test series is on an individual basis, but the cross-contamination effect nevertheless can be a serious one in an ion source, and requires further investigation. After the most promising individual materials are selected from the results of the next test, it will be necessary to conduct a subsequent test using a technique similar to that of TABLE VIII-C, wherein cross-contamination effects in a cesium environment can be ascertained.

As an illustration of the results of the second corrosion test (Table VIII-C), photomicrographs of the more interesting materials are given in Figures VIII-4 through VIII-8.

All of the figures pertain to 450 hour exposure at 1275°K. Molybdenum, shown in Figure VIII-4, indicates no apparent change due to corrosion, but long time exposure at temperature has caused approximately fifty percent recrystallization. The effect on niobium is shown in Figure VIII-5. The dark gray area near the specimen edge is copper contamination. There is a distinct spongy effect caused by corrosion and alloying.

The result with Inconel X is given in Figure VIII-6. The corrosion attack on the surface and the spongy condition are apparent. The grey particles indicate a new phase.

TABLE VIII-A. EFFECT OF A CESIUM ATMOSPHERE ON VARIOUS METALS*

<u>Materials</u>	<u>Weight Change</u>	<u>Results of Surface and Photomicrographic Examination</u>
Nickel	0.10% loss	No apparent effect except loss of luster.
18/8 Stainless	0.25% loss	No apparent effect. Loss of luster and some surface staining.
Porous Sintered Tungsten	0.34% gain	Slight discoloration & staining.
Nichrome	0.12% loss	No apparent effect except loss of luster.
Mild Steel	0.04% loss	Some surface pitting.
Aluminum	0.76% loss	Localized erosion and corrosion. Metal removal and intergranular corrosion. Surface pitting.
Copper	2.10% loss	Small layer of scale on surface.
Silver Solder	0.32% loss	Slight surface pitting. Single phase layer at surface increased in thickness.
Brass	0.13% gain	Surface pitting.

* Conditions: 100 hours exposure at 575°K; vapor pressure 2mm Hg.



TABLE VIII-B. EFFECT OF CESIUM ATMOSPHERE ON VARIOUS NON-METALLIC MATERIALS
(Conditions 100 hr. exposure at 480°K)

<u>Material</u>	<u>Weight Change</u>	<u>Remarks</u>
Teflon	9.7% loss	Color change from white to black
Graphite-Teflon Compound	0.1% gain	Slight darkening from gray to black
Duroid	3.2% gain	Color change from buff to black
Rubber, Type 18007	1.1% loss	No apparent change
Rubber, Type 66-018	5.7% loss	Color change from green to green-white
Asbestos Cloth	15.7% loss	Color change from white to black
Al Oxide Insulator	2.6% gain	No apparent change
Nylon Cloth	27.8% loss	Color change from white to brown
Pyrex Glass	0.2% gain	No apparent change
Vycor Glass	8.9% loss	No apparent change. Weight change result appears to be questionable.
Tungsten Glass	0.2% loss	No apparent change
Soft Glass	0.1% loss	No apparent change
Natural Rubber	1.8% loss	No apparent change
Zr Oxide Ceramic	0.5% gain	No apparent change
Technical G Cement (Copper Base)		Reduced to copper. Disintegrated when tube opened to atmosphere.
Sauereisen Cement (Zirconium Oxide)		No apparent change in tube, but disintegrated when tube opened to atmosphere.

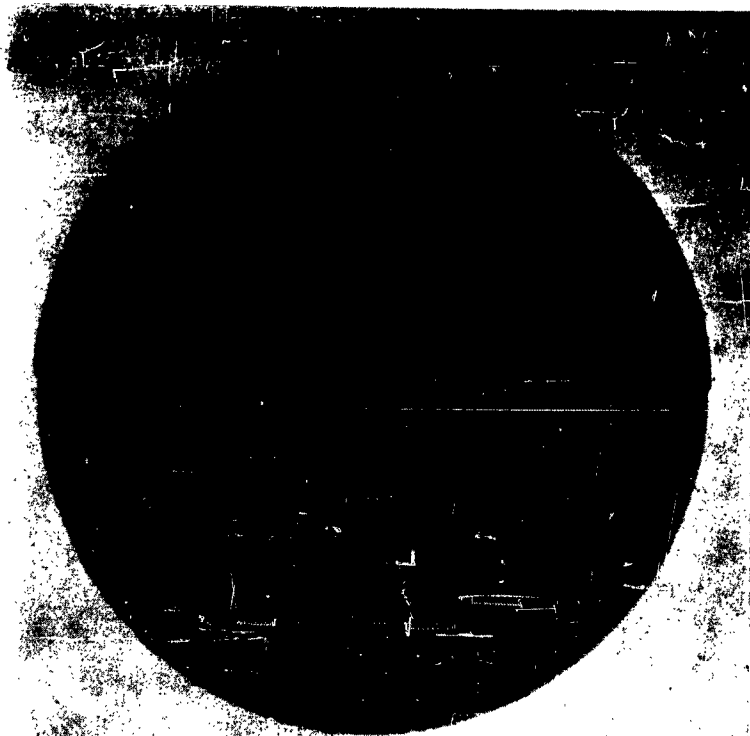


CURTISS-WRIGHT CORPORATION • RESEARCH DIVISION

TABLE VIII-C. SECOND CESIUM CORROSION TEST WITH METALS
(450 hours at 1275°K)

<u>Material</u>	<u>Sample Diameter (Inches)</u>	<u>Gram Wt. Before Test</u>	<u>Gram Wt. After Test</u>	<u>Gram Wt. After Wash and Dry</u>
Copper	.048	0.3333	Disappeared	
Gold	.030	0.2759	*	
Platinum	.032	0.3541	*	
Tungsten	.010	0.0370	*	
Niobium	.061	0.4491	.5194	.5188
Tantalum	.010	0.0242	*	
Molybdenum	.125	2.4031	2.4041	2.4039
Titanium	.030	0.0685	*	
Nickel	.062	0.5718	.5927	.5928
Inconel "X"	.062	0.5260	.5333	.5332
Stellite 25	.069	0.5299	.5295	.5296
Iron	.063	0.5259	.5259	.5257
Mild Steel	.093	1.0556	1.0579	1.0578
SS 308	.062	0.4781	.4802	.4801
SS 419	.198	3.2113	3.2120	3.2119
Iridium	.0605	0.1677	.2545	.2546

* Denotes samples which could not be evaluated due to small diameter.



Before



After

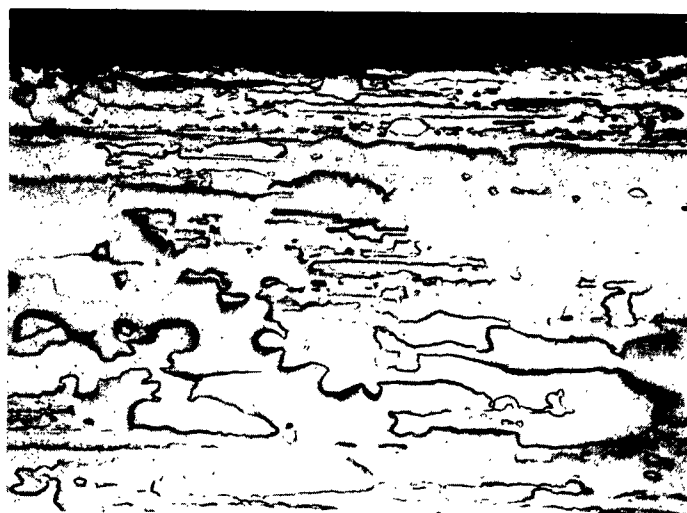
Figure VIII-3. Photomicrograph of Aluminum Sample Exposed to Cesium Vapor at 550°F for 100 Hours (500X)



M-877

(a) Before

250X



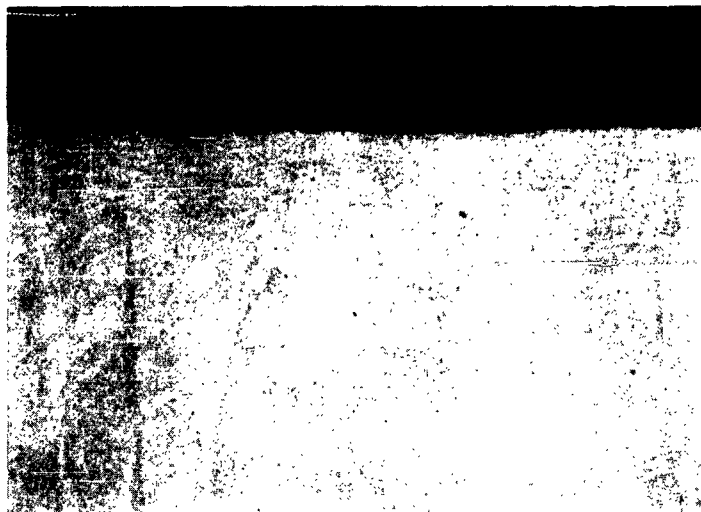
M-878

(b) After

250X

Molybdenum Before and After Cesium Corrosion Test

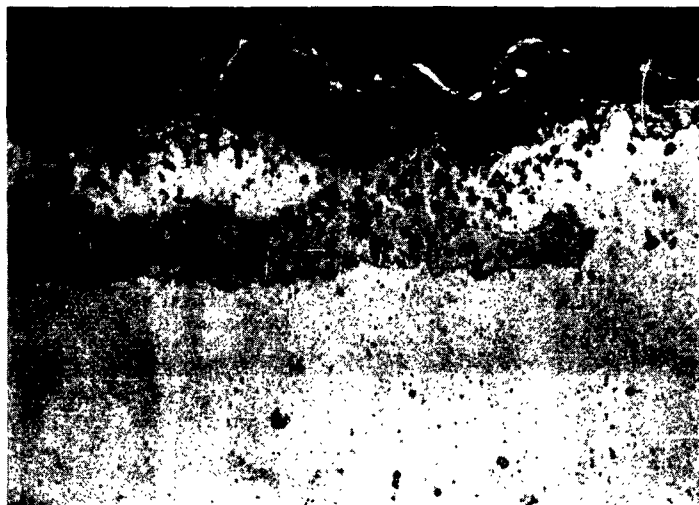
Figure VIII-4



M-861

(a) Before

250X



M-871

(b) After

250X

Niobium Before and After Cesium Corrosion Test

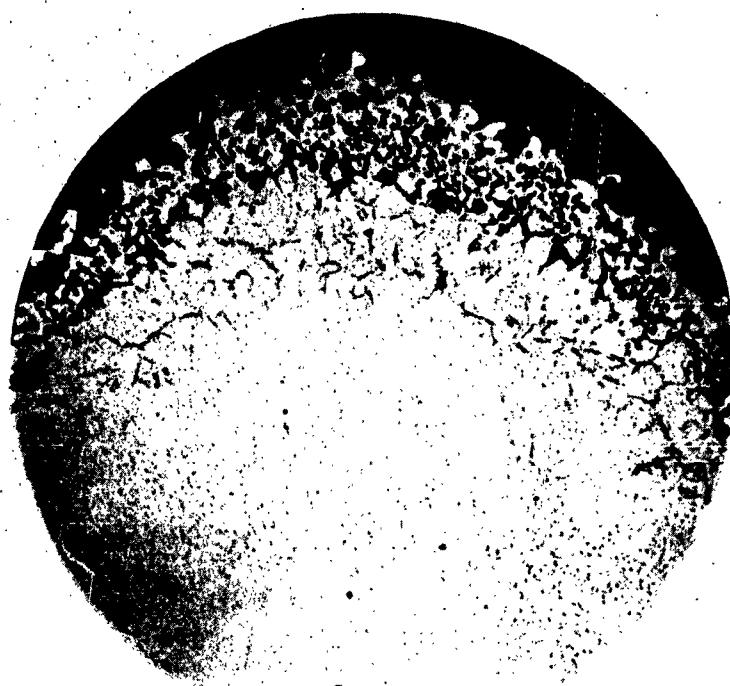
Figure VIII-5



M-883

(a) Untested, Etched

250X



M-857

(b) After Test

250X

Figure VIII-6

Inconel X Before and After Cesium Corrosion Test



M-882

(a) Before Test, Etched

250X



M-884

(b) After Test

250X

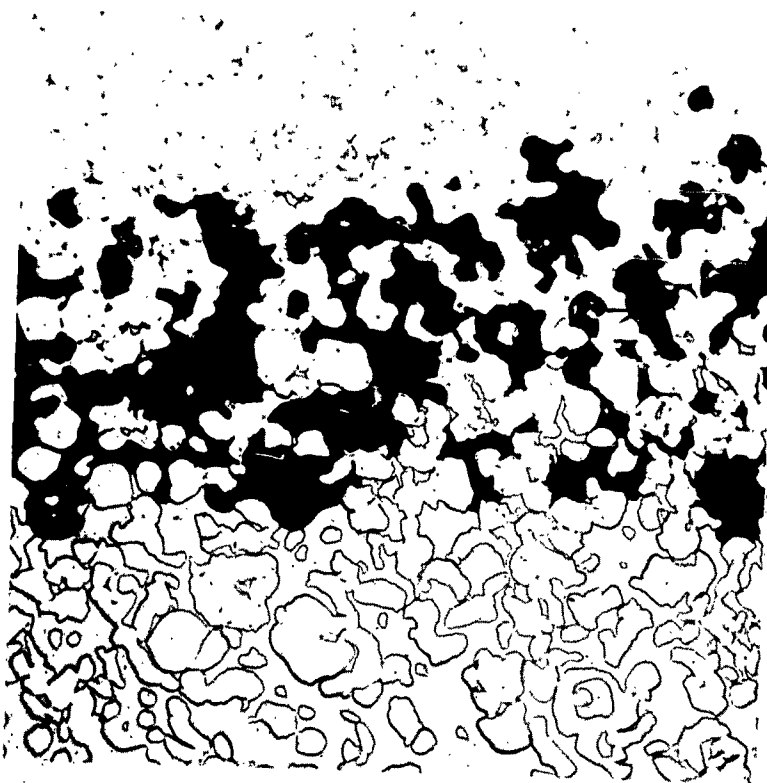
Stainless Steel 308 Before and After Cesium Corrosion Test

Figure VIII-7

M-861

(a) Before

250X



M-858

(b) After

300X



Iridium Before and After Cesium Corrosion Test

Figure VIII-8

For stainless steel (SS 308), the photomicrographs are reproduced in Figure VIII-7. The high carbon content in the untested specimen is indicated by the black spots. After testing, oxides are present at the surface and carbide is reprecipitated at the grain boundaries. These carbides will remain at grain boundaries through the 0000-1300°F range. At this temperature, this would cause the stainless to be subjected to increased intergranular corrosion in this area.

Perhaps the most dramatic result was obtained with iridium, as shown in Figure VIII-8. The black area indicates porosity, the darker gray areas are copper-gold alloying, and the light gray area is iridium.

E. Next Test Phase

Based on the previous test results, and considering the requirements for the ion source, the material chosen for further corrosion testing includes the following:

<u>EMITTERS</u>	<u>STRUCTURE</u>	<u>ELECTRICAL CONDUCTOR</u>	<u>INSULATOR</u>
Tungsten	Nickel	Copper	Aluminum Oxide
Molybdenum	Stainless Steel 410		
Platinum			

Copper doesn't appear to be particularly promising for the conductor (depending on the cesium environment) but platinum serves here as a possible back-up in the high-temperature applications. The method about to be described is relatively simple and is expected to provide the desired results. A greater cross-section of data than was previously available will be obtained.

Four specimens of each of the above materials have been prepared, cleaned, and accurately weighed. One sample has been mounted in a metallographic mount for study and photographing in the untested condition. The remaining three specimens have been loaded into clear fused quartz vials and temporarily sealed. Each of the vials will next be loaded with one-half grams of pure cesium metal and vacuum-sealed. The charged vials will then be divided into three groups for heating for a specified time and temperature. The vial will then be unloaded and the samples accurately weighed and measured, followed by photomicrographic examination.

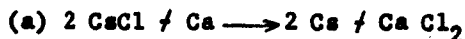
At the present time, the vials have been forwarded to a vendor for loading with cesium. Corrosion data will be reported after the vials are returned and the tests completed.

IX. CESIUM GENERATION IN SITU

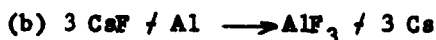
The use of cesium in its metallic form requires specialized handling techniques. The metal is shipped in glass ampules, usually sealed under a vacuum of about 10^{-3} mm Hg. For use in an ion source, it is necessary to thoroughly clean the ampule, place in the system, evacuate, then break the ampule and release the cesium metal under vacuum conditions. Although not particularly difficult, the procedure is somewhat time-consuming; but more important, the cesium must be handled with extreme care at all times. Cesium is extremely reactive in air, rapidly forming oxides and subsequently a hydroxide; with other substances, the reaction can be violent.

In order to reduce the handling problems with cesium metal, an experimental program is being undertaken to investigate the generation of cesium in situ. Various cesium salts, when properly mixed with a reductant and heated to a specified temperature, will release cesium as a product of the reaction. If the other products have a suitably low vapor pressure, the cesium metal produced in the ion source "boiler" subsequently could be used as required in the ion source without contaminating effects. An endothermic reaction may be preferable, with cesium generated as needed by controlling the temperature of the mixture.

Some of the reactions which appear to be feasible are given below. The reductions indicated are based upon the use of reductant weights twice the stoichiometric value.



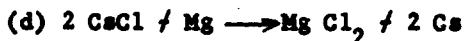
Reduction: 4 parts / 1 part \longrightarrow 3 parts Cs



Reduction: 8 parts / 1 part \longrightarrow 7 parts Cs



Reduction: 17 parts / 1 part \longrightarrow 7 parts



Reduction: 7 parts / 1 part \longrightarrow 6 parts Cs



Reduction: 3 parts / 1 part \longrightarrow 2 parts Cs



As a first step, reaction (a) is being investigated in a vacuum bell jar (Figure IX-1). The reactants are mixed to proper proportions, then are electrically heated in a crucible within the bell jar. The cesium is collected in a cold trap located above the crucible. Test will be reported after the experiments have been completed.



CURTISS-WRIGHT CORPORATION RESEARCH DIVISION

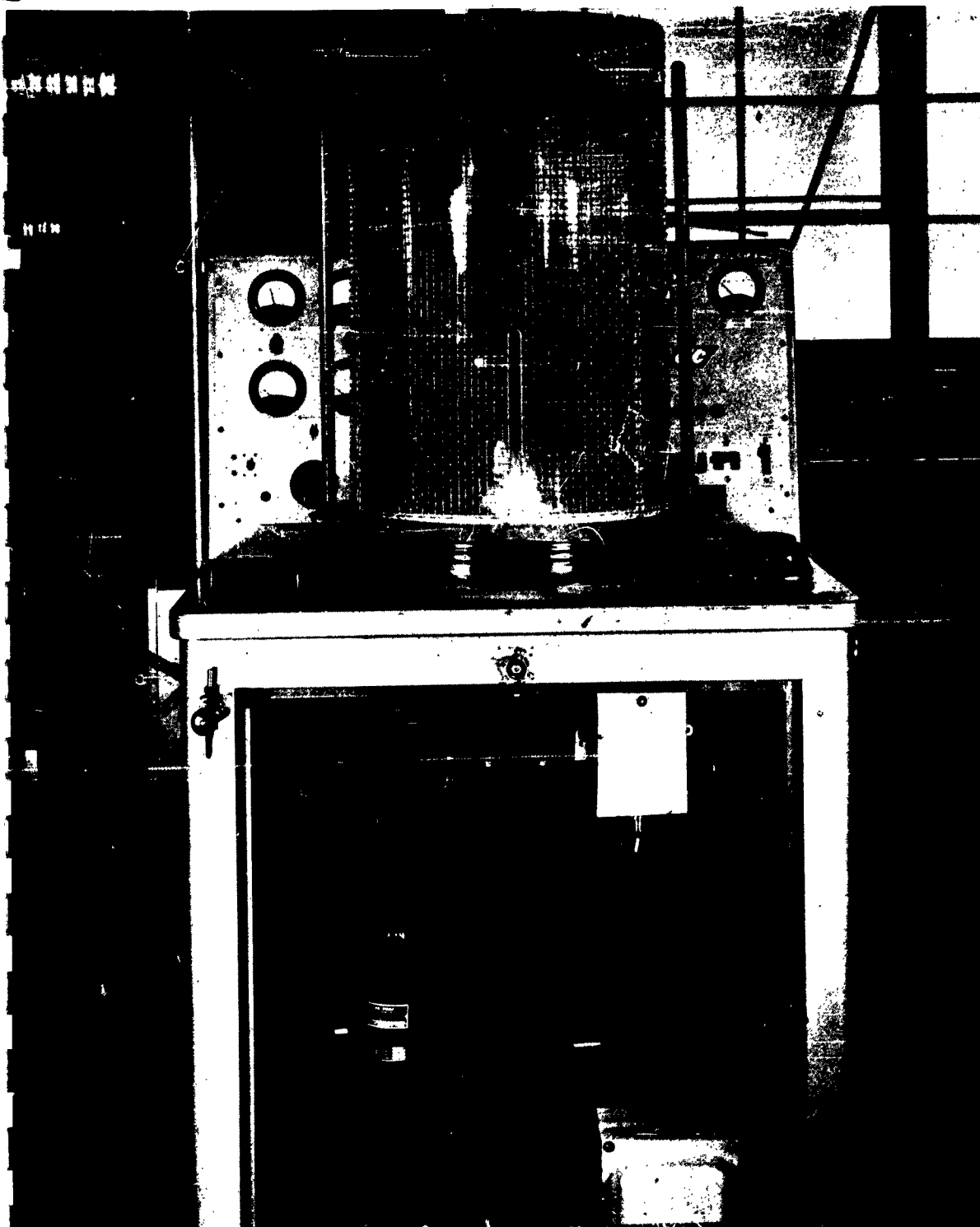


Figure IX-1. Vacuum System for Cesium Generator Experiments

X. THE RF ION SOURCE APPARATUS

A brief description of the RF ion source was presented previously in Section II-B of this report. Figure X-1 shows a hydrogen ion source which was set up prior to this program in the manner of Moak, et al. (l.c.), to confirm previously published results. In considering an RF source for alkali metals, a new design has been formulated, using in part the techniques described by Reifenschweiler (l.c.) and, in particular, the ion condenser described by Neuert (l.c.). The experimental device is shown in Figure X-2. The fuel is stored in the lower portion of the Pyrex plasma tube 8, separated by an aperture from the plasma tube. (The underlined numbers in the text correspond to the detail numbers shown in Figure X-2.) An external supply of hot air contained within the heat shields 7 and 11 regulates the fuel temperature and thus the vapor pressure in the plasma tube. The RF ionization coil 10 surrounds the tube and the heat shield. The ion-focusing electrode 16 and the extraction channel are located at the top of the plasma tube. Electrodes 16 and 20 form the ion condenser, the components of which are easily modified. The extraction channel is surrounded by a quartz tube 12, and is relatively large in diameter because with the low gas pressures the loss by diffusion is relatively small. The ratio of ions to neutrals should be correspondingly large. The accelerator electrode 20 is insulated by Pyrex 17 from the focusing electrode. The ion beam is collected in a Faraday cage contained within the cold trap 24. A grid 21 to suppress secondary electron emission from the Faraday cage is positioned between the accelerator electrode and the Faraday cage. The large elbow at the top of the apparatus is connected to the vacuum pumping system.

The apparatus is now being constructed, with all glass parts already completed. It should be noted that ion deflection in the ion lens is independent of the mass, therefore the same lens system can be used for various types of fuels.



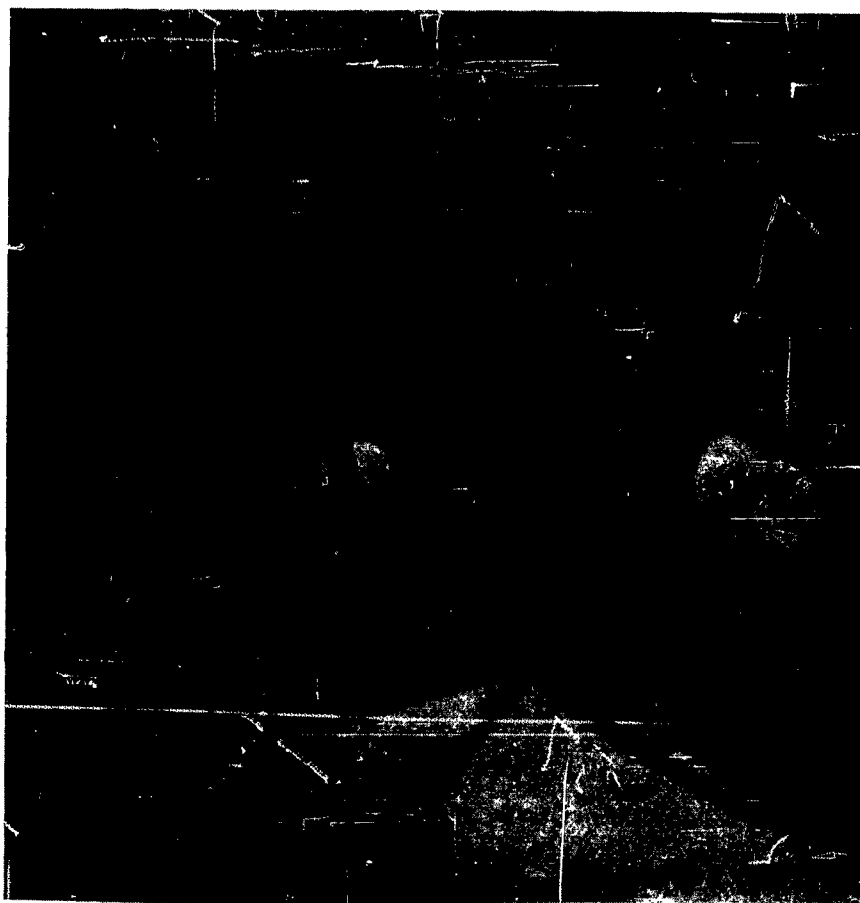
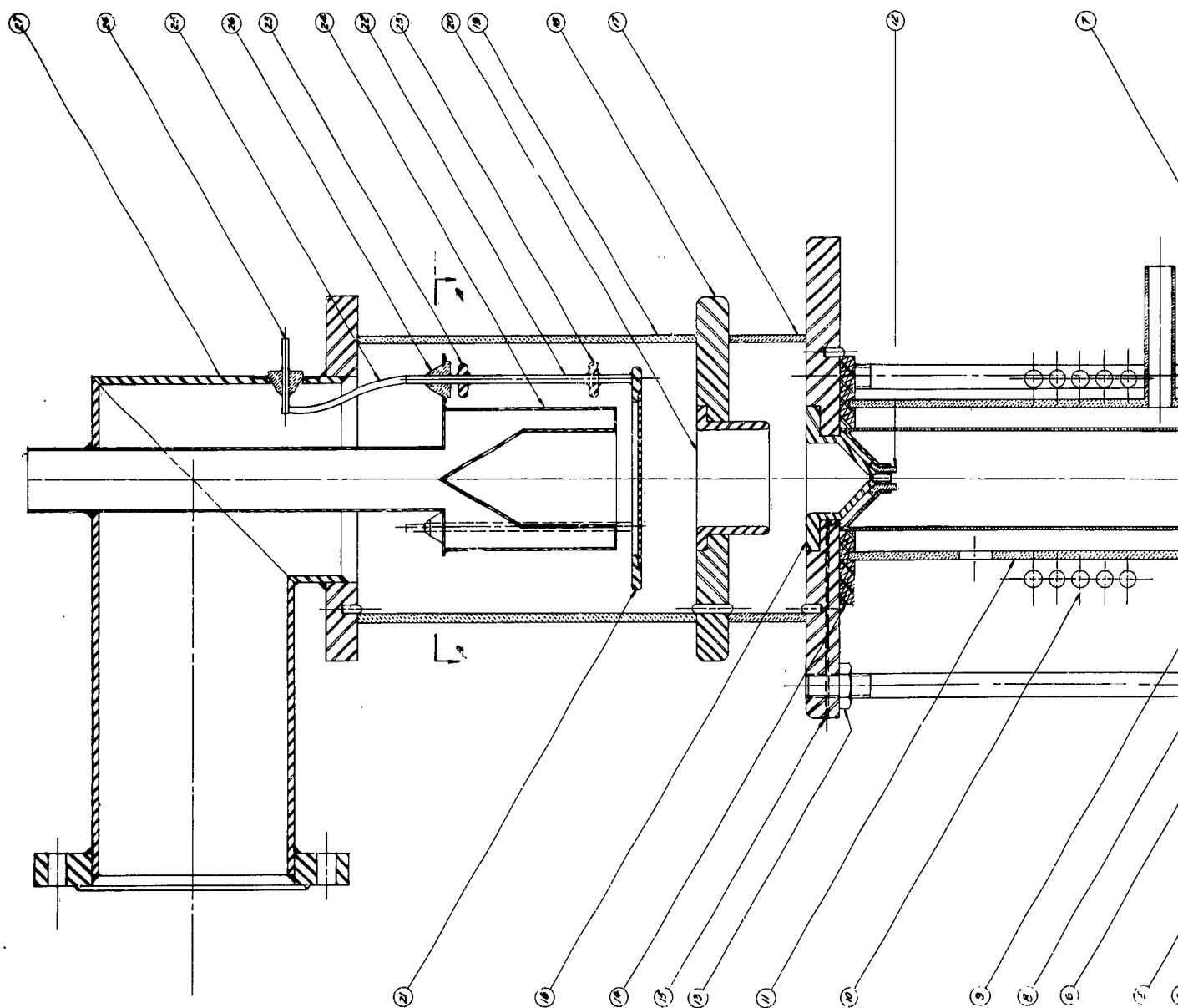
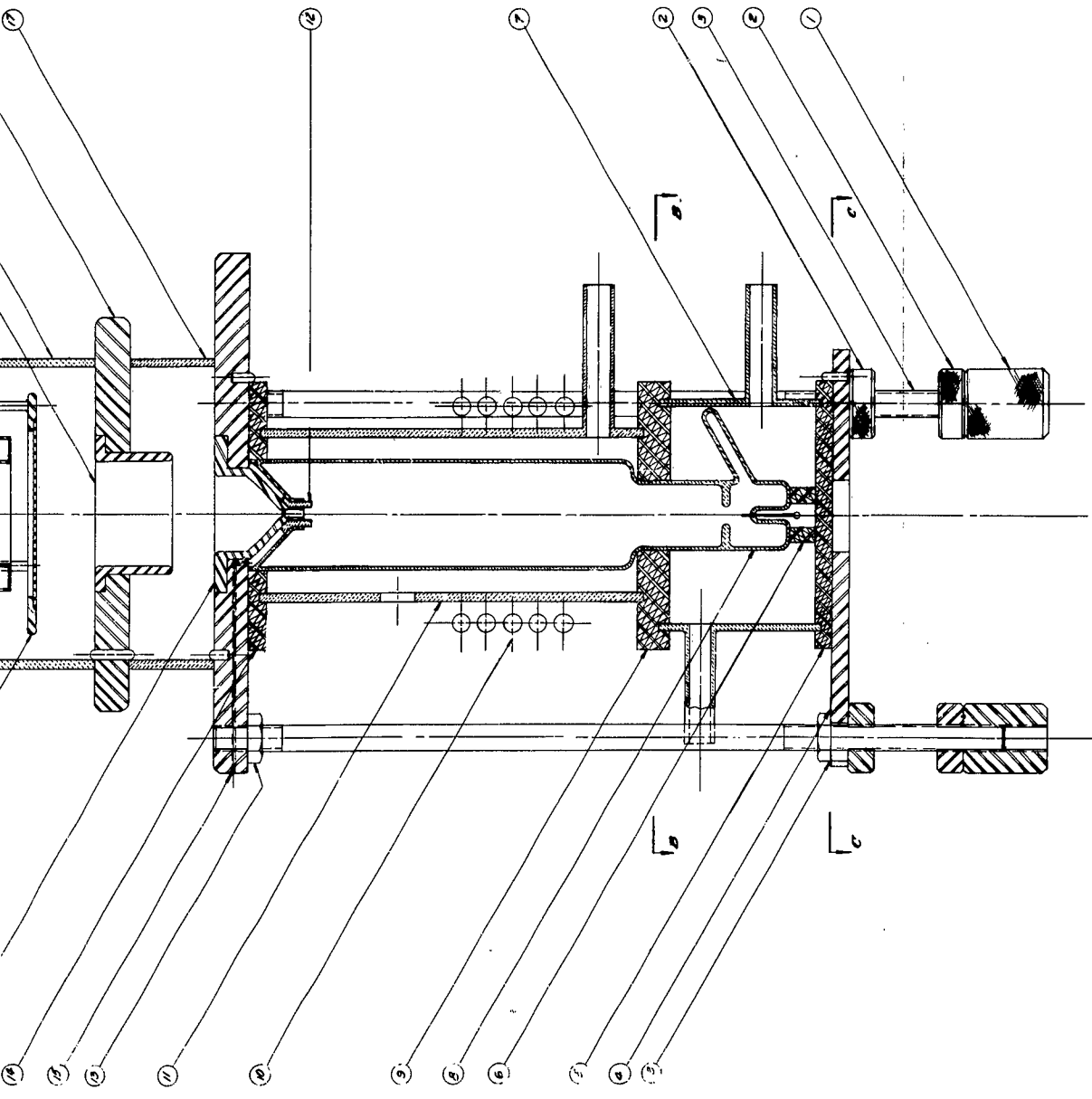


Figure X-1. RF Hydrogen Ion Source
in the Manner of Moak, et al.

1





RF ION SOURCE

Figure X-2

XI. THE PLASMA ARC SOURCE, PROPOSED EXPERIMENTS

In the original scope of work statement for this program, it had been proposed to conduct cesium-seeding experiments in the existing plasma-arc rig, with the objective of obtaining data for comparison with the charge exchange (contact) and RF ion sources. In Section II-C of the present report, the extensive efforts by AEC Laboratories on plasma sources has been discussed, and some of their results have been presented. In view of the difficult diagnostics problem and the questionable data which would be obtained using our existing rig, it was judged unwise to divert effort from our main problem (i.e., charge exchange ionization) to accomplish the plasma seeding experiments. For that reason the plasma work in this program has been devoted to a study of diagnostic techniques and of the specialized experimental devices which could provide acceptable data. The large current densities obtainable in plasma devices have already been cited in Section II-C, indicating that further experimental investigations on plasma sources would be warranted although not proposed in the present program.

A flexible experimental device would be of most value, since the various features suggested by existing arcs might be compared. A complete study is clearly a major undertaking, but it is recommended that the source be designed to allow for some changes in electrode geometry and magnetic field configuration. The following indicate the types of arcs considered in the order of their current interest.

- A. Thermionic or self-heated hollow cathode with mirror type fields and cathode extraction; high arc current.
- B. Source A modified for Duoplasmatron operation and anode extraction.
- C. Source A with uniform magnetic field and cyclotron extraction.

A. Diagnostics

The evaluation of an arc ion source and the extraction procedure should be carried out using known techniques in plasma study and ion optics. Particular attention should be given to comparing the results of operation with cesium vapor with the results of the charge exchange process using a hot tungsten plate. However, as mentioned before, an arc source might be expected to operate with practically the same efficiency using other elements (fuels) without the possible difficulties associated with the chemical activity of cesium.

A convenient and dependable plasma diagnostic to be used in studying the arc is optical spectroscopy. Provided the ion density exceeds



about $10^{16}/\text{cm}^3$, kinetic equilibrium can be assumed and the Saha equation, relating the ion and neutral densities with the "plasma temperature" is applicable (Ref. 54). The subject of spectroscopic diagnostics has been recently reviewed by Margenau and Lewis. The following equations have been taken from that review (Ref. 55). The Saha equation is written

$$\frac{n_i n_e}{n_o} = \frac{2 z_i}{z_o} \frac{(2\pi m_e kT)^{3/2}}{h^3} \exp - \frac{(X - \Delta X)}{kT} \quad (\text{Eq. XI-1})$$

where z_o and z_i are the partition functions for neutral atoms and ions and n_o and n_i for their concentrations. Since the Saha equation involves both temperature and electron density, it is desirable to get an independent measure of one of these quantities. Electron densities have classically been determined from the Stark profiles of hydrogen-like spectra. First-order Stark lines are generally used with conditions of rather high density ($10^{16}/\text{cm}^3$) in order to minimize other effects which complicate the theory. For the Balmer line H_β , Margenau writes (Ref. 56)

$$W_{1/2} \approx 7.8 r_2 (2n)^{2/3} \quad (\text{Eq. XI-2})$$

where $r_2 = 10.35$ for H_β .

Recent experimental studies have been made which utilized these and additional phenomena. In particular, Wulf has studied an arc discharge in helium using first and second order Stark effects and the Inglis-Teller "Drowning" of high energy states (Ref. 57). Davies has made a study of cesium discharges in a magnetic field (Ref. 58) making particular use of the distribution in intensity in the 6p recombination radiation as suggested by Moehler (Ref. 59) to determine the distribution of electron velocities in the discharge.

Absolute line intensities may also be used to obtain a relationship between radiator density and temperature provided the plasma is optically thin and the oscillator strengths, f , are known.

$$I = \frac{2\pi e^2 h f n^2}{m_e \lambda^3} n_o \exp - \left(\frac{E_n - E_o}{kT} \right) \quad (\text{Eq. XI-3})$$

A temperature can also be derived from the relative intensity of lines in a spectral series such as the Balmer series of hydrogen.

$$\frac{I_n}{I_{n'}} = \frac{n^2}{n'^2} = \frac{\nu_n}{\nu_{n'}} \frac{A_n}{A_{n'}} \exp \frac{E_{n'} - E_n}{kT} \quad (\text{Eq. XI-4})$$

The use of a small amount of hydrogen as a spectroscopic probe is desirable. However, transition probabilities for cesium are also known (Ref. 60).



CURTISS-WRIGHT CORPORATION • RESEARCH DIVISION

The Saha equation would be useful with the cesium spectrum or it might be applied to observations on the spectrum of helium or argon used as a carrier gas in the discharge. Argon would be of additional use since transition probabilities in A 1 and A 11 have recently been determined by Olsen (Ref. 61). Relative measurements on the Cs 1 and Cs 11 spectrum of interest can be made as a function of position in the arc and as a function of changes in applied voltage, rate of cesium injection, carrier gas pressure, etc. A particularly useful measurement which can be made when a small amount of cesium is added to a plasma of helium ions is the decrease of intensity of the helium ion light ($\lambda 4686 \text{ \AA}$). The measurement is directly related to the number of helium ions which must decrease as the electron density is increased by the ionization of cesium. This is because the Saha equation refers to the partial pressures of a given ion and all of the electrons. Incidentally, the Saha equation predicts that at a density of $10^{16}/\text{cm}^3$ and a temperature of 5000°K the cesium will be more than 90% ionized.

The use of a Langmuir probe is also a standard technique in dense plasmas. Several circumstances indicate, however, that this diagnostic may be somewhat unreliable. There is always some effect of a probe on the behavior of the discharge, and its use in a magnetic field is more difficult to interpret. Finally, the bombardment by cesium neutrals may give rise to spurious currents requiring corrections. In view of the precautionary remarks expressed by Loeb (Ref. 62) and by Francis (Ref. 63), it does not seem advisable to depend entirely on probe measurements, although some use should be made of this technique. Following the notation of Bohm, Burhop, and Massey, the expressions of electron temperature T_e and positive ion density n_0 are:

$$T_e = \left[\frac{d}{dV} \ln (-J - J_s) \right]^{-1} \quad (\text{Eq. XI-5})$$

$$J_s = 0.4 n_0 \sqrt{\frac{2 k T_e}{m_i}} A \quad (\text{Eq. XI-6})$$

where J_s is the ion saturation current, V is the probe voltage, and A is the probe area. The validity of the expression for T_e in a magnetic field is somewhat questionable, but the ion saturation current is expected to be a good diagnostic if the probe dimensions are small compared to the Larmor radius for the ions.

Microwave techniques appear not to be applicable to the dense plasmas obtained in arc discharges. However, similar optical refractivity measurements have been suggested by Alpher and White for electric discharges (Ref. 64). In any major plasma study such a possibility should be exploited. However, the optical problems involved with this diagnostic are sufficient to postpone its use for the immediate future.



B. Ion Extraction

The success of any ion source, regardless of its production of large ion densities, hinges on the ability to extract large ion currents. A straightforward testing procedure here is the collection of the ions in a Faraday cage after extraction and analyzing magnetically in a manner similar to that accomplished in the previously discussed charge exchange experiment. A particular difficulty to be avoided in the extraction procedure is the production of electrons and possibly a plasma in the accelerating region. It is expected that the electrons, but probably not the negative ions, can be magnetically deflected from the accelerating field. It may thus develop that an upper limit on the escape of neutrals from the source must be imposed in order to guarantee the success of ion extraction.

Those devices relying on an accelerating grid may be experimentally of interest, but will probably have to be ruled out on the basis of long term reliability. The filament type cathode suggested in Source A may suffer in this regard also. However, the use of D.C. filament power may prevent a considerable amount of sputtering due to the azimuthal magnetic field produced about each conductor. Also, the alignment of the filaments parallel to the exterior magnetic field should eliminate the usual sagging of such a filament. The particular merit of this type of cathode is based on the supposition that an independently heated cathode will produce a more stable arc, and that a larger ion current may result from the ion backstreaming caused by the existence in the plasma of a fraction of the impressed arc field. This accelerates the ions toward the cathode sheath from a region which is space-charge-neutralized.

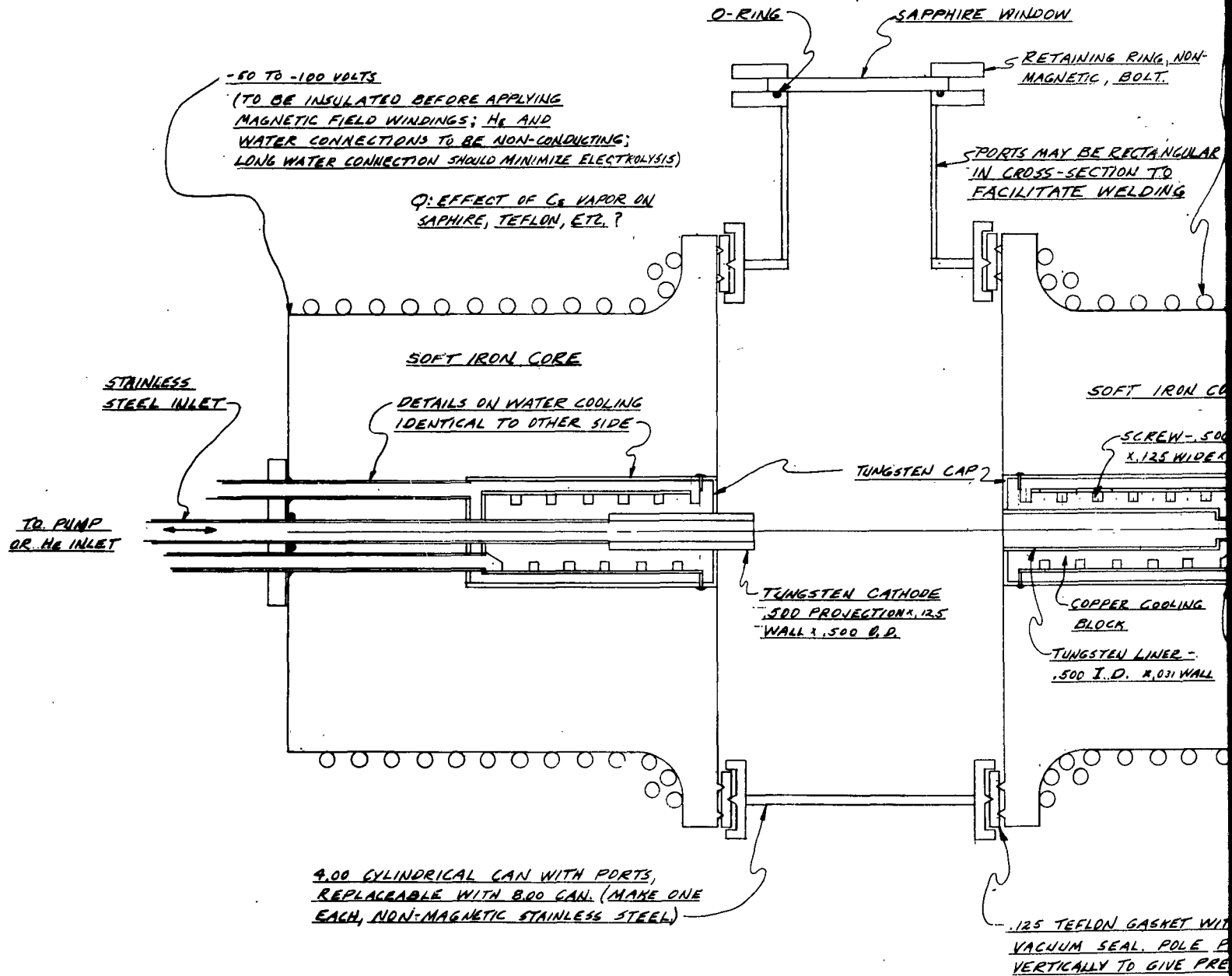
A final possibility for ion extraction and acceleration is the classic cyclotron resonance phenomenon for single ions. The sketch of a suggested apparatus is shown in Figure XI-1. Such a process lends itself nicely to the selective acceleration of a particular type of ion in a magnetic field. It is expected that an electric field oscillating at the cyclotron frequency for cesium ions (about 50 kc for 5000 gauss) and directed at right angles to the magnetic field can penetrate the plasma sufficiently to extract a small fraction of cesium ions present in a plasma of another carrier gas. After being removed from the plasma column and its partial shielding effect, the ions will be less subject to recombination and can be given further energy for propulsion purposes by continued cyclotron acceleration, which is possible if the region is a reasonably high vacuum. This is also one of the attractive features of the DCX type arc. It is clear that the accelerating frequency ought to be comparable to or greater than the collision frequency of the ions. The latter may be estimated from the expression derived by Spitzer (Ref. 65). The frequency of 50 kc corresponds to a density of $10^{12}/\text{cm}^3$, roughly comparable to that surrounding the DCX arc. The period of oscillation will have to be somewhat less than the



CURTISS-WRIGHT CORPORATION • RESEARCH DIVISION

FOUR EXPERIMENTAL PORTS AT 90°
 1. WINDOW
 1. PUMP
 2. CYCLOT RESONANCE GEARS
 OR PROBES
 OR ADDITIONAL WINDOWS

1



FOUR EXPERIMENTAL PORTS AT 90°
 1. WINDOW
 2. PUMP
 3. CYCLOT. RESONANCE GEARS
 OR PROBES
 OR ADDITIONAL WINDOWS

2

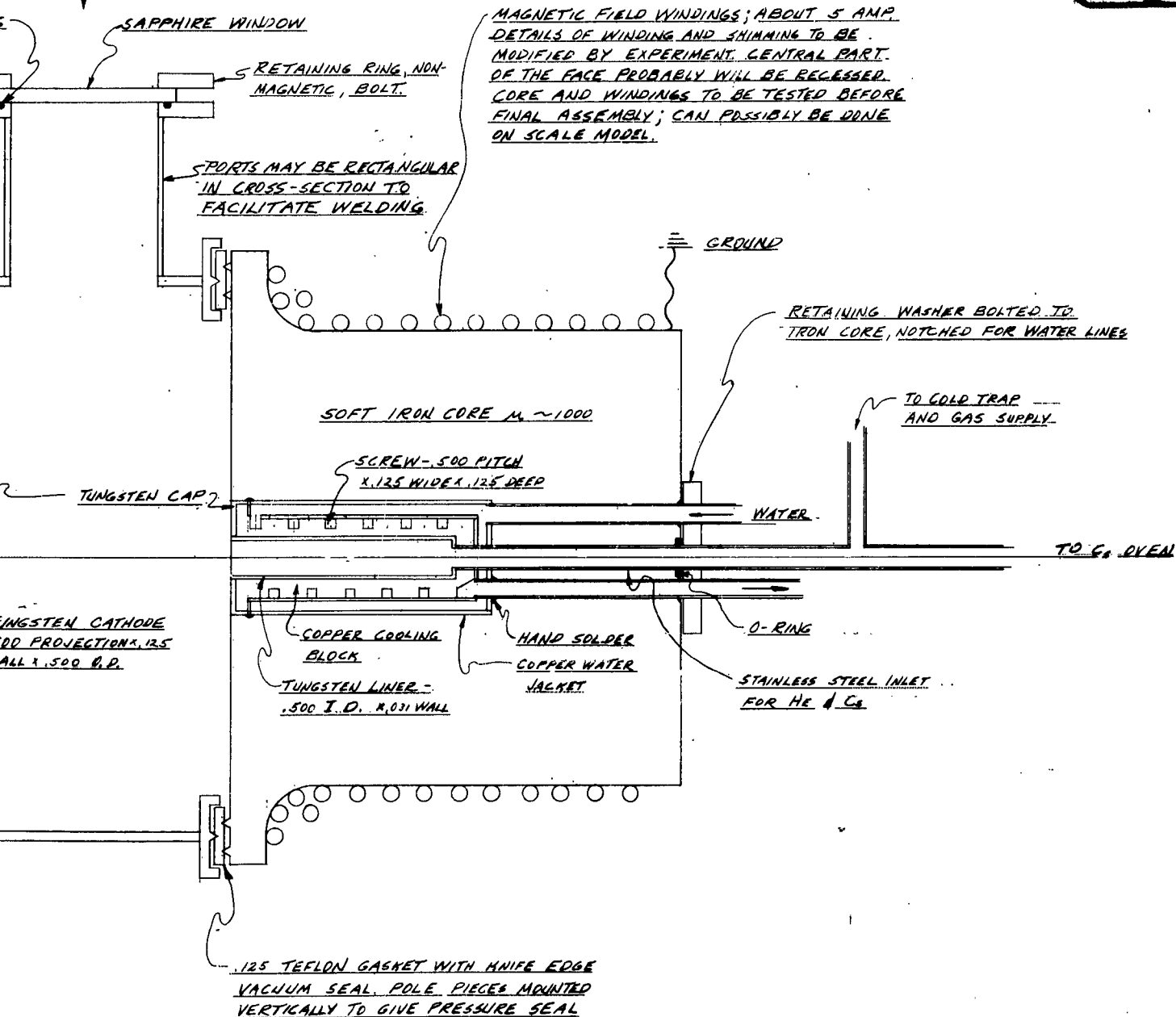


Figure XI-1. Magnetically Constricted Plasma-Arc

transit time in the arc if several accelerations are to be made, which may require an arc on the order of one meter in length. Also, a 10 kev cesium ion in a magnetic field of 5000 gauss would travel in a 30 cm radius arc. Apparently, this would be a rather large device, although the magnetic field and frequency can be increased somewhat in order to decrease the space required. There will undoubtedly be considerable power transferred to the plasma electrons by the cyclotron acceleration field and the possibility of extracting a large ion current may be rather remote. The unique feature allowing very large final ion velocities using relatively small accelerating fields is believed to merit further theoretical and possibly experimental study, although no further studies are anticipated in the present programs.



XII. CONCLUSION AND RECOMMENDATIONS

Based upon the results of the program to date, i.e., at the conclusion of ten months of work, several significant experimental observations have been made, and specialized techniques have been developed with regard to ion source configuration, performance, and operation. The results are not yet complete, and will be reported in their entirety in the final contract report. On a preliminary basis, however, the following observations can be made.

- (a) The charge exchange (contact) emitter can provide a high current density on a theoretical basis. Diffusion experiments with various gases tend to confirm that emitters can be designed for high current densities.
- (b) The RF method of ionization also is promising; an experimental apparatus has been designed and partially fabricated.
- (c) Diffusion flow experiments with contact emitters confirm that the flow rate is a function of plate temperature and differential pressure. Furthermore, an aging effect is observed in porous plates which reduces the flow rate with time. The aging effect may be a function of sintering temperature.
- (d) By-passing of fuel flow around the edge of the emitter can reduce the ionization efficiency. Various methods of bonding the emitter have been investigated. A braze method of holding the emitter has been successful for diffusion experiments, but requires further confirmation in ionization tests.
- (e) During the experimental investigation, it was noted that the beam current data did not always follow the three-halves law, which may have been due to secondary emission under certain operating conditions. The effect of secondary emission is being further investigated. Another measuring technique is the use of a mass spectrometer, which has been designed and is being constructed. The equipment is intended to eliminate, in addition to other effects, the effect of secondary electrons.
- (f) Corrosion of materials by cesium is apparent at high temperatures when exposed for extended periods of time. In particular, cross-contamination by different materials in the ion source system can provide additional corrosion. The data is not complete; confirming data for individual samples at high temperatures will be obtained.

Firm and final recommendations cannot be made until all of the experimental results are available at the conclusion of the present program period. It is intended, however, to concentrate during the



remaining contract period on the following phases.

- (a) Repeat all diffusion experiments using the braze method of bonding the emitters.
- (b) Measure the beam current density of the various emitters in the ion gun. Continue the assembly and check-out of the mass spectrometer.
- (c) Continue with the "sintered in place" porous tungsten plate emitters as a means of obtaining a well-bonded emitter.
- (d) Perform cesium corrosion experiments with individual samples at high temperatures for extended periods of time.
- (e) Continue, on a limited basis, the emitter plate heating investigation, the RF apparatus construction, and the generation of cesium fuel in situ.



CURTISS-WRIGHT CORPORATION • RESEARCH DIVISION

REFERENCES

1. "Supplemental Information for Proposed Joint ARPA-ONR Program on Compact Charge-Exchange Ionization." CW Research Division Report submitted to ONR, Power Branch.
2. A. Eucken, Lehrbuch der Chemischen Physik Volume II, 2. p1320. 1944.
3. J. Zemel, J. Chem. Phys. 28. 410. 1958.
4. S. Datz and E. H. Taylor, J. Chem. Phys. 25. 389. 1956 and J. Chem. Phys. 23. 1711. 1955.
5. T. J. Killian, Phys. Rev. 27. 578. 1926.
6. J. B. Taylor and I. Langmuir, Phys. Rev. 44. 423. 1933.
7. M. J. Copley and T. E. Phipps, Phys. Rev. 48. 960. 1935.
8. P. Keuk and L. B. Loeb, Rev. Sci. Instr. 4. 486-490. 1933.
9. J. B. Taylor and I. Langmuir, Phys. Rev. 51. 753. 1937.
10. M. Nordmeyer, Ann. d. Phys. 16. 697. 1933.
11. J. B. Koch, Z.f. Phys. 100. 669. 1936.
12. E. Stuhlinger, "Electrical Propulsion Systems for Space Ships with Nuclear Power Source." J. Astronautics, 1955. 149-152 and 11-14. 1956.
13. M. J. Willinsky and E. C. Orr, "Project Snoopers," ARS Preprint 419-57. April 1957.
14. D. B. Langmuir, Feb. 17, 1958, ERL-116, ERL-119 and ERL-121.
15. R. H. Boden, R 1455, May 1955, R-645.
16. A. T. Forrester and R. C. Speiser, Conference on Ion and Plasma Research, 30 September - 2 October 1958.
17. F. L. Hughes, H. Levinstein, and R. Kaplan, Phys. Rev. 113. 1023. 1959.
18. E. Mueller, Z.f. Phys. 108. 668. 1938, and Z.f. Phys. 120. 261. 1943.
19. F. Knauer, Z.f. Phys. 125. 278. 1948 and 126. 319. 1949.
20. T. H. Bull and J. G. Marshall, Nature, London, 167. 478, 1951.
21. R. D. Evans, Proc. Roy. Soc. A 139. 604, 1932.
22. J. A. Becker, Ann. N.Y. Accel. Sci. 58. 723-740, 1954.
23. M. Benjamin and R. O. Jenkins, Proc. Roy. Soc. Ldn. A 180. 225. 1942.
24. L. Frank, Trans. Faraday Soc. 32. 1003-14. 1936.
25. R. W. Ditchburn and J. C. Gilmour, Rev. Mod. Phys. 13. 310. 1941.
26. A. Eucken, Metallwirtschaft 15. 27. 1936.
27. E. Stuhlinger and R. Seitz, Astronautics, V4, No. 11, p. 37.
28. G. K. Wehmer, J. Appl. Phys. 30. 1762. 1959, also Phys. Rev. 108. 35-45. 1957, also Advances in Electronics and Electron Physics, Vol. VII. 239-298. 1955.
29. D. T. Goldman et. al., Phys. Rev. Vol. No. 2, 1958 July.
30. R. Bruenne, Z.f. Phys. 147. 165-183. 1957.
31. P. M. Waters, Phys. Rev. 109. 1466. 1958.
32. J. R. Pierce, J. Appl. Phys. 11. 548-54. 1940.
33. M. E. Hines, Proc. IRE 40. 60. 1952.
34. T. VanDuzer and G. R. Brewer, J. Appl. Phys. 30. 291. 1959.
35. R. Fox, ARS 927-59.
36. J. B. Langmuir and R. B. Cooper ARS 929-59.



37. H. Neuert, H. J. Stuckenberg and H. P. Weidner, Z.f. angewandte Phys. 6. 303. 1954.
38. P. C. Thoneman, Nature, Ldn. 158. 61. 1946.
39. R. N. Hall, Rev. Sci. Instr. 19. 905. 1948.
40. H. Neuert, Z.f. Naturforschung, 4a 456. 1948.
41. M. Chenot, Ann. Physique 12. 3. 277. 1948.
42. C. Swann and J. F. Swingle, Rev. Sci. Instr. 23. 636. 1952.
43. C. D. Moak, H. Reese, W. M. Good, Nuclonics 9. 18. 1951.
44. O. Reifenschweiler, Ann. Phys. 14. 33. 1954.
45. J. Sommeria, J. Phys. et Radium 12. 563. 1951.
46. J. Sommeria, J. Phys. et. Radium, 13. 645. 1952.
47. M. Von Ardenne, Tabellen der Elektron Physik, Ionen Physik, und
Ubermikroskopie, 1956.
48. ORNL-2802, TID-4500, Semi-Annual Report, p 67, July 1959.
49. UCRL 8775, Quarterly Report, p 29, May 1959.
50. Fasolo, "Hot Cathode Ion Source" UCRL 5285.
51. ORNL-2457, Jan. 1958, p 61.
52. Bohm, Burhop, and Massey, Characteristics of Electrical Discharges
in Magnetic Fields Ch. 2, edited by Guthrie and Wakerling.
53. McNally, Skidmore, and Werner, p 26, Semi Annual Report, Jan. 1959,
ORNL-2693, TID-4500.
54. Petrie, Amer. Jour. Phys. 16, 378, 1948.
55. H. Margenau and Lewis, Rev. Mod. Phys., July 1959.
56. H. Margenau, "Formulas for Estimating Widths of Spectral Lines
Emitted from Plasmas and their Limits of Validity", Unpublished.
57. H. Wulf, Z.f. Phys. 150, 614, 1958.
58. Davies, Proc. Phys. Soc. Ldn. B66, 33, 1958.
59. F. Moeller, J. Res. NBS 17, 849, 1936.
60. Landolt-Bornstein, I Band, 1 Teil, s 266.
61. H. N. Olsen, Bull. Amer. Phys. Soc., Vol. 4. No. 4, p 262, 1959.
62. L. B. Loeb, Basic Processes of Gaseous Electronics, 1955.
63. G. Francis, Handbuch der Physik, Band XXII, p 62-68.
64. Alpher and White, Phys. of Fluids 2, 162, 1959.
65. Spitzer, Physics of Fully Ionized Gases.
66. E. E. Petersen, A.I.C.H.E.J. 4.343. 1958.
67. A. S. Michaels, A.I.C.H.E.J. 5.270. 1959.
68. W. C. Rutledge and E. S. Rittner, J. Appl. Phys. 28. 170. 1957.
69. G. W. Sears, J. Chem. Phys. 22. 1252. 1954.
70. T. L. Hill, J. Chem. Phys. 25. 730. 1956.
71. W. Clausius, Ann. d. Phys. 7. 489-578. 1930.
72. R. Bernas and J. Sarrouy, C. R. Acad. Sci, Paris 233, 1092, 1951.
73. R. Bernas, Kaluszyner, and Armaux, J. Phys. Rad. 15. 273. 1954.



CURTISS-WRIGHT CORPORATION • RESEARCH DIVISION